VNIVERSITAT
DE VALÈNCIA

VACUUM DEPOSITED WIDE BANDGAP PEROVSKITE SOLAR CELLS

– PhD Thesis –

VNIVERSITAT DE VALÈNCIA

Doctorado en Nanociencia y Nanotecnología

Isidora Susic

Directors:

Prof. Dr. Hendrik Jan Bolink

Dr. Michele Sessolo

July 2023

Prof. Dr. Hendrik Jan Bolink, professor titular de la Universitat de València en l'Institut de Ciència Molecular (ICMol), i **Dr.Michele Sessolo**, investigador Ramón y Cajal en la Universitat de València, certifiquen que la memòria presentada per l'estudiant de doctorat Isidora Susic, amb el títol "*Vacuum deposited wide bandgap perovskite solar cells*", correspon a la seua Tesi Doctoral i ha sigut realitzada sota la seua direcció i tutoria, autoritzant mitjançant aquest escrit la presentació d'aquesta.

A Paterna (València), a 25 de Julio de 2023.

Prof. Dr. Hendrik Jan Bolink	Dr. Michele Sessolo
(Director i tutor)	(Director)

Mojoj porodici.

Index

Chapter 1

Introduction and aim of the thesis

1.1 Global warming and photovoltaics

Over the last century the world population increased from 2 billion to approximately 8 billion, accompanied by an equally large rise in demand for energy. Nowadays the main energy sources are fossil fuels such as oil, natural gas and coal, that are finite and upon combustion release substantial amounts of CO_2 in the atmosphere.[1] This gas is a major contributor to the greenhouse effect, leading to global warming and hence to climate change. Therefore, there is a need to implement renewable energy sources such as solar and wind, which are cleaner and more sustainable. The use of renewable energy sources has increased significantly, however, they still represent only a small percentage (approximately 15%) of the global energy generation. Hence, more efforts need to be undertaken in order to replace the use of fossil fuels and reduce their impacts on climate. The challenge is to continue to explore and develop new technologies that are more efficient, cost-effective and sustainable, helping to reduce greenhouse gas emissions and the use of finite resources. Among all renewable reserves, solar energy presents by far the planet's largest energy source accessible (Figure 1.1).[2]

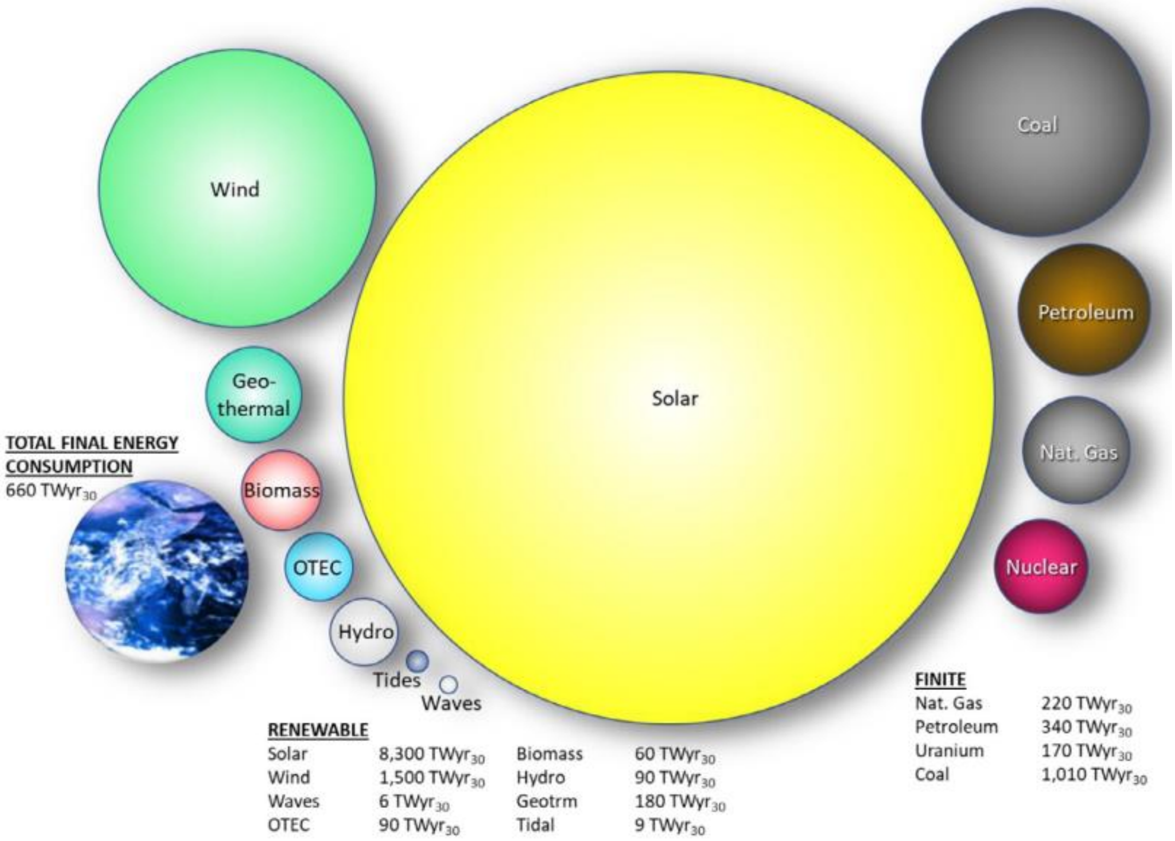

Figure 1.1. Reasonably Assured Recoverable Reserves of renewable and finite energy resources.[2]

Among the solar energy harvesting technologies, the most promising is photovoltaics (PVs), which involves the direct conversion of solar to electrical power. The photovoltaic effect was discovered and first reported by Edmund Bequerel in 1839. Since then, and especially with the development of semiconductors, several types of PV devices have been developed, which are typically divided in three generations.[3];[4] Today's PV market is dominated by silicon solar cells, that presents the first and more mature generation of solar cells. They are based on thick crystalline layers composed of abundant and non-toxic material, silicon. This first generation includes mono-, poly-, and multicrystalline silicon, but also crystalline III-V semiconductors such as GaAs. GaAs has reached the record efficiency for a single junction solar cell of 29.1%, although at a high cost, due to the price of starting materials and overall device processing.[5] Currently the best silicon solar cells are approaching their theoretical limit of 29% power conversion efficiency (PCE), with a record reported efficiency of 26.8%.[6] However, since silicon is a relatively weak absorber of long wavelength sunlight, thick (100-500 μm) silicon layers are necessary to quantitatively harvest solar radiation, which significantly increases the cost of materials. As a result, the main restrictions for silicon technology are the high costs associated with both raw materials and installation. In order to address these limitations, alternative materials have been investigated in the second-generation thin-film solar cells. As the name suggests, they consist of layers of semiconductors only a few micrometers thick, resulting in a reduced material usage and lightweight devices, that can lower the overall price of the solar cell. The three main thin-film technologies are amorphous silicon, cadmium telluride (CdTe), and copper indium sulphide/selenide (CIGS). CdTe solar cells have demonstrated promising efficiency in excess of 22%, however their share in the global market is still low (approximately 5% market share) mainly due to limitation factors such as high toxicity of cadmium and the use of rare materials.[7] Currently, the research focus is on third-generation devices that are based on unconventional semiconductors with the potential of being inexpensive while delivering high power efficiency. Main examples are organic solar cells (OSCs), dye sensitized solar cells (DSSCs), perovskite solar cells (PSCs) and quantum dot (QD) solar cells. OSCs are promising because of their continuously increasing efficiency (recently close to 19%), flexibility, semi-transparency, and applicability to large-scale roll-to-roll processing. DSSCs are promising because of their simple fabrication, low material costs, and their benefits in semi-transparency and color tunability. However, the main challenges towards the application of DSSCs are the low power conversion efficiency (13%) and limited cell stability. Among third generation semiconductors, metal halide perovskites are the most promising ones due to their optoelectronic properties, such as high absorption coefficient, low exciton binding energy, high charge carrier mobility, and widely tunable bandgap.[8] Initially, perovskites were used as sensitizers in liquid dye-sensitized solar cells, demonstrating power conversion efficiency of up to 6.5% using $CH_3NH_3PbI_3$.[9],[10] In 2012. the groups of Grätzel and Park first designed solid-state perovskite solar cells reaching efficiency of 10%.[11] Over the last decade, perovskites have been widely studied and developed, reaching record efficiency that exceeds 25%, as illustrated in the NREL chart in Figure 1.2.[5]

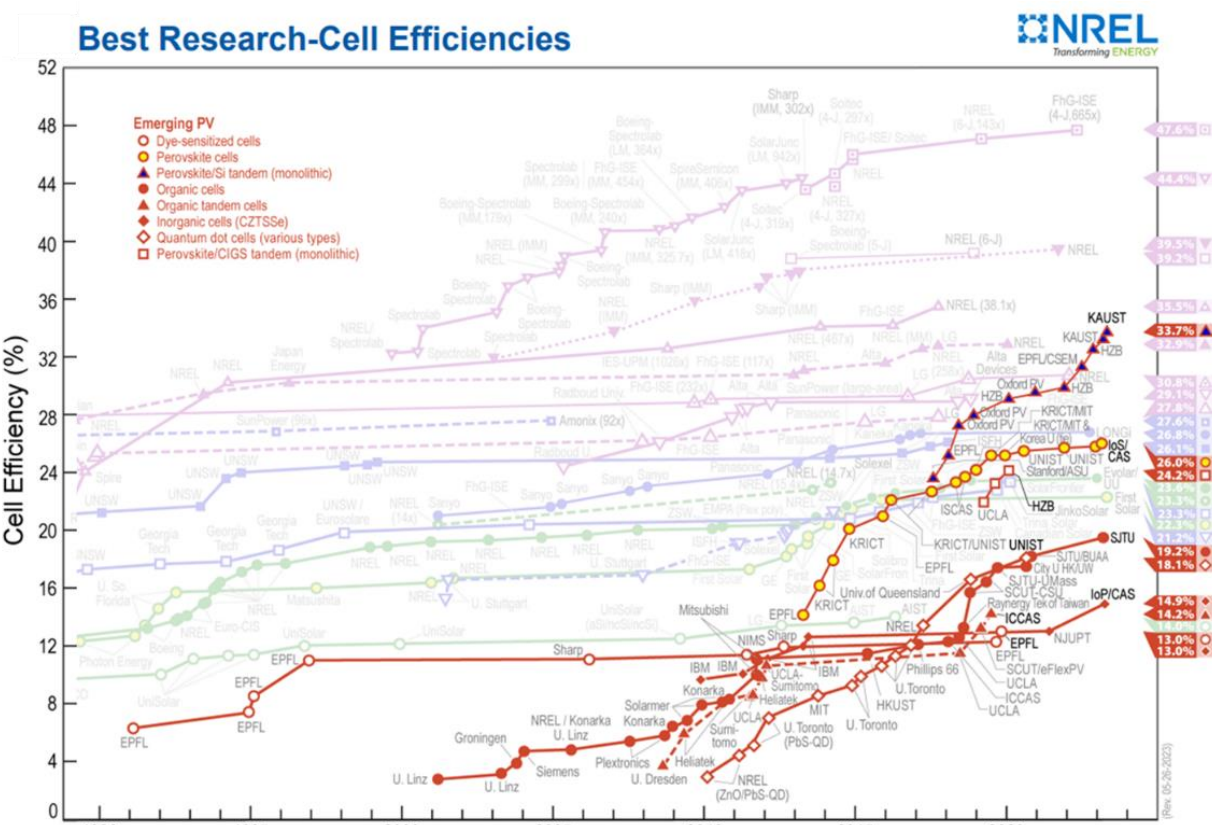

Figure 1.2. Efficiency chart of different solar cell technologies- NREL.[5]

1.2 Working principle of solar cells

A solar cell generates electric power by producing both a current and a voltage when it is exposed to light. General processes in the operation of a solar cell are: absorption of photons, carrier generation and recombination, charge transport and collection. These processes are outlined in Figure 1.3a, where the absorber layer is a semiconductor.

Semiconductors are defined by their bandgap (E_g), a forbidden energy region without intrinsic electronic states. The bandgap refers to the energy gap between the highest energy level of the valence band (VB, completely occupied with electrons) and the lowest energy level of the empty conduction band (CB). When an intrinsic (undoped) semiconductor is in equilibrium (in the dark), the Fermi level is located in the middle of the bandgap. When the semiconductor is exposed to light, photons with energy $E_{ph} = h\nu$ larger than E_g will be absorbed, resulting in electron-hole pairs generation. In other words, electrons are excited from the VB to the CB, leaving positive charges that can move freely in the valence band. Photons with $h\nu < E_g$ are not absorbed, they are either transmitted or reflected by the semiconductor. The excess energy ($h\nu - E_g$) of absorbed photons is dissipated as heat to the semiconductor lattice through a process called thermalization. After fast thermalization within the bands, electrons and holes redistribute at the conduction and valence band edges, respectively. Their energy distribution can be described by two separate quasi-Fermi levels, one for electrons (E_F^n) and one for holes (E_F^p). The energy difference between them is called quasi-Fermi level splitting (QFLS) and represents the upper limit for the open circuit voltage of a solar cell (Figure 1.3b).

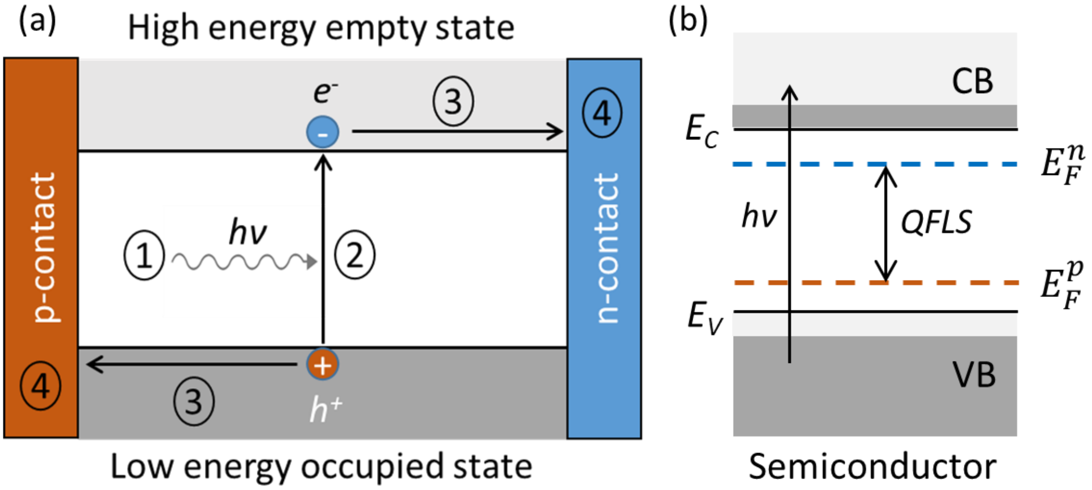

Figure 1.3. Schematic illustration of a) the processes taking place in a solar cell and b) energy bands for a semiconductor upon photon absorption.

The charge carrier (electrons and holes) generation upon photon absorption is described by the absorption coefficient α of the semiconductor, which is proportional to the density of occupied and available electronic states in the VB and CB, respectively. However, the maximum of the valence band and the minimum of the conduction band are not generally at the same value of the momentum of the electron–hole system. In a direct bandgap semiconductor, the electronic transition does not involve a change of momentum and hence electron-hole pairs generation is statistically more favored, increasing the absorption coefficient. As a consequence, solar cells made from these materials can be very thin (hundreds of nanometers to few micrometers) to quantitatively absorb all the light with $h\nu > E_g$. On the other hand, the probability of transition is lower in indirect bandgap semiconductors, where the transition is not vertical. The transition does not take place with only the absorption of a photon: electrons need to interact both with the photon and with a lattice vibration (phonon) in order to either gain or lose momentum, leading to a smaller α value. Hence, solar cells based on indirect semiconductors such as Si and Ge need to be thicker (tens to hundreds of micrometers) to quantitatively absorbs all the above-bandgap photons. After generation of electron–hole pairs, electrons and holes are selectively extracted by the hole and the electron transport materials and collected at the electrodes. Nevertheless, the charge collection is in competition with recombination processes that occur either in the bulk or at interfaces of the material. There are two principal recombination mechanism: radiative and non-radiative (Shockley-Read-Hall) recombination, as illustrated in Figure 1.4.

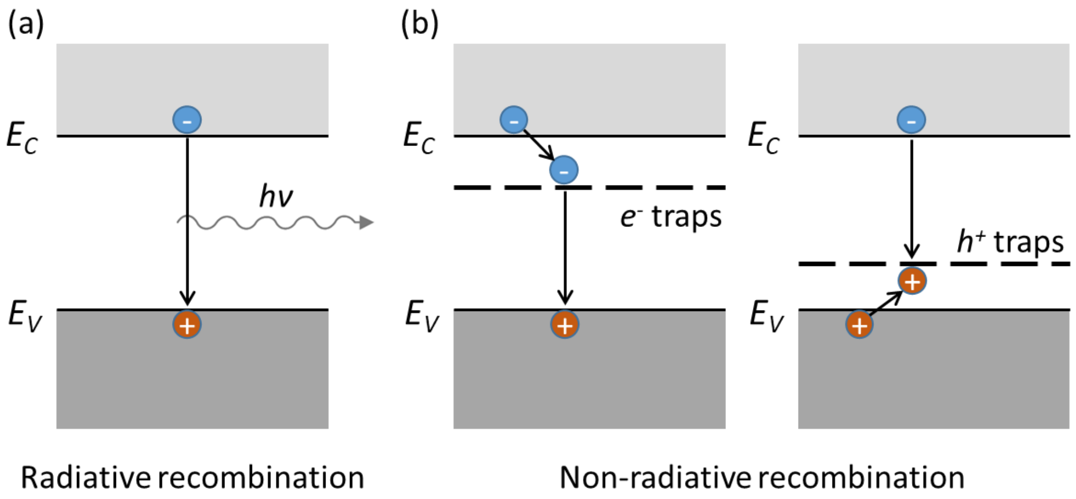

Figure 1.4. Schematic illustration of a) radiative and b) non-radiative (trap-assisted) recombination.

In the radiative recombination process, electrons relax back in the valence band and the excess energy is released as a photon with $E_g = h\nu$. On the other hand, non-radiative recombination occurs when an electron or hole is trapped in an electronic energy level (trap state) located within the bandgap. Trap states are associated with defects in the material (either structural or elemental), that can either be introduced in the form of impurities or through intentional doping of the material. Non radiative recombination involves two steps: an electron or hole is first trapped in a trap state and then, once a carrier of opposite charge comes in the vicinity of the trap, recombination takes place. It is important to note that non-radiative recombination processes decrease the QFLS in the semiconductors, therefore it is important to minimize them in order to have an efficient power generation in solar cells.

The solar irradiance spectrum is distributed over a range of wavelengths from 280 to 4000 nm, and outside of the Earth's atmosphere follows approximately the radiation of a black body at 5800 K. The solar radiation is attenuated and distorted due to reflection and absorption by atmospheric gases. The air-mass (AM) coefficient represents the amount of air that the light has to pass through and depends on the distance and on the incidence angle. The spectrum outside the atmosphere corresponds to an AM0 and that on the surface of the earth for normal incidence to AM1. Currently, Air Mass 1.5 Global (AM1.5G) is used as the standard reference solar spectrum and refers to the radiation arriving at the earth’s surface after passing through 1.5 times a standard air mass, with the sun at 48.2° (Figure 1.5).[12] This type of illumination is denominated “1 sun”, and its intensity is approximately 100 mW/cm^2.

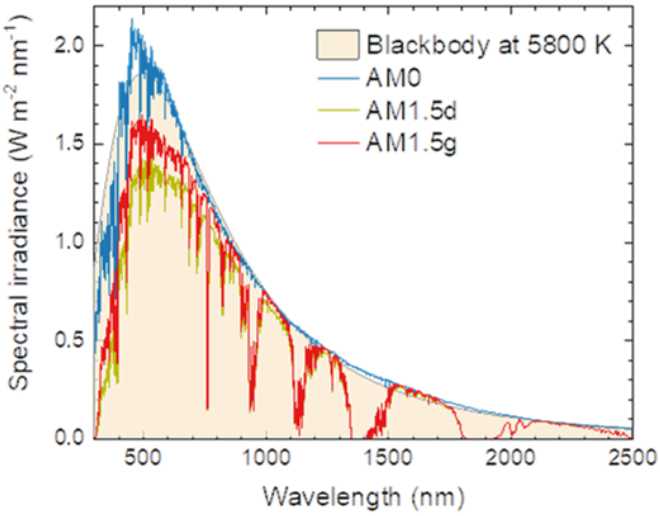

Figure 1.5. The spectral irradiance from the sun just outside the atmosphere (AM0) and (AM1.5G) terrestrial solar spectrum.

The charge carrier collection yield in solar cells can be quantified via the external quantum efficiency (EQE). The EQE is the ratio between the number of charge carriers extracted from the solar cell and the number of impinging photons of a given energy. For an ideal solar cell, where all photons of a certain wavelength are absorbed and all resulting carriers collected, the EQE spectrum would be unity and constant for $h\nu \geq E_g$ (square line in Figure 1.6). However, in real solar cells the EQE is always < 1 due to several possible loss mechanisms, such as bulk/surface recombination and optical losses.

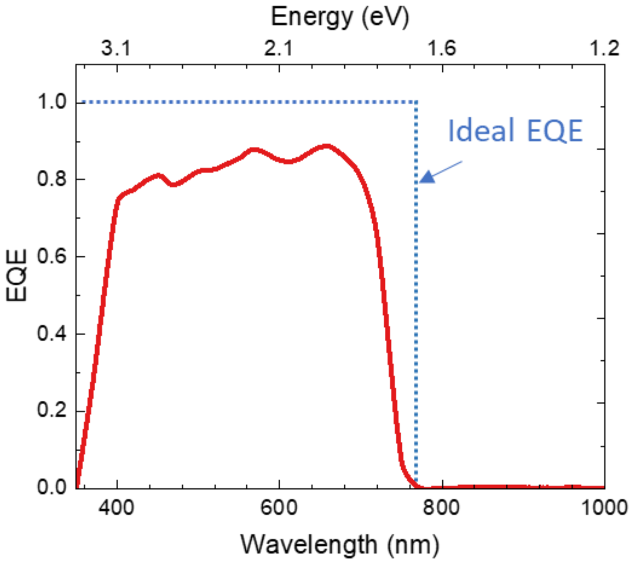

Figure 1.6. EQE spectrum of a perovskite solar cell.

When a solar cell is in the dark it behaves as a simple diode, conducting current only in the forward bias directions. The relation between current and voltage in a diode can be seen in the current density versus voltage (J-V) curve (Figure 1.7a) that is described by the Shockley equation:

$$J = J_0 \left(e^{\frac{qV}{nkT}} - 1 \right) \qquad \text{Equation 1.1}$$

where J_0 is dark saturation current, V is the applied voltage, q is the elementary charge, n is the ideality factor, k the Boltzmann constant and T the absolute temperature. When a solar cell is exposed to light, a (negative) photocurrent is generated and the J-V curve shifts down the vertical axis (Figure 1.7b). The current density of an ideal solar cell can be described by the following equation:

$$J = J_0\left(e^{\frac{qV}{nkT}} - 1\right) - J_{ph} \qquad \text{Equation 1.2}$$

where J_{ph} is the photocurrent. For the characterization of solar cells, the main figure of merit is the PCE, which can be defined with the following parameters: short-circuit current (J_{sc}), open circuit potential (V_{oc}), and fill factor (FF). These parameters can be extracted from J-V curves of a cell under 1 sun illumination.

The short-circuit current density (J_{sc}) refers to the current density through the solar cell when the applied voltage is zero. It is the current per unit area of the cell. It depends on the spectrum of the incident light, the photon flux, carrier collection probability, the absorption coefficient and thickness of the absorber materials among others. The open-circuit voltage (V_{oc}) corresponds to the maximum voltage delivered by a solar cell and occurs when there is no current flow. The V_{oc} depends primarily on the bandgap of the semiconductor absorber, increasing as the bandgap increases, and its upper limit is dictated by the QFLS. As mentioned previously, the QFLS is maximum when all charge recombination occurs radiatively. Hence, by determining the luminescence efficiency one can obtain information about the maximum V_{oc} a solar cell can produce. In order to define the efficiency, one needs to determine how much power a solar cell can deliver. This can be derived from the J-V curve of a solar cell under 1 sun illumination. The power output of a solar cell is given as:

$$P_{out} = I \cdot V \qquad \text{Equation 1.3}$$

where I is the current passing through the device at a given voltage (V), resulting in the power curve depicted in Figure 1.7c. The maximum of the curve, where the product of the voltage and current is maximum, is called maximum power point (MPP). The voltage and current density at the MPP are V_{mpp} and J_{mpp} , respectively. The power density ($P_{max} = J_{mpp} \cdot V_{mpp}$) is represented as the green area in the J-V plot (Figure 1.7d). The ratio between the maximum power density and the product of V_{oc} and J_{sc} is known as fill factor:

$$FF = \frac{J_{mpp} \cdot V_{mpp}}{V_{oc} \cdot J_{sc}} \qquad \text{Equation 1.4}$$

In the J-V curve the FF corresponds to the ratio between the rectangle with sides V_{mpp} and J_{mpp} and the area with sides of V_{oc} and J_{sc}. The FF gives information about the efficiency of the charge transport and extraction in a solar cell. It depends on both the semiconductor material and device architecture. The PCE is defined as the ratio between the electrical power generated by the solar cell and the radiant power density incident on the solar cell, and is expressed in percentage:

$$PCE = \frac{P_{out}}{P_{in}} = \frac{P_{max}}{P_{in}} = \frac{FF \cdot J_{sc} \cdot V_{oc}}{P_{in}} \times 100 \qquad \text{Equation 1.5}$$

where P_{out} is defined in its MPP. The PCE depends on the operation conditions (light source) and it is usually reported under a simulated standard sun spectrum AM1.5 G, with an incident power of 1000 W m^{-2} (100 mW cm^{-2})

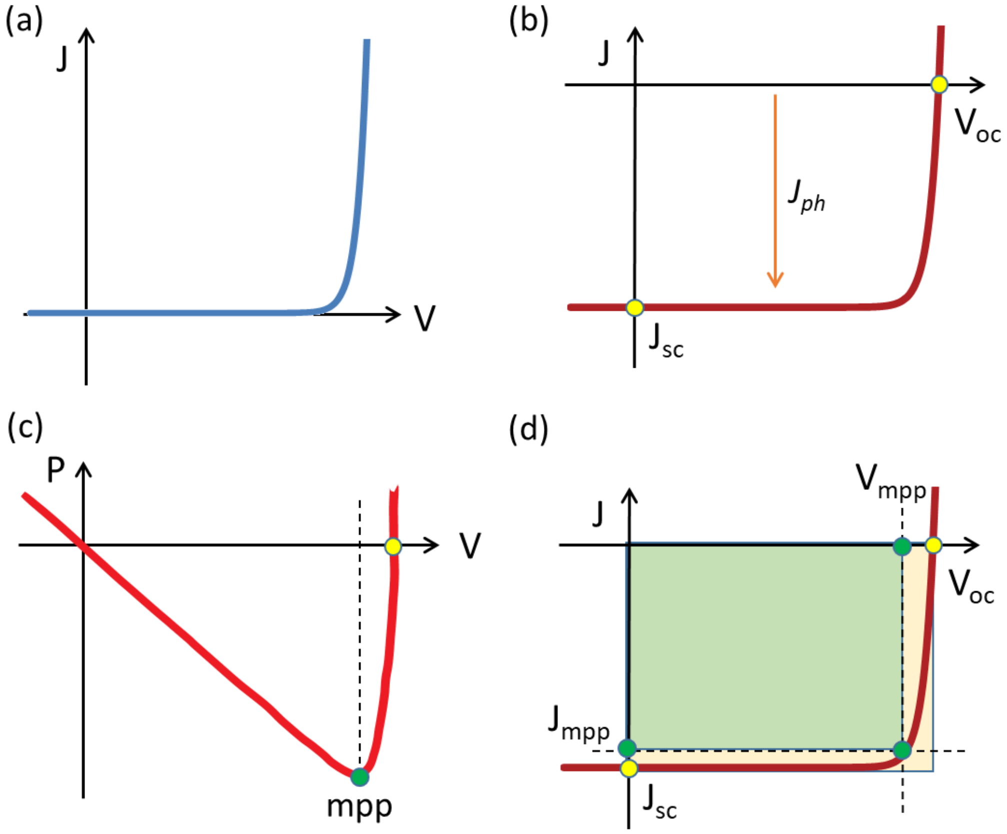

Figure 1.7. Schematic a) current density–voltage (J-V) curve in the dark, b) J-V curve under illumination, c) power density-voltage curve and d) J-V curve under illumination with characteristic parameters.

1.2.1 Radiative limit

In 1961, Shockley and Queisser proposed a model to calculate the maximum possible efficiency of a photovoltaic device, known as the Shockley–Queisser limit or radiative efficiency limit.[13] The model is based on several assumptions, among which the most important are that all photons with $h\nu \geq E_g$ are quantitatively absorbed, charge carriers have infinite mobility and only radiative recombination is taken into account. Figure 1.8a shows the theoretical maximum efficiency for a single-junction solar cell under AM1.5G illumination as a function of bandgap, where the maximum efficiency is 33.7% for a semiconductor with E_g = 1.34 eV.[14]

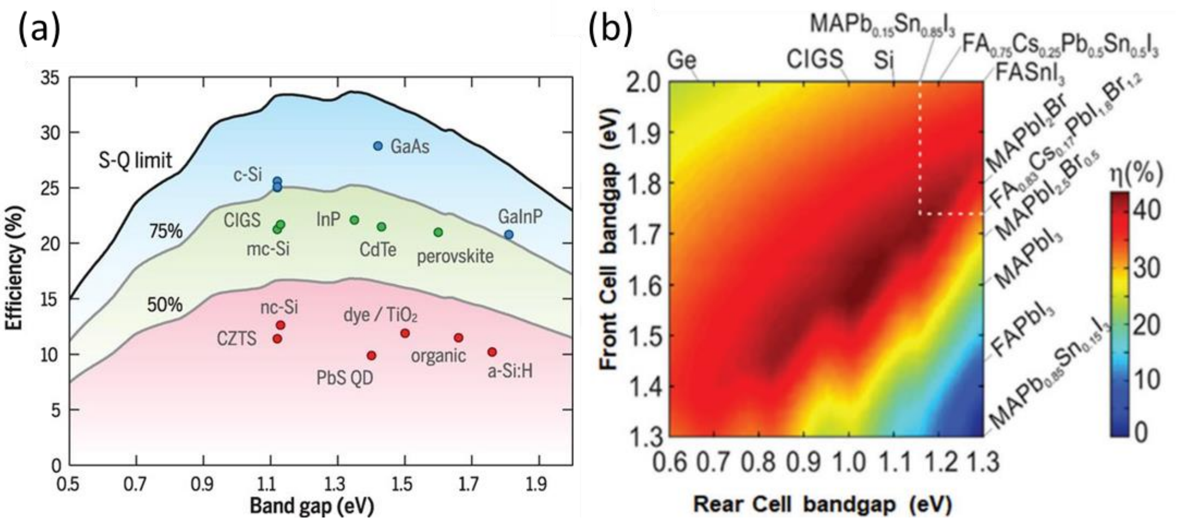

Figure 1.8. a) Theoretical radiative efficiency limit as a function of bandgap and b) calculated theoretical PCE (η) for tandem solar cells with different bandgap combinations of front and rear subcell absorbers.[14],[15]

As previously mentioned, in a single-junction solar cell, photons with energies below the E_g of the active material cannot be absorbed which results in current losses. On the other hand, photons with higher energies lead to charge carriers that quickly thermalize (loose energy in the form of heat) to band edges from where they are extracted, leading to unavoidable energy losses. In the radiative limit, the efficiency of a solar cell is limited mainly by the fraction of photons absorbed and by carrier thermalization. One approach to overcome this limitation is to include multiple absorber layers with complementary bandgaps in the solar cell structure, forming multi-junction solar cells.[16],[17] The most common one contains two different bandgap absorbers and is revered to as a tandem solar cell. Each light absorber has a different bandgap and absorbs a different part of the solar spectrum which allows to minimize thermalization losses and to reach higher PCEs. As shown in Figure 1.9 a double-junction solar cell consists of a wide bandgap 'top cell' that absorbs high-energy photons and allows lower energy photons to pass through and to be absorbed in the narrow bandgap 'bottom cell'. In this way thermalization losses are reduced compared to single-junction solar cell.

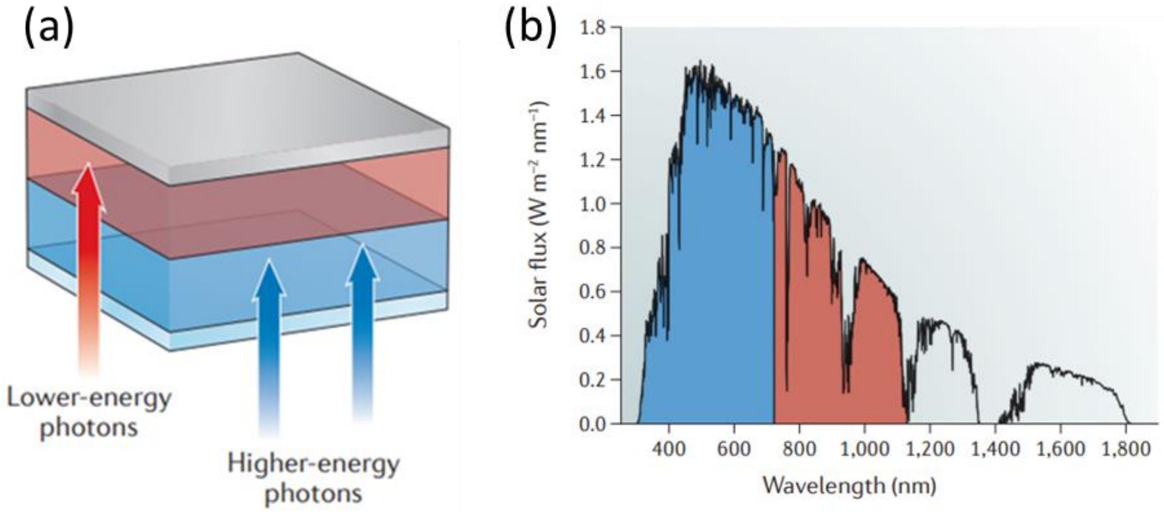

Figure 1.9. a) Scheme of tandem device and b) Spectra response of top cell and bottom cell in a tandem configuration.

In theory, connecting two semiconductor junctions with complementary bandgaps could lead to efficiency limit of 46%, adding a third junction would further increase the efficiency to 52%, and an infinite number of junctions would lead to 68% efficiency.[18] However, commercially available multi-junction solar cells are based on expensive epitaxial crystalline semiconductors, and hence are almost exclusively used for space applications.[19] In this context, there is a growing interest in developing cost-effective alternatives for highly efficient tandem solar cells. Perovskite materials have emerged as promising candidates due to their tunable bandgaps in the region of 1.2–3.0 eV, combined with simple thin film processing. They can be employed both as top cell with Si or CIGS or combined with a second perovskite absorber to form all-perovskite tandem solar cells. A key requirement is to select the absorbers with appropriate bandgap for both cells (Figure 1.8 b).[15] For instance, the ideal absorber to use as a front cell with a 1.1 eV semiconductor back cell (c-Si) is a perovskite that has a bandgap in the 1.6-1.75 eV range. On the other hand, all-perovskite tandems can be obtained combining a front cell with bandgap of 1.8 eV with a 1.2 eV bandgap perovskite bottom cell. Current record efficiencies for perovskite/Si and all-perovskite tandems are 33.7% and 29.1%, respectively, outperforming the performance of single-junction solar cell.[5],[20]

1.3 Perovskites

Perovskites, discovered by Gustav Rose in 1839, refer to the mineral form of $CaTiO_3$ and are named after the Russian mineralogist Lev Perovski. The perovskite structure is described by the general ABX_3 formula, where a three-dimensional framework is composed of corner-sharing BX_6 octahedra. The B-site cation is located in the center of each octahedron, surrounded by six X anions, meanwhile a larger A-site cation occupies the cubo-octahedral cavity surrounded by twelve X anions, balancing the charge. (Figure 1.10).[8] There are many types of perovskites ranging from the natural mineral to superconducting cupper oxides to name an example. The type of perovskite interesting for opto-electronic applications such as solar cells consist typically of the following ions. The A cation is a positive monovalent inorganic or organic cations such as Cs^+, methylammonium ($CH_3NH_3^+$) or formamidinium ($CH_3(NH_2)_2^+$), B is a positive divalent metal (typically Pb^{2+}, Sn^{2+}, but also Ge^{2+}) and X is a halide (I^-, Br^-, Cl^-).

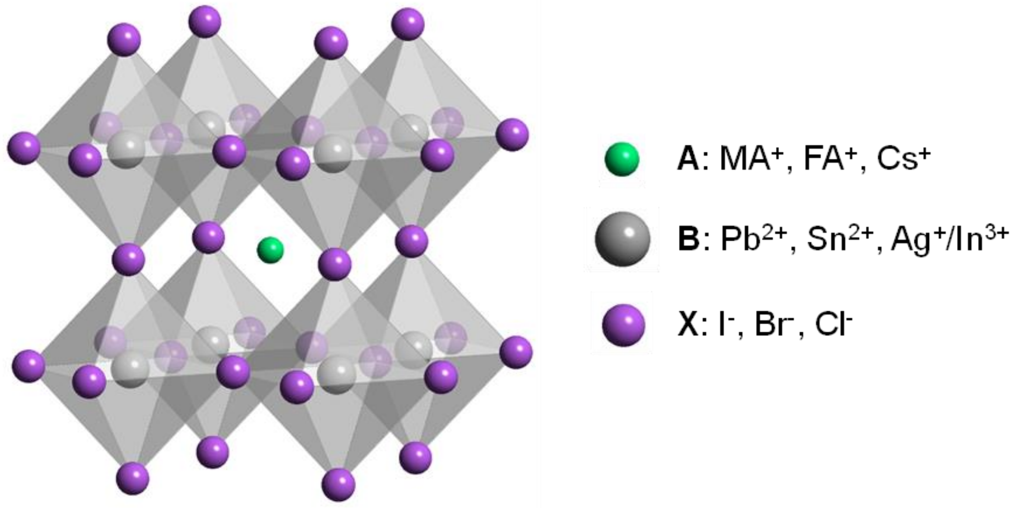

Figure 1.10. Perovskite ABX_3 crystal structure.

The structural stability of the perovskite structure can be estimated considering its geometric tolerance factor, described by Victor Goldschmidt in 1926:

$$t = \frac{r_A + r_X}{\sqrt{2}(r_B + r_X)} \qquad \text{Equation 1.6}$$

where r_A, r_B and r_X are the effective ionic radii of the A, B and X ions, respectively.[21] For halide perovskites, a stable structure is expected for tolerance factors ranging between 0.8 and 1.1. The cubic structure is predicted for $t = 1$, while the symmetry decreases for deviating t values, for example in orthorhombic ($t < 0.8$) or hexagonal phases ($t > 1$). It is worth noting that the tolerance factor does not account for the temperature, and a given perovskite formulation will undergo phase transitions when cooling or heating the material. In the case of the widely studied $MAPbI_3$, where the A-site cation is $CH_3NH_3^+$ (MA^+), the B-site cation is $Pb^{2+}$and I^- is the anion, three phases have been identified, with the tetragonal structure one being the most stable at room temperature. The transition from the tetragonal to the cubic phase occurs at approximately 330 K (57 °C), while at temperatures below 160 K the stable phase is an orthorhombic structure, as illustrated in Figure 1.11.[22]

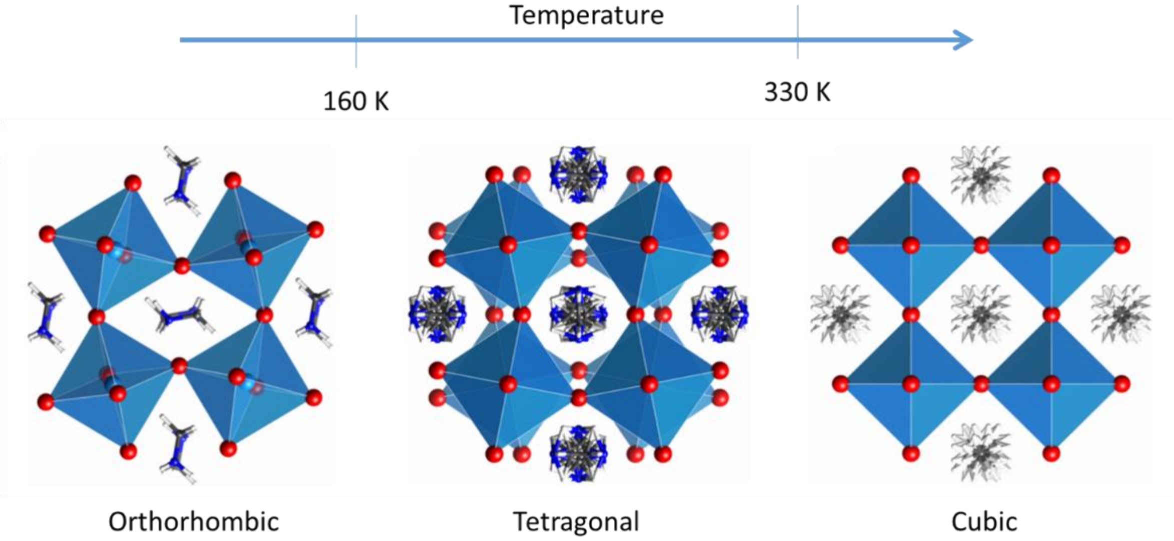

Figure 1.11. Temperature dependent crystal structure of $CH_3NH_3PbI_3$.[22]

On the other hand, formamidinium lead iodide ($FAPbI_3$) has a large tolerance factor and is more stable in the hexagonal δH-phase (yellow phase) at room temperature. Note that $FAPbI_3$ in this phase is not a semiconductor, but the semiconducting perovskite α-phase can be stabilized at elevated temperatures.[23] On the contrary, if we replace the MA^+ cation with the smaller Cs^+, the tolerance factor becomes too low to sustain the cubic structure. For $CsPbI_3$, the more stable structure at room temperature is a yellow orthorhombic phase, which undergoes a transition to the perovskite black phase at approximately 300 °C.[24] Three dimensional (3D) structures are obtained when the A cation is small enough to fit in the cavity formed by the octahedral lead halide framework. If a larger organic cation is introduced, the structure collapses into a low dimensional 2D material with the tolerance factor t much larger than 1. 2D perovskites consists of octahedral lead halide sheets separated by double layers of organic cations ($n = 1$), while quasi-2D perovskites are obtained when n octahedral layers ($n = 2, 3, \ldots$) are formed. For quasi-2D perovskite to form, the co-existence of large organic cations and small A-site cations is needed (Figure 1.12a).[25] The general formula of low dimensional perovskite is $(RNH_3)_2(A)_{n-1}B_nX_{3n+1}$ (with n = 1, 2, 3, 4……), where RNH_3 is a large aliphatic or aromatic alkylammonium spacer cation, such as 2-phenylethylammonium (PEA^+) or n-butylammonium (n-BA^+), A is monovalent organic cation (usually MA^+ and FA^+), M is a divalent metal, X is a halide, and n represents the number of octahedral inorganic $[BX_6]^{4-}$ layers. By changing n, these materials show different electronic properties. For example, as the number of inorganic layers decreases, the corresponding bandgap becomes wider, as shown in the Figure 1.12b.

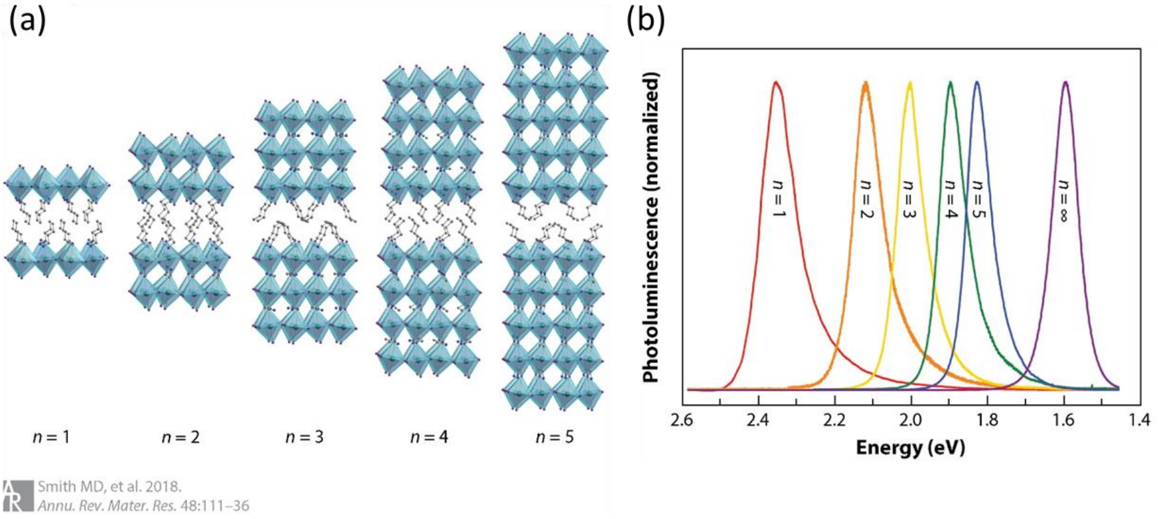

Figure 1.12. a) Crystal structures of the n = 1–5 members of the $(C_4H_9NH_3)_2(MA)_{n-1}Pb_nI_{3n+1}$ perovskite family and b) their corresponding photoluminescence.[25]

1.3.1 Physical properties

Hybrid perovskite are direct bandgap semiconductors that exhibit many favorable properties for applications in optoelectronics. Probably their most important property is their resilience towards defects which enables the use of low cost deposition methods. This is a remarkable feature as all other inorganic semiconductors require a close to perfect alignment of the atomic constituents in the respective crystal lattice. Such high degree of alignment is only achieved with careful crystallization methods which limit the speed of growth. Their *high optical absorption coefficient* ($\approx 10^5$ cm^{-1}) allows to efficiently harvest the incident light while maintaining the absorber layer thickness low which means that weight depends primarily on the type of substrate used.[26] Another important property of perovskites is their balanced electron/hole mobility and *long diffusion length* (in the 1-100 μm range), which allows for efficient charge transport with limited recombination in thick perovskite films.[27],[28] The *high dielectric constant* results in a low exciton binding energy, favoring the generation of free carriers at room temperature.[29] Another important characteristic of halide perovskites relates to their *tunable bandgap*. By changing different B, and/or X ions, it is possible to tune the optical gap at will, making them suitable for different optoelectronic applications.[30] The valence band of lead halide perovskites is formed from a mixture of metal s-orbitals and halide p-orbitals, while the conduction band contains predominantly metal p-orbitals. Therefore, the valence band position is strongly influenced by the type of halide used (I, Br, Cl), and substitution with smaller (more electronegative) halides results in downward shift of the VBM and a larger bandgap. Increase of the bandgap with increasing halide electronegativity is shown in Figure 1.13 as a blue shift of the optical absorption and emission in $CsPbX_3$ colloids. Furthermore, when varying the B site in the perovskite structure, for instance replacing Pb with less electronegative Sn, the VBM and the CBM shift upward leading to a reduction of the bandgap in Sn and mixed Sn/Pb compounds. On the other hand, the A site cation substitution influences the electronic structure indirectly via changing the volume of the ABX_3 lattice or by introducing distortion in the ideal perovskite structure.[31] For example, substitution of MA^+ cation with larger FA^+ tilts the metal-halide octahedra, decreasing the bandgap from 1.6 eV for $MAPbI_3$ to 1.50 eV for $FAPbI_3$.

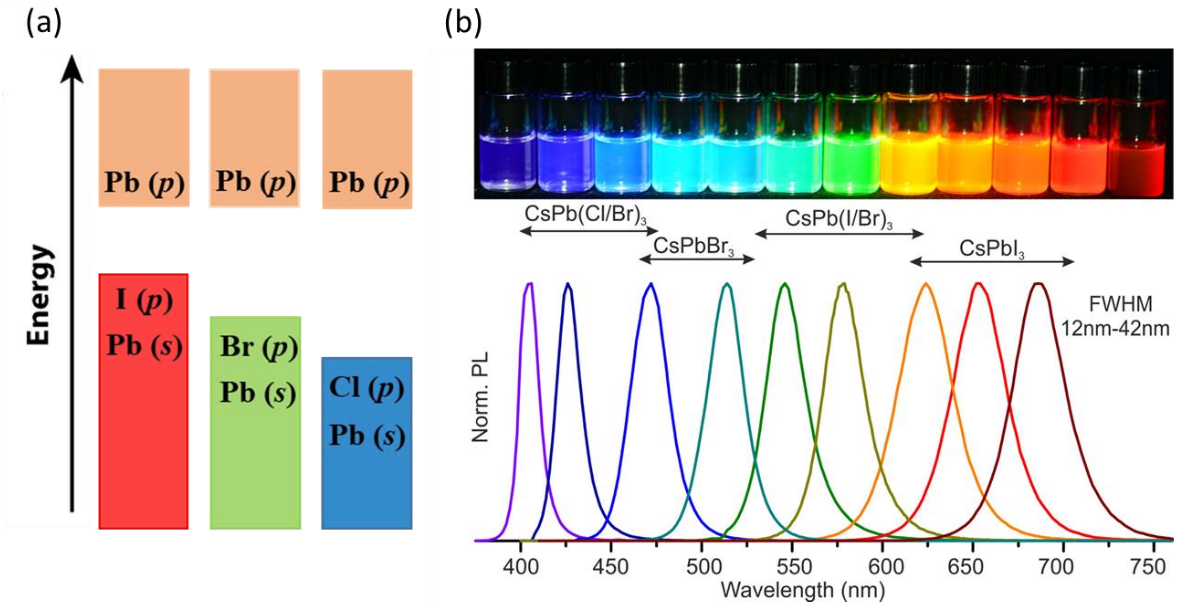

Figure 1.13. a) Schematic diagram of the electronic bands for different lead halide perovskites and b) colloidal solutions of $CsPbX_3$ NCs (X = Cl, Br, I) in toluene under UV lamp ($\lambda = 365$ nm) and representative PL spectra.[32]

1.4 Wide bandgap perovskites

Semiconductors with bandgap > 1.6 eV are of particular interest for multi-junction solar cells, and halide perovskites are particularly suited for this task. The simplest way to obtain wide bandgap perovskites is by using mixed iodide/bromide formulations, as the resulting bandgap can be tuned over a wide range by changing the I/Br ratio (Figure 14a). However, when increasing the bromide content, mixed-halide perovskites can undergo phase segregation under illumination, separating into low-bandgap I-rich and wide-bandgap Br-rich domains. This phenomenon was first reported for a $MAPb(Br_xI_{1x})_3$ perovskite by Hoke *et al*.[33] Figure 1.14b clearly shows this phenomenon by measuring the photoluminescence (PL) spectrum over time. Under continuous illumination, the initial PL peak of a homogeneous $MAPb(Br_{0.4}I_{0.6})_3$ film at 1.85 eV decreases over time, and a peak that corresponds to lower bandgap, I-rich domains appears at 1.68 eV.

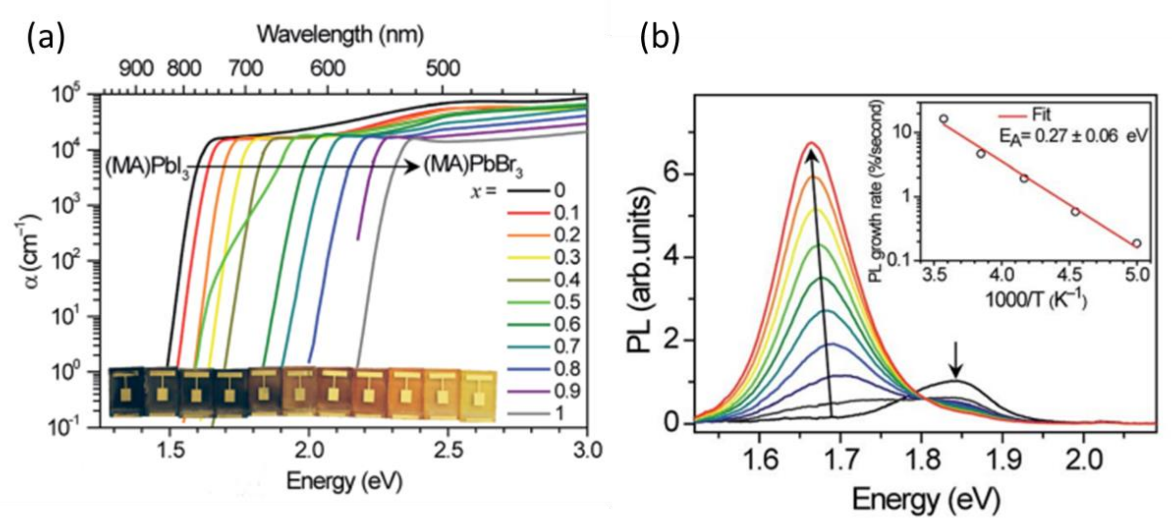

Figure 1.14. a) Absorption coefficient of $MAPb(Br_xI_{1-x})_3$ from x = 0 to x = 1 and b) PL spectra of an x = 0.4 thin film over 45 s in 5 s increments under 457 nm.[33]

This additional peak grows in intensity under continuous illumination, and can be reversible or attenuated depending on the perovskite formulation. Several strategies to suppress halide segregation have been reported, including compositional engineering, formation of 2D/3D perovskites, and interface chemical modification. Substitution of the A-site cation, in particular by replacing MA^+ with mixtures of Cs^+ and FA^+ is an effective way to minimize the halide segregation.[34],[35] Efficient wide bandgap PSCs with mixed FA^+/Cs^+ based perovskites were first reported by McMeekin *et al.*, as a result of the enhanced photostability of the material.[36] Triple cation $Cs^+/MA^+/FA^+$ perovskite compositions were found to be also more thermally stable, reaching stabilized power efficiency of 21.1%.[37] Partial substitution of the larger formamidinium with the smaller cesium, due to octahedral tilting leads to an increase in the bandgap, which allows to reduce the amount of Br and further mitigate the phase segregation.[38] Additionally, the incorporation of alkali metal ions such as potassium (K^+) and rubidium (Rb^+) can passivate the defects at grain boundaries and reduce non-radiative recombination.[39],[40],[41]

Apart from small cations, large aliphatic or aromatic alkylammonium cations have also been introduced to achieve highly efficient and stable 2D/3D heterojunctions PSCs.[42] When these large organic cations are added to the conventional 3D perovskite lattice, mixed-dimensional perovskites with enhanced stability are obtained.[43],[44],[45] 2D perovskites have also been applied to passivate the surface and the grain boundaries of perovskites, diminishing the non-radiative recombination loss. Gharibzadeh *et al.* designed a hybrid

2D/3D perovskite heterostructure by depositing BABr on the 3D perovskite surface, realizing PCE of 19.4% and a record V_{oc} of 1.31 V for a bandgap of 1.72 eV.[46] Another strategy involves the use of A-site cations that are only slightly larger than those used in stable 3D halide perovskites, and that for this reason are sometimes called "pseudo A-cations". One example of large pseudo-A cation is dimethylammonium (DMA^+). By using DMA^+ in combination with cesium, the amount of bromine needed to obtain a wide bandgap perovskite ($\geq$ 1.7 eV) can be reduced, consequently limiting undesirable photoinduced phase segregation and leading to a more stable formulation.[47],[48]

An alternative approach to achieve wide bandgap perovskites is to fabricate pure inorganic perovskites such as $CsPbI_3$. Currently, there is a significant focus on fully-inorganic perovskites, due to their potentially superior chemical stability when compared to the organic-inorganic materials.[49] The $CsPbI_3$ perovskite have a wide bandgap of 1.73 eV, nevertheless, as mentioned before, the black cubic phase (α-$CsPbI_3$) is normally obtained only at high temperature (>300°C).[32] At room temperature it tends to convert to the non-semiconducting orthorhombic phase with a bandgap of ~2.82 eV, as a consequence of the small size of Cs^+ which reduces the tolerance factor (Figure 1.15).

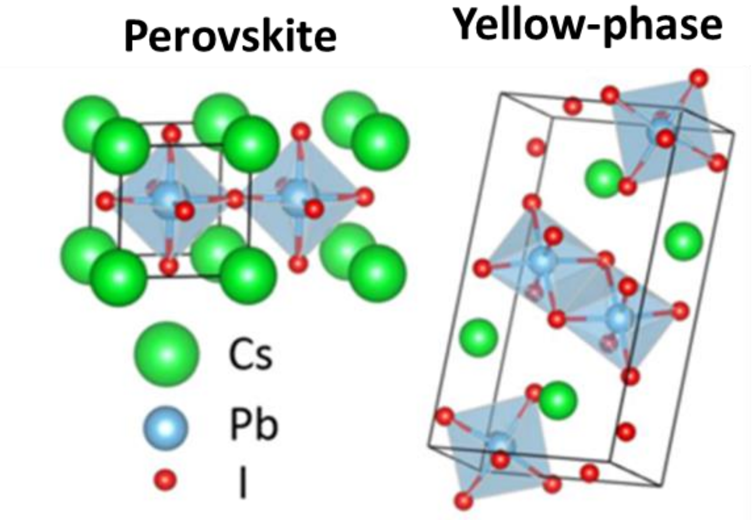

Figure 1.15. Schematics of the perovskite and yellow-phase crystal forms of $CsPbI_3$.[50]

To overcome this phase instability by increasing the tolerance factor, in a similar fashion to what described before for mixed halide perovskites, substitution/addition of larger A-site cations and/or smaller B- or X-site species can be carried out.[51] Partial incorporation of the smaller Br and Cl leads to the formation of mixed I/Br/Cl perovskites that are more thermo-dynamically stable at room temperature.[52],[53],[35] Addition of larger A-site cations (compared to Cs^+), such as MA^+ and FA^+, also results in the stabilization of $CsPbI_3$ at room temperature.[54],[55]Moreover,$CsPbI_3$ can be stabilized by 2D/3D alloying, using organic cations EDA^+, GA^+, BA^+, PEA^+.[56],[57],[58],[59]Additionally, surface post-treatment and interfacial modification are currently applied on both organic–inorganic and all-inorganic wide-E_g PSCs in order to passivate defects on the perovskite surface and facilitate energy level alignment for good charge transport and extraction. By using the CF_3-PEA as surface passivating agent, all-inorganic $CsPbI_{3-x}Br_x$ PSCs achieved a PCE of 18.5% with remarkable operational stability over 2,000 h.[60] Recently, Chu *et al.* reported $CsPbI_xBr_{3-x}$ solar cell with record efficiency of 21.02%, suppressing non-radiative recombination through CsF treatment.[61] Most of these reports are based on solution-processing techniques, while vacuum deposition is less investigated in spite of its benefits, such as good control over the film thickness and composition and simple fabrication of multilayer architectures (described in details in the following section).[62] Vacuum-deposited $MAPb(I_{1-x}Br_x)_3$ films and solar cells have been prepared with 2- and 3-sources processes, where stable films can be obtained only with x up to 0.2 (1.7 eV).[63,64] Mixed-cation and mixed-halide wide bandgap perovskites of the type $FA_{1-n}Cs_nPb(I_{1-x}Br_x)_3$ have been also prepared via vacuum-deposition, either with a 3-source process using PbI_2, CsBr, FAI,[65,66] or with 4 sources and using FAI, CsI, PbI_2 and $PbBr_2$ as the precursors.[67]Gil-Escrig *et al.* fabricated $Cs_{0.5}FA_{0.5}Pb(I_{0.83}Br_{0.17})_3$ photovoltaic devices and further by replacing 20% of the FA^+ with MA^+, triple cation perovskite solar cells with 1.70 eV bandgap were obtained, that significantly improved efficiency up to 16%.[68] Chiang *et al.* found out that an excess of PbI_2 during the deposition leads to high performance p-i-n solar cells with stabilized power output of 18.2%.[66] Regarding the inorganic wide-bandgap perovskites, high efficiencies up to 16% were achieved for vacuum deposited $CsPbI_3$ perovskite film.[69] Zang *et al.* showed that addition of PEAI during thermal evaporation results in stable and efficient solar cells with improved microstructure and reduced density of defects.[70]

Although several advances are being reported in the field of wide-bandgap perovskite solar cells, their performance is still lacking behind narrower bandgap materials. Therefore, it is crucial to further investigate these perovskite formulations in order to reduce charge recombination losses, enhance the phase stability, and hence the efficiencies of the corresponding solar cells.

1.5 Deposition techniques

As mentioned, perovskites are defect tolerant implying that low cost coating methods can be employed. However, to obtain efficient solar cells, it is important that the perovskite layers are homogeneous and crystalline. Different methods are currently employed to form a high quality film and can be divided into two broad categories, solution-processing and vacuum deposition techniques. Depending on the deposition method, the perovskite properties such as morphology, grain size and crystallinity may differ.

1.5.1 Solution-based methods

Prior to processing, the perovskite precursors are dissolved in polar organic solvents such as N,N-dimethylformammide (DMF), dimethyl sulfoxide (DMSO), γ-butyrolactone (GBA) or mixture of them. The solution is then deposited on the substrate using a variety of methods, such as one-step or two-step spin-coating, blade coating or slot-die coating. In one-step spin-coating, the precursor solution is spread onto the substrate and, during rotation, the solvent evaporates and the precursors reacts leading to crystallization of the perovskite. Afterwards, an annealing step is performed to remove the remaining solvent. With this simple method, however, it is very difficult to control the crystallization and morphology of the perovskite film. For this reason, two-steps methods are widely adopted, for example via anti-solvent washing, where a small amount of a less-polar solvent is added on top of the perovskite film during its formation.[71],[72] This additional step controls the crystallization and results in more homogeneous and crystalline films. In sequential deposition methods, the inorganic precursor is spin-coated on the substrate and converted into perovskite either by spin- or dip-coating with a solution of the organic cation. In all cases, the last step is the annealing of the perovskite films, to eliminate the excess solvents and promote the crystallization process.[73],[74]

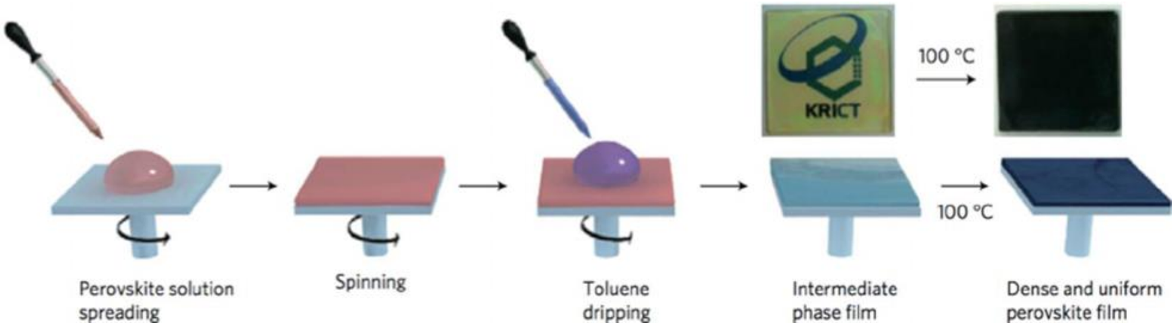

Figure 1.16. Schematic illustration of antisolvent washing procedure.[71]

1.5.2 Vacuum deposition

Vacuum deposition methods are widely applied in the industrial environment for the large scale production of thin film optoelectronic devices, such as organic light-emitting diodes (OLEDs).[75] In the simplest case, it involves the sublimation of chemical compounds by heating under high vacuum. The materials then condense on a cold substrate where, in the case of perovskites, they react crystallizing into the perovskite phase. There are several advantages associated with vacuum deposition when compared to solution-processing:[62],[76]

- Dry processing: eliminates the use of toxic solvents, solubility limitation of precursors and issue of dissolving the underlying layer. In this way facilitating the fabrication of multilayer devices that is crucial for building tandem solar cells.
- Fine control over the film thickness and stoichiometry: quartz crystal microbalances (QCMs) are used to monitor the deposition rate during evaporation with nanometric precision. The composition of vacuum deposited perovskites can be tuned by selecting the evaporation rates of each of the perovskite precursors. Furthermore, it allows the flexibility in terms of materials, deposition of 3D, 2D, multi-cation and mixed halide perovskites is possible.
- Wide substrates compatibility: thermally evaporated perovskites crystallize well already at room temperature, eliminating the need of thermal treatments, which makes them compatible with sensitive and flexible substrates. Vacuum deposition is conformable, hence can be used to coat rough surfaces such as textured silicon, which is important when fabricating tandem devices.

- Large area compatibility: Large area devices can be achieved owing to homogeneity of the layers and possibility of up-scaling the process to industrial scale, as proven by commercial OLEDs TV.
- High purity films: high purity of the used precursors and difference in their sublimation temperatures lead to formation of ultra-pure layers.

Vacuum deposition techniques are classified depending on their complexity:

Single source deposition: The simplest way to deposit thin-films, where pre-formed perovskite is directly sublimed from a single thermal source or a metal electrode in a high vacuum chamber.[77] It is also known as "flash evaporation" since the source temperature is increased fast, allowing the perovskite to rapidly vaporize on a substrate.[78]

Dual source deposition: The most commonly used process, where the organic and inorganic halides are simultaneously thermally sublimed in a high vacuum chamber. The vapors condense and react on a substrate placed above the thermal sources. By controlling the evaporation rates of the precursors, placed in separate thermally controlled ceramic crucibles, the material stoichiometry can be finely adjusted. In 1997. Era *et al.* were the first ones to report 2D perovskite films by dual-source deposition, meanwhile the first example of vacuum-deposited perovskite solar cell was reported by Liu *et al.* in 2013.[79],[80]

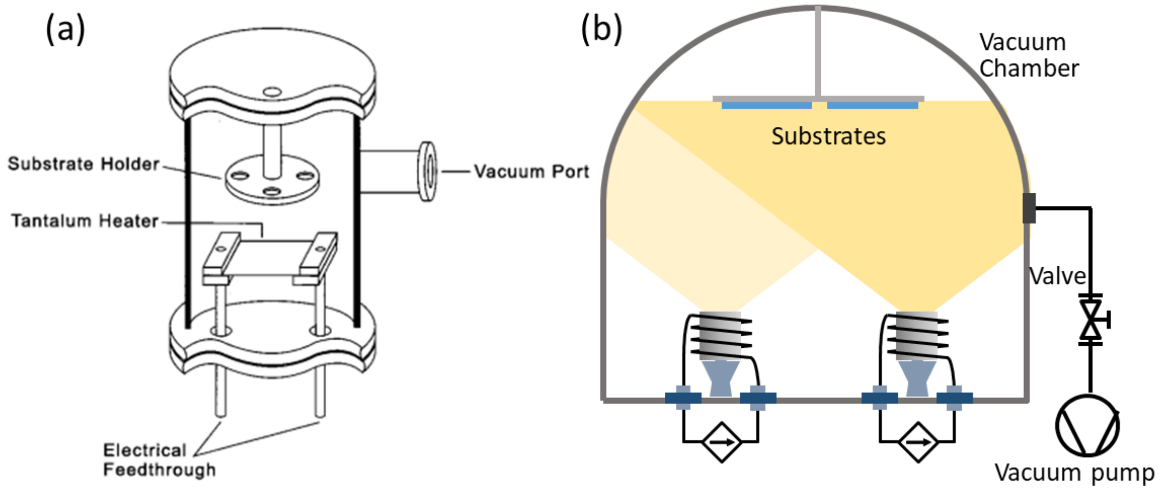

Figure 1.17. Schematic illustration of a) single source thermal deposition chamber and b) dual-source vacuum-deposition.[77]

Multi-source deposition: In order to obtain multi-cation and/or multi-halide perovskites films, vacuum co-deposition from several thermal sources is required, making the process more complex. A high level of control over the deposition rate of each precursor during the film formation is mandatory to obtain homogenous films with the desired stoichiometry. The first reports using multiple thermal sources (3 and 4) to form multi-cations/anions perovskite films were presented by Bolink's group.[63],[68] In these reports, perovskite thin films were prepared by simultaneous thermal vacuum deposition of the corresponding precursors.

Sequential vacuum-deposition: In this approach the perovskite film is deposited layer-by-layer, one precursor after the other, subsequently converting them into the desired compound. Usually, the metal halide layer is deposited first and then converted to perovskite with the organic/inorganic halides, either through vacuum-deposition, vapor exposure or spin-coating of solution of the organic cation.[81],[82]

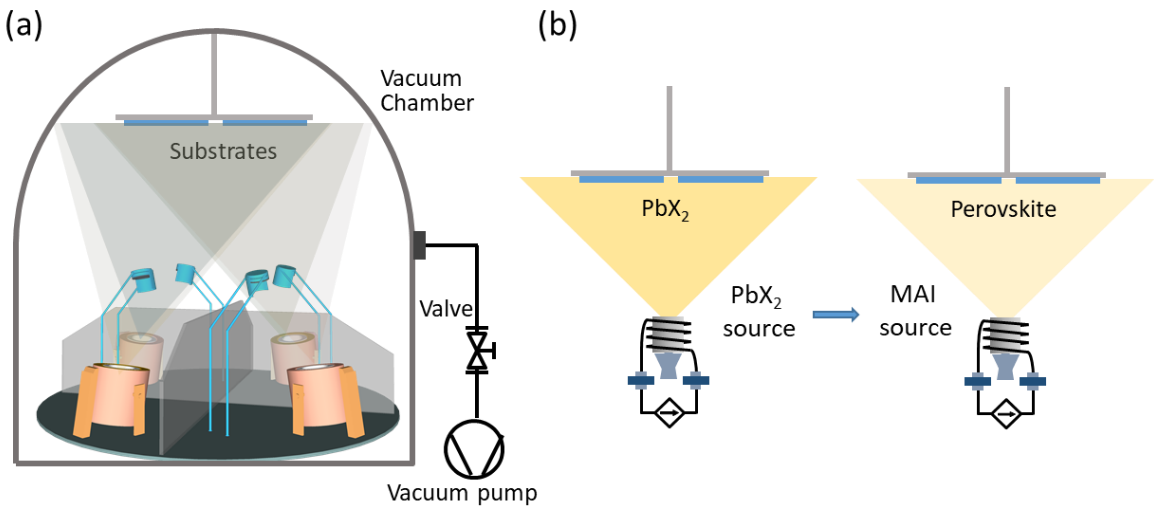

Figure 1.18. Schematic illustration of a) multiple source vacuum-deposition and b) two-step single source vacuum-deposition processes.

In this thesis, multi-source vacuum deposition will be employed in all experiments, and the details of each process will be discussed in the corresponding chapters.

1.6 Device structures

Perovskite solar cell (PSC's) consists of a transparent electrode (usually a conductive metal oxide), a perovskite absorber sandwiched between two selective transport layers that allow charge transport of either electrons (hole blocking) or holes (electron blocking), and a counter electrode. Depending on which transport layer is deposited first on the transparent electrode, in the commonly adopted superstrate configuration we can distinguish two structures: n-i-p, when the electron transport layer is deposited first, and p-i-n, when the hole transport layer is deposited first. n-i-p cells are the most widely adopted structures, where the perovskite layer is deposited on top of the ETL and capped with the HTL and the top electrode. p-i-n cells (inverted structure, Figure 1.19) are increasingly studied in view of their easier integration in tandem solar cells with commercial Si solar cells layout.

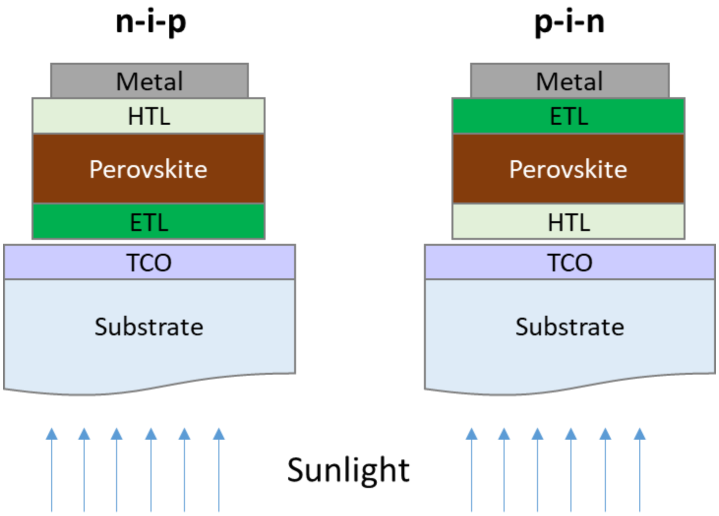

Figure 1.19. Schematic diagram of n-i-p and p-i-n solar cell architectures. Blue arrows indicate the direction of the sunlight.

As previously described, the photo-generated carriers have to be extracted from the perovskite to the electrodes. Therefore, in order to minimize the energy loss during charge transfer, the energy levels of transport layers in perovskite-based devices should be aligned with the valence and conduction bands of the perovskite layer. Both transport layers are typically wide bandgap semiconductors to selectively transport only one type of carrier to the respective electrode, while blocking the other type of carrier (Figure 1.20).

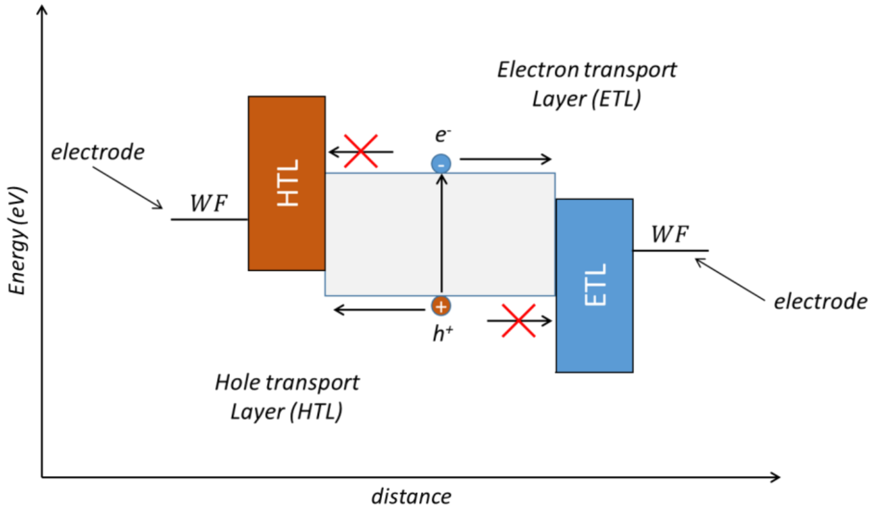

Figure 1.20. Energy band diagram of a typical solar cell with schematic electron and hole extraction.

Moreover, additional doped extraction or injection layers are often utilized to facilitate ohmic contacts at the electrodes and eliminate energy barriers, improving the efficiency of charge extraction and injection. Apart from favourable energy level alignment, the ideal transport material should be thermally and chemically stable with high charge mobility. To date, 2,2’,7,7’-tetrakis(N,N-dip-methoxyphenylamino)-9,9’-spirobifluorene (Spiro-OMeTAD) is the most studied and widely used hole transport material (HTM) in n–i–p perovskite solar cells.[83],[84] In p–i–n devices, the variety of possible HTMs is much larger, but the most common are poly[bis(4-phenyl)(2,4,6-trimethylphenyl)amine] (PTAA) and the inorganic p-type semiconductor NiOx.[85],[86],[87] When using low-molecular-weight organic semiconductors (small molecules) as the HTM, an additional interlayer is often used to increase the work function (WF) of the indium tin oxide (ITO) and ensure ohmic charge injection/collection.[88] Common materials are organic semiconductors with high WF, such as 2,20 -(perfluoronaphthalene-2,6-diylidene) dimalononitrile (F6-TCNNQ), doped layers, or high WF metal oxides, in particular, MoO_3, W_2O_3, and V_2O_5.[89],[90],[91],[92] In the case of electron transport material, commonly used are n-type oxides, in particular TiO_2 and SnO_2, and fullerene derivatives, such as PCBM and C_{60}.[89],[93] Ohmic injection is ensured by depositing a thin interlayer between the ETL and the electrode e.g. 2,9-dimethyl-4,7-diphenyl-1,10-phenanthrolin (bathocuproine, BCP), 1,3,5-tri(*m*-pyrid-3-yl-phenyl) benzene (TmPyPB), (2-(1,10-phenanthrolin-3-yl)naphth-6-yl) diphenylphosphine oxide (DPO), LiF, or n-type metal oxides.[94],[95],[96],[97] The bottom electrode of a PSC is typically a transparent conductive oxide (TCO), either indium tin oxide (ITO) or fluorine doped tin oxide (FTO). The top electrode is commonly metal such as silver, gold and aluminium.

In this thesis, both n-i-p and p-i-n solar cell architectures with different HTL and ETL were prepared and studied.

1.7 Aim of the thesis

The development of efficient wide-bandgap perovskite solar cells that are prepared by scalable techniques is crucial for their application in tandem solar cells. Thus, the aim of this thesis is the development of wide-bandgap perovskite films with improved properties via vacuum deposition, and their subsequent incorporation into highly performing solar cells.

Long deposition time of thermal evaporation leads to a long timeframe to optimize even a single perovskite composition. In **Chapter 3** we present the approach to speed up the development of novel perovskite compositions based on combinatorial vacuum deposition of wide bandgap perovskites, producing more than 100 solar cells with different perovskite absorbers in a single deposition run.

Vacuum processing of multicomponent perovskites is not straightforward, because the number of precursors is in principle limited by the number of available thermal sources. **Chapter 4** introduces the strategy to increase the complexity of the formulation of vacuum-deposited lead halide perovskites films in order to fabricate quadruple-cation perovskite films with enhanced thermal stability.

Many efforts have been focused on the stabilization of the $CsPbI_3$ black perovskite phase by adjusting the tolerance factor. **Chapter 5** demonstrates the vacuum processing of $CsPbI_3$ perovskite films at room temperature, obtained by incorporating the larger salt DMAI. In addition, they are incorporated in fully vacuum processed solar cells, prepared in both the p-i-n and n-i-p configurations.

Chapter 2

Experimental and characterization techniques

2.1 Fabrication of perovskite solar cells

Preparation of the devices was carried out in a class 10000 clean-room with all fabrication processes performed inside a nitrogen-filled glovebox to avoid the presence of oxygen and moisture. In this thesis, the photovoltaic devices were fabricated in both p-i-n and n-i-p configurations, as shown in Figure 2.1. The first step for any fabrication is the substrate preparation, which consists of cleaning the ITO-coated glass substrates with soap, water and isopropanol in an ultrasonic bath, followed by a 20 min UV-ozone treatment. Afterwards, the substrates are transferred to a vacuum chamber integrated into a nitrogen-filled glovebox, which is evacuated to a pressure of approximately 10^{-6} mbar in order to deposit the transport layers.

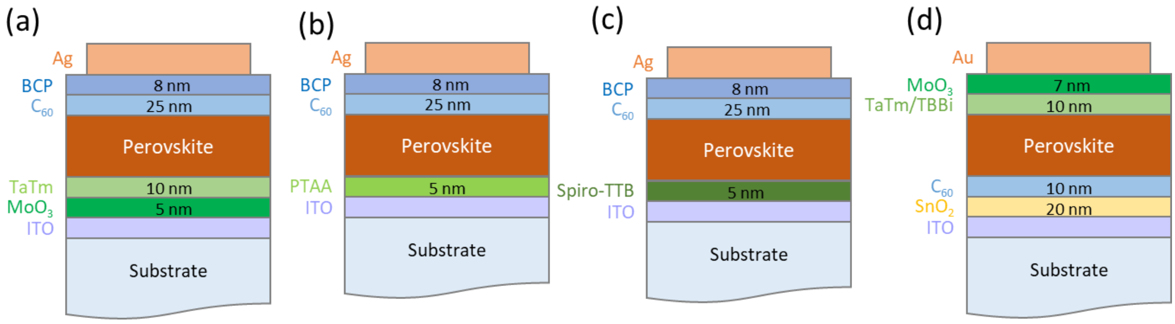

Figure 2.1. Scheme of the p-i-n solar cells employed in (a) Chapter 3, (b) Chapter 4, (c) Chapter 5, and (d) n-i-p solar cells employed in Chapter 5.

In Chapter 3, a p-i-n structure was employed (Figure 2.1a) with MoO_3 (5 nm)/TaTm (10 nm) bilayers used as hole transport layers, where TaTm is N4,N4,N4″,N4″-tetra([1,1′-biphenyl]-4-yl)-[1,1′:4′,1″-terphenyl]-4,4″-diamine. These materials were deposited by vacuum deposition, MoO_3 using aluminum boats as sources and by applying currents ranging from 2.0 to 4.5 A. TaTm was deposited in a second vacuum chamber using a temperature controlled crucible with a deposition rate of 0.5 Å/s. Then the substrates were transferred to a vacuum chamber where a 500 nm thick perovskite film was deposited by multi-source vapor deposition. Devices were finished with the vacuum deposition of electron transport layers, 25 nm thick C_{60} film and 8 nm BCP which is used as a buffer layer. In general, the deposition rate for the C_{60} was 0.5 Å/s while the thinner BCP layer was sublimed at 0.2 Å/s. 100 nm thick Ag is deposited in the same vacuum chamber as MoO_3, from alumina-coated aluminum boats, and by applying currents ranging from 2.0 to 4.5 A.

In Chapter 4, a p-i-n configuration (Figure 2.1b) was fabricated using a thin layer (~ 5 nm) of poly[bis(4-phenyl)(2,4,6-trimethylphenyl)amine (PTAA) as the hole transport layer. PTAA solutions (1.5 mg mL^{-1} in toluene) were spin-coated on the substrates at 3000 rpm and annealed on a hot plate at 100 °C for 10 min. The substrates were then transferred to a vacuum chamber for the perovskite deposition. The devices were finished with C_{60}, BCP and Ag, in the same way as in Chapter 3.

In Chapter 5, both p-i-n and n-i-p configurations were prepared and investigated, as shown in Figure 2.1c and 2.1d. For p-i-n structure, the same fabrication process was performed as in previous Chapters, except that Spiro-TTB (2,2′,7,7′- Tetrakis(N,N′-di-p-methylphenylamino)-9,9′-spirobifluorene) was used as the HTL. 5 nm thick Spiro-TTB films were deposited by vacuum deposition with deposition rate of 0.5 Å/s. In the case of n-i-p configuration the structure was: ITO/SnO_2 (20 nm)/C_{60} (10 nm)/perovskite/TaTm (10 nm)/TPBi (2 nm)/MoO_3 (7 nm)/Au, where TPBi is 2,2′,2"-(1,3,5-Benzinetriyl)-tris(1-phenyl-1-H-benzimidazole). A 20 nm thick layer of SnO_2 was deposited by atomic layer deposition (ALD) using an Arradiance's GEMStar XT Thermal ALD system integrated into a nitrogen-filled glovebox. For that, the ALD chamber was heated to 90 °C; one ALD cycle consisted of consecutive purges of tetrakis(diethylamino)tin (TDAT) for 550 ms and water vapor for 200 ms, each followed by N_2 purges of 30 and 105 s, respectively (final growth per cycle: 1.5 Å). Then a thin layer of C_{60} was deposited in the vacuum chamber with deposition rate of 0.5 Å s^{-1}. The substrates were transferred to another vacuum chamber integrated in a nitrogen-filled glovebox for the perovskite deposition. Afterwards, charge extraction layers were deposited in the same chamber as C_{60}. The deposition rate for TaTm was 0.5 Å s^{-1} and for TPBi was 0.1 Å s^{-1}. MoO_3 and Au were deposited in a third vacuum chamber from alumina-coated aluminum boats, and by applying currents ranging from 2.0 to 4.5 A. The deposition rate of MoO_3 was 0.01 Å s^{-1}, meanwhile Au was deposited at low rate (0.01 Å s^{-1}) for the initial 10 nm and afterwards the rate was increased to 0.1 Å s^{-1}.

2.1.1 Deposition of the perovskite layers

The vacuum deposition of the perovskite was performed using a vacuum chamber integrated in a nitrogen-filled glovebox, whose baseplate is shown in Figure 2.2. The chamber for perovskite deposition is equipped with four evaporation sources and with independent temperature controllers and shutters, located 90 degrees from each other, at a vertical distance of 25 cm from the substrate holder. Each thermal source is equipped with a quartz crystal microbalance (QCM) thickness sensor that monitors the sublimation rate, and a fifth sensor located in the proximity of the sample holder to monitor the overall deposition rate.

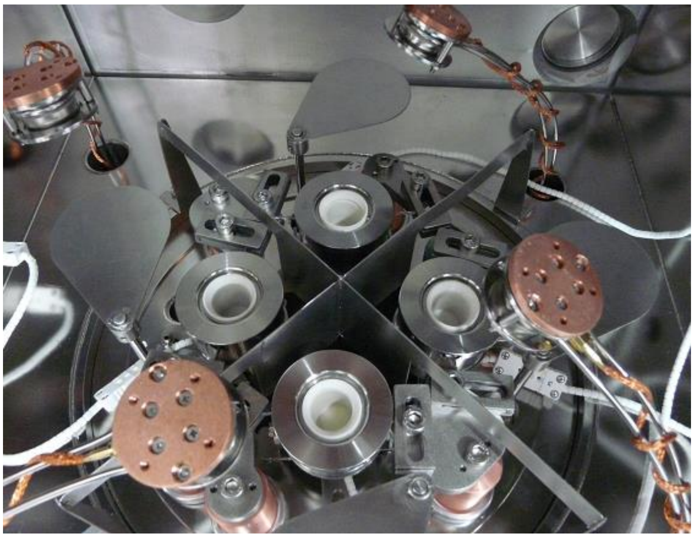

Figure 2.2. Picture of the baseplate of the evaporation chamber employed for the deposition of perovskite thin films.

The substrate holder (Figure 2.3) can accommodate seven 30 x 30 mm^2 substrates. All sources were individually calibrated for their respective materials and no cross-reading between different materials is ensured by the position of the sources, shutters and sensors. Temperature controlled evaporation sources are fitted with ceramic alumina crucibles filled with the desired precursors and the chamber was evacuated to a base pressure of 10^{-6} mbar. The crucibles were heated until they reached the desired deposition rate, subliming simultaneously precursors and forming the perovskite film. The total film thickness of the perovskite was monitored using a fifth QCM sensor placed at the height of the substrate holder. During the perovskite deposition, the pressure of the chamber was maintained at $8 \cdot 10^{-6}$ mbar and the substrates were kept at room temperature. In this thesis, different perovskite formulations were obtained and investigated:

1. $FA_{1-n}Cs_nPb(I_{1-x}Br_x)_3$: four-sources vapor deposition technique using FAI, PbI_2, $PbBr_2$ and CsI as precursors (Chapter 3).
2. CsMAFAGA: multi source vapor deposition technique using MAI, CsI, FAI:GAI mixture and mixed halide $Pb(I_{0.8}Br_{0.2})_2$ as a precursors (Chapter 4).

3. $CsMADMAPbI_3$: four-sources deposition process subliming simultaneously DMAI, PbI_2, CsI, MAI or FAI (Chapter 5).

Deposition rates and details are given in the Experimental section for each chapter.

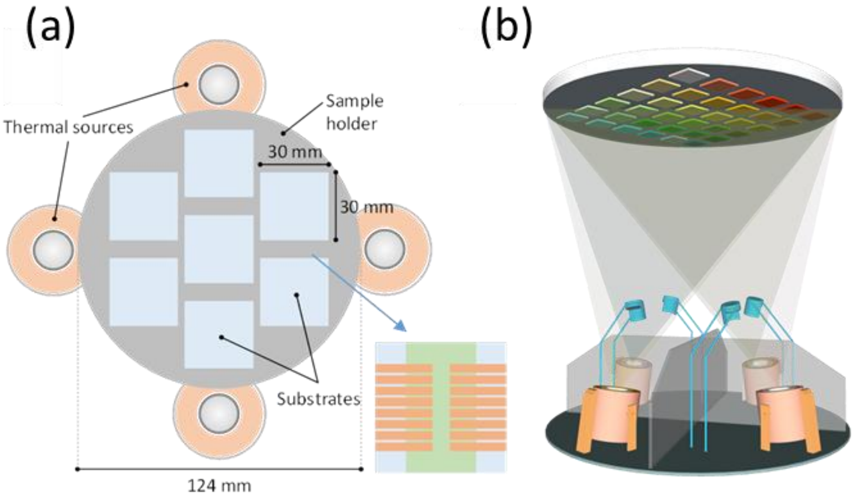

Figure 2.3. (a) Top view of the substrate holder, position of the thermal sources, dimensions and layout of a single substrate. (b) Schematic illustration of evaporation chamber.

All devices were encapsulated by an ALD coating, using an Arradiance's GEMStar XT thermal ALD system integrated into a nitrogen-filled glovebox. The ALD chamber was heated to 40 ºC, while the precursor and oxidizer manifolds (to which the bottles of trimethylaluminum (TMA) and water were connected) were heated to 115 and 140 ºC, respectively, to avoid vapor accumulation at the tubes leading to the main chamber. Prior to deposition, the tubes and valves were degassed three times by performing pulses with the bottles manually closed, to avoid contamination. The substrates were inserted in the chamber, which was then evacuated. A N_2 gas flow of 20 SCCP was used as TMA and water vapor carrier. A cycle consisted of consecutive purges of TMA for 10 ms and water vapor for 30 ms, each followed by N_2 purges for enough time to guarantee complete removal of the precursors from the ALD chamber, as monitored by the transient pressure inside the chamber.

2.2 Characterization techniques

Since the quality of the perovskite layer plays a key role in achieving high photovoltaic efficiency, a reliable and accurate characterization of the thin films is mandatory. In this thesis we performed different characterization techniques:

To start with, the thickness of each layer was measured with a contact profilometer (Ambios XP-1). These measurements allow us to optimize the deposition conditions in order to reach the optimum thickness for each layer.

2.2.1 Optical absorption and photoluminescence spectroscopy

Optical absorption and photoluminescence spectroscopy are important techniques in order to determine the efficiency of light absorption by a given material, the bandgap and the recombination processes. The absorption is quantified by the Beer-Lambert law:

$$A = \log_{10}\left(\frac{I}{I_o}\right) \qquad \text{Equation 2.1}$$

where A is absorbance, I_0 is the intensity of the incident light, and I is the transmitted intensity.

In the photoluminescence spectroscopy, the film is excited by a light beam with photon energy typically higher than the band gap, and the emission spectrum is recorded. By analyzing the PL spectrum, one can get information about the band gap, presence of excitonic peaks and the efficiency of radiative recombination within the film.

In this thesis, measuring the UV-Vis absorption and PL spectrum of the films was done using an Avantes Avaspec-2048 spectrometer. For the PL measurement, films were illuminated with a diode laser from Integrated Optics, emitting at 522 nm. All spectra were collected with an integration time of 1 s. In Chapter 3, optical spectroscopy measurements were performed on 16 points (corresponding to the positions in Figure 2.3). Optical absorption measurements were performed using total transmission (TT) and total reflection (TR) over 400−1000 nm spectral range in N_2 atmosphere. The system is optical fiber-based and consists of a CCD array spectrometer (USB4000, Ocean Optics) and two integrating spheres.[98] The measurement points were circular with a diameter of 3 mm. The absorptance was calculated based on the total transmission and total reflection measurements as A = 100 − TT −TR. Optical bandgaps were calculated from the absorption onset.

2.2.2 X-Ray diffraction (XRD)

XRD presents an important tool for characterizing the microstructure of perovskite films, giving information about crystal structure, phase purity, crystallite size, grain orientation, identification of structural defects, macrostrain, and phase quantity. This technique is based on Bragg’s law that establish a relation between the position of a peak in a diffraction pattern and the distance between atomic planes in the material, described by equation:

$$2d\ \sin\theta = n\lambda \qquad \text{Equation 2.2}$$

where d presents the distance between atomic planes, θ is the angle of the incident X-ray beam with respect to the atomic plane, n is an integer number and λ is the wavelength of the X-ray. Looking at a crystalline material with ordered arrangement of atoms an incident X-ray beam is either scattered or diffracted by the atoms in its path. The formation of a diffraction peak occurs when Bragg's law is satisfied and that is when diffracted rays undergo constructive interference. Phase identification and lattice parameters are obtained from the presence or absence of diffraction peaks, analyzing the peak width and fitting the XRD signal.

In this thesis, the crystallinity of perovskite thin films was analyzed by XRD which were collected at room temperature on an Empyrean PANalytical powder diffractometer using the Cu kα_1 anode operated at 45 kV and 40 mA. Scans were measured in the $2\theta = 8^\circ - 60^\circ$ range in Bragg Brentano geometry, where X-ray source and detector are placed at a fixed radius from the sample in a horizontal plane. Both source and detector are moved at the same time so that incident and diffracted beams leave the sample at the same angle, θ. Further analysis including Le Bail fits were performed with Fullprof software. Microstructural analysis is performed based on these whole-pattern fits, considering instrumental resolution. In short, an instrument resolution file is provided based on previous measurement and analysis of a single crystal. Thus, instrumental broadening is taken into account for microstructural analysis. Whole-pattern Le Bail fits are then performed using a

Thompson-Cox-Hastings pseudo-Voigt line shape. Parameters for the Gaussian and Lorentzian contributions of the pseudo-Voigt function are optimized by fitting of the experimental data. Importantly, these parameters are independent for every different phase present in the diffractograms so that the existence of multiple phases in a single diffractogram is not problematic. Obviously fitting of different diffractograms are also independent. Eventually, average crystallite size and strain values can be derived for every phase of every diffractogram.

2.2.3 Scanning electron microscopy (SEM)

SEM is type of electron microscopy which provide sample's images by scanning the surface with a focused beam of electrons. As a result, information about surface topography, crystalline structure and chemical composition can be obtained. The incident electrons usually have energies of 2-40 keV and in the interaction with the sample produce secondary, back-scattered and X-rays.

Secondary electrons (SE) can only escape from the top few nanometers of the sample's surface due to their very low energies (50 eV). They provide topographic information producing the highest spatial resolution images below 1 nm. Back-scattered electrons (BSE), emitted from the bulk of the sample, have much higher energy then SE. Mostly, they provide compositional information with the resolution of BSE images being less than SE images. When incident electrons remove an inner shell electron from the sample X-rays are produced that are used for elemental analysis. Characteristic X-rays are detected by an energy dispersive spectrometer, providing rapid qualitative analysis of the sample.

In this thesis, SEM images were collected on a Hitachi S-4800microscope operating at an accelerating voltage of 2 kV over samples metalized platinum. However, the SEM images in the Chapter 3 were taken using the HRSEM (FEI, Magellan 400 L) at 4kV and 0.4 nA. The seven samples of $FA_{1-n}Cs_nPb(I_{1-x}Br_x)_3$ compositional spread were deposited on glass and were measured using energy-dispersive X-ray spectroscopy (EDS). The EDS spectra were obtained by an 80 mm^2 X-max detector (Oxford Instruments) coupled to the HRSEM at 30 kV. On each substrate, 16 points corresponding to the positions in Figure 2.3 were measured and then analyzed using the Aztec software (Oxford Instruments).

2.2.4 Solar cell characterization

EQE measurements were performed using a custom-made spectral response setup equipped with a xenon lamp, a grating monochromator and lock-in amplifiers, with chopped light at a frequency of 237 Hz for all cells, and beam size of 2 mm^2. The perovskite cells were continuously illuminated at a defined wavelength and the short-circuit current monitored over time. Since the current is expressed as number of electrons (e) over time and the amount of available photons at every wavelength is known, one can calculate the EQE ratio e/photon.

The J-V curves for the solar cells were recorded using a Keithley 2612A SourceMeter in a -0.2 and 1.3 V voltage range, with 0.01 V steps and integrating the signal for 20 ms after a 10 ms delay, corresponding to a scan speed of about 0.3 V/s. The layout used to test solar cells has 16 equal areas of 0.0825 cm^2 and was measured through a shadow mask with 0.05 cm^2 aperture. The custom-made sample holder and electronics allows to measure all 16 pixels on each device automatically. The devices were illuminated under a Wavelabs Sinus 70 LED solar simulator. The light intensity was calibrated before every measurement using a calibrated Si reference diode. Solar cell stability measurements were recorded using a maximum power point tracker (mppt) system, with a white LED light source under 1 sun equivalent, developed by Candlelight. During the mppt measurements, a flow of N_2 gas was used and temperature was kept at 25 ºC using a water-circulating cooling system. Thermal stability was assessed by leaving the thin films or the encapsulated solar cells on a hot plate at 85 ºC in a nitrogen glove box, and by periodically characterized them ex situ.

Chapter 3

Combinatorial vacuum-deposition of wide bandgap perovskite films and solar cells

The development of vacuum deposited perovskite materials and devices is partially slowed down by the minor research effort in this direction, due to the high cost of the required research tools. But there is also another factor, thermal co-deposition in high vacuum involves the simultaneous sublimation of several precursors with an overall deposition rate in the range of few Å/s. This leads to a deposition time of hours with only a single set of process parameters per batch, hence to a long timeframe to optimize even a single perovskite composition. Here we report the combinatorial vacuum-deposition of wide bandgap perovskites of the type $FA_{1-n}Cs_nPb(I_{1-x}Br_x)_3$, by using 4 sources and a non-rotating sample holder. By using small pixel substrates, we can produce >100 solar cells with different perovskite absorbers in a single deposition run. The materials are characterized by spatially resolved methods, including optical, morphological and structural techniques. By fine-tuning of the deposition rates, we can alter the gradient and reproduce the best performing formulations in standard depositions with rotation. We view this as an approach that can serve as a basis to prototype other compositions, overcoming the current limitations of vacuum deposition as a research tool for perovskite films.

3.1 Introduction

One of the key benefits of using halide perovskites is the ease with which high-quality semiconducting films are made using simple solution-based small-scale methods like spin-coating, but also scalable ones such as slot-die coating.[99] Besides solution-based deposition, high-efficiency perovskite solar cells are increasingly being reported also using physical vapor deposition techniques.[62,100–103] As previously mentioned in Chapter 1.5, vapor deposition processes offer several advantages over solution-based methods, including no dependence on (toxic) solvents and solubility of the precursors, precise control over film thickness,[104,105] and the straightforward fabrication of multilayer architectures. Importantly, thermal vacuum deposition is widely used in the semiconductor industry and can be scaled up to large substrates,[106] moving closer to the commercialization of perovskite solar cells.

Vacuum deposition becomes more challenging when targeting complex perovskite compositions. The simultaneous co-sublimation of perovskite precursors limits the complexity of the perovskite formulation, as the number of thermal sources limits the number of precursors that can be co-sublimed. The development of vacuum deposited perovskite materials and devices is partially slowed down by the minor research effort in this direction, at least when compared with the field of solution-processed perovskites. But there is also another factor, thermal co-deposition in high vacuum (e.g. 10^{-6} mbar) involves the simultaneous sublimation of several precursors with an overall deposition rate in the range of 1-4 Å/s. This leads to a deposition time of > 1 hour (typically 2 hours considering chamber evacuation and venting). Importantly, in typical deposition chambers, in one deposition run only a single set of parameters can be used (i.e., a set of deposition rates for a certain set of precursors). This leads to a long timeframe for optimizing even a single perovskite composition.

Combinatorial materials science (CMS) is a method that can be used to accelerate the study of compositionally varying perovskites.[107] CMS is widely used in the research and development of catalysts, biomaterials, and nanomaterials.[108] When CMS is applied to thin films, a gradient with variation of deposition parameters such as composition, thickness or temperature is deposited on a single large area substrate, referred to as a library, forming a set of experiments or materials in a single deposition run.[109–112] The library of materials is then investigated with spatially resolved high-throughput measurements, to pinpoint those with more interesting physical or chemical properties, which can be later replicated as isolated homogeneous materials. As described by Potyrailo *et al*., the terms “combinatorial materials screening” and “high-throughput experimentation” are typically interchangeably applied for all types of automated parallel and rapid sequential evaluation processes of materials and process parameters that include truly combinatorial permutations or their selected subsets.[113] CMS with high-throughput analysis of the products of the syntheses, have also been applied to the development of halide perovskites. For example, the phase transition of the $CsPb(I_xBr_{1-x})_3$ perovskite was studied using inkjet printing by mixing two precursors solutions with different ratios to form a continuous compositional spread (CCS).[114] Another study concerned the degradation mechanism of the CCS of Br and I in $MAPb(I_xBr_{1-x})_3$ perovskite.[115] Deposition of the CCS using solution-based methods is limited as it depends on solvent polarity, pH, boiling point, and solubility. Solvents play essential roles in controlling not only the solubility, but also the nucleation and growth of the perovskite film.[116] Therefore, systematic changes in composition/precursors also affect the coverage, thickness, and density of the perovskite films.[117] High throughput synthesis has also been used to develop perovskite nanocrystals in a droplet-based microfluidic platform, producing tens of compositions within minutes.[118] Robotic, high throughput synthesis has been applied to the preparation of low dimensional perovskite crystals,[119] as well as to perovskite films.[120] The latter was achieved via a combinatorial synthesis with high-throughput characterization with a high level of complexity and automation. Such platforms are extremely promising for the future development of advanced perovskite formulations, and have already been applied to screen perovskite compositions with state-of-the-art stability in solar cells.[121] Simple perovskite CCS produced by vacuum co-evaporation have also been reported. Compositional gradients have been obtained using two thermal sources with a non-rotating substrate, resulting in linear CCS of two precursors. The compositional gradient formed during evaporation can be systematically reproduced in a controlled process. Simple binary compounds such as $MAPbI_3$,[122] $CsPbI_3$,[69,123] $CsPbBr_3$,[124] have been studied for application in solar cells and light-emitting diodes (LEDs). Yet, only linear compositional gradients of binary compounds have been reported to date.

Here we report the combinatorial vacuum-deposition of wide bandgap perovskites of the type $FA_{1-n}Cs_nPb(I_{1-x}Br_x)_3$, by using 4 sources and a non-rotating sample holder. With an initial set of deposition rates for each precursor, calculated based on the target perovskite stoichiometry, we run a combinatorial deposition and high throughput characterization. By using small pixel substrates, we can produce >100 solar cells with different perovskite absorbers in a single deposition run. The materials are thoroughly characterized by spatially resolved and high throughput methods, including optical, morphological and structural techniques. By subsequent fine-tuning of the deposition rates, we can alter the gradient and reproduce the best performing formulations in standard depositions with rotation. We view this as an approach that can accelerate the discovery of materials, and serve as a basis to prototype other compositions (low bandgap, lead-free), overcoming the current limitations of vacuum deposition as a research tool for perovskite films.

3.2 Experimental section

Materials: *N4,N4,N4',N4'*-tetra([1,1'-biphenyl]-4-yl)-[1,1':4',1'-terphenyl]-4,4'-diamine (TaTm) was provided by Novaled GmbH and fullerene (C_{60}) was purchased from Merck KGaA. PbI_2, MoO_3, and bathocuproine (BCP) were purchased from Luminescence Technology Corp. $CHNH_2NH_2I$ (FAI) was purchased from Greatcell Solar. $PbBr_2$ was obtained from Tokyo Chemical Industry. All materials were used as received.

Thin films and solar cells fabrication: Solar cells with p-i-n structure were fabricated, preparation details are given in Chapter 2. The perovskite was evaporated in the vacuum chamber shown in the Figure 2.2. All sources were individually calibrated for their respective materials and no cross-reading between different materials is ensured by the position of the sources, shutters, sensors. Details of the geometry and deposition rates are provided in the main text. During the perovskite deposition, the pressure of the chamber was maintained at $8 \cdot 10^{-6}$ mbar and the substrates were kept at room temperature. Typical sublimation temperatures for the precursors were 150 °C for FAI, 310 °C for PbI_2, 280 – 300 °C for $PbBr_2$ and 490 - 520 °C for CsI.

3.3 Results and discussion

The vacuum chamber used for this study is shown in Figure 3.1 and described in more details in Chapter 2.1.1. The substrate holder is fixed with respect to the sources (as depicted in Figure 3.1a), and can accommodate seven 30 x 30 mm square substrates to form a CCS of $FA_{1-n}Cs_nPb(I_{1-x}Br_x)_3$. To ensure enough spatial resolution, each substrate is patterned by lithography so that it can accommodate 16 solar cells (defined by the geometry of the top metal electrode using shadow masks, 8.25 mm^2), resulting in 112 measurement points and working solar cells for a single deposition run.

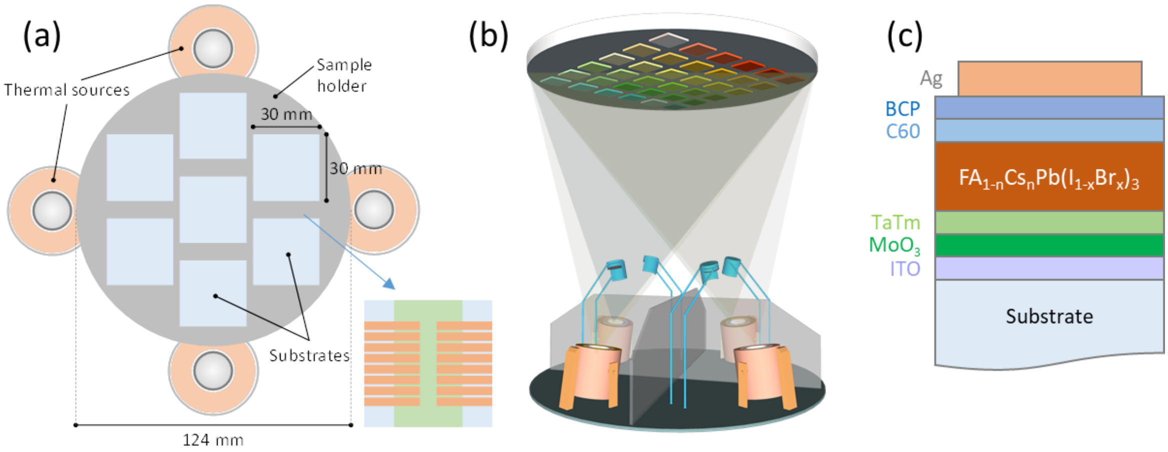

Figure 3.1. Details of the setup and device layout used in the combinatorial study. (a) Top view of the substrate holder, position of the thermal sources, dimensions and layout of a single substrate. (b) Without sample rotation, a gradient of each precursor is deposited on the substrate, resulting in CCS library of thin film perovskites. (c) Device architecture that was used in this study.

We chose to study a well-known wide bandgap halide perovskite, targeting the approximate stoichiometry $FA_{0.6}Cs_{0.4}Pb(I_{0.8}Br_{0.2})_3$, and using FAI, CsI, PbI_2 and $PbBr_2$ as the precursors. The starting deposition rates (r) are chosen by fixing $r(PbI_2)$ at 1 Å/s. Using the PbI_2 density and molecular weight, we calculate the $r(PbI_2)$ in mol/s. Then, the deposition rates (in mol/s) of the other precursors (FAI, CsI, $PbBr_2$) are calculated simply considering the target stoichiometry. Finally, the corresponding deposition rates in Å/s are calculated considering the density and molecular weight of each precursor (Table 3.1). With this set of initial deposition rates, we run the vacuum deposition of perovskite films with a fixed sample holder, obtaining a CCS library because of the gradients formed by each of the 4 precursors (Figure 3.1b). The glass substrates contain patterned ITO, which are coated with MoO_3 (5 nm)/TaTm (10 nm) bilayers used as HTLs. The combinatorial deposition of the perovskite is then carried out until a nominal thickness at the substrate sensor of 500 nm. Samples are finished with a 25 nm thick C_{60} film as an electron transport layer and 8 nm BCP as a buffer layer. 100 nm thick Ag is deposited using a shadow mask to form 16 individual electrodes on each substrate (Figure 3.1c).

Table 3.1. Initial set of deposition rates of the perovskite precursors, calculated taking into account the target stoichiometry of the wide bandgap perovskite $FA_{0.6}Cs_{0.4}Pb(I_{0.8}Br_{0.2})_3$ (**r*(PbI_2) is fixed at 1.0 Å/s as a starting point).

	Molar ratio	**ρ (g/cm^3)**	**MW (g/mol)**	***r* (mol/s)**	***r* (Å/s)**
PbI_2	0.8	6.16	461.01	$1.34 \cdot 10^{-10}$	1.0*
$PbBr_2$	0.2	6.66	367.01	$3.35 \cdot 10^{-11}$	0.2
FAI	0.6	2.22	171.97	$1.00 \cdot 10^{-10}$	0.8
CsI	0.4	0.40	259.81	$6.68 \cdot 10^{-11}$	0.4

We initially analyzed the performance of the perovskite solar cells by measuring all the 112 pixels under simulated solar illumination. Each substrate containing 16 solar cells is measured with a customized automatic system, and the resulting PV parameters for the 7 substrates are depicted as color maps, with the position of each substrate on the holder with respect to the source location. In Figure 3.2, the color maps for the main PV indicators are reported, together with the J-V curves under illumination for each substrate.

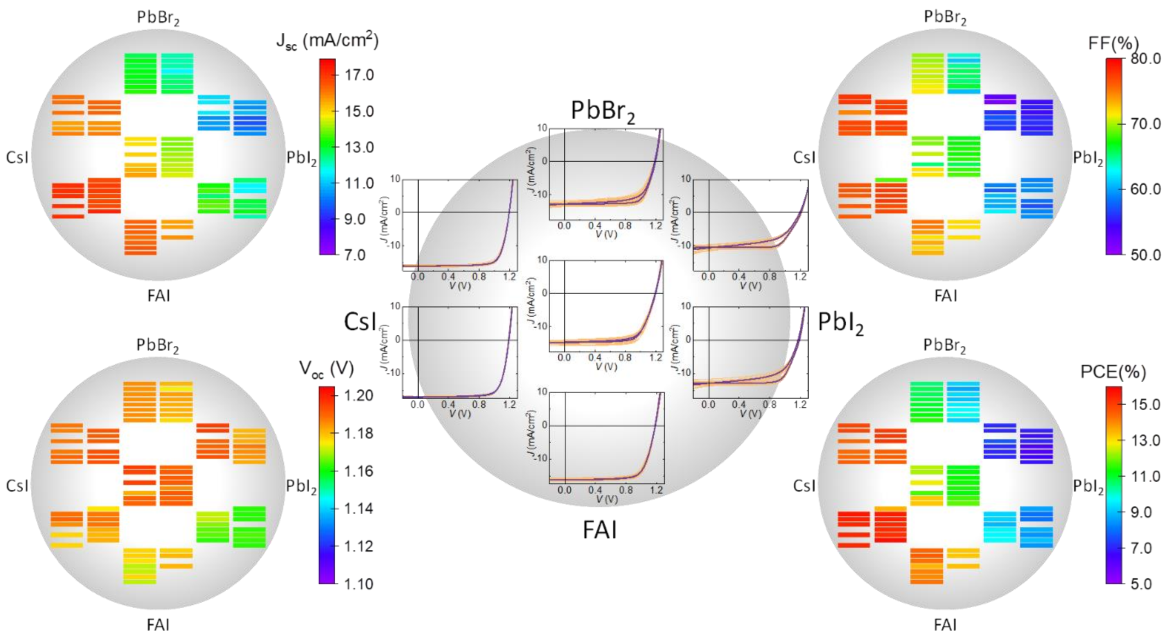

Figure 3.2. Results of combinatorial deposition of wide bandgap perovskite solar cells. 112 points color maps for J_{sc}, V_{oc}, (top) FF, and PCE (bottom) are shown together with the J-V curves for each substrate (the mathematical average of all J-V curves for each substrate are shown as a thick blue line). The deposition rates for PbI_2, $PbBr_2$, CsI and FAI are those reported in Table 4.1 as the initial parameter set.

In Figure 3.2, a gradient of the short circuit current density is clearly visible, with lower photocurrent (approximately 8 mA/cm^2) in pixels located in the vicinity of the $PbBr_2$ and PbI_2 sources, and higher J_{sc} (up to 17 mA/cm^2) for those closer to the CsI and FAI sources. As discussed in more details in the following, this is related to the higher Br^- content in the top part of the map, resulting in wider bandgap perovskites due to increased electronegativity when exchanging I^- with Br^-.[31] This hypothesis is also supported by the trend in open circuit voltage, which is higher (reaching values up to 1.2 V) in the top-central part of the material library. We noticed a slightly lower V_{oc} for the devices near the $PbBr_2$ source, indicating that other loss mechanisms are present in Br-rich materials.[125,126] However, the V_{oc} does not vary substantially within the library, as the minimum values are still in the range of 1.16 V. The fill factor is more directly aligned with the gradient of CsI, as the highest value (approximately 80%) are found in the left side of the sample holder, where the CsI content is expected to be higher.

Samples on the right side of the sample holder, where PbI_2 is sublimed, show hindered charge extraction (FF roughly in the 50 - 60% range), as well as hysteresis in the

J-V curves when measured in forward (short- to open-circuit) and reverse (open- to short-circuit) bias direction. J-V hysteresis is completely suppressed for substrates placed on top of the CsI and FAI thermal sources. The PCE map shows an obvious gradient going from the top right to the bottom left of the sample holder. The lowest values (6-9%) were found for pixels located in the vicinity of the PbI_2 and $PbBr_2$ sources, mainly due to the lower photocurrent and FF. The best performing solar cells are located in the bottom-left part of the maps, with most of the pixels in the 14-15% PCE range.

In principle, we expect the average performance of solar cells on the central substrate to resemble that of devices deposited with the same set of deposition rates, but with a rotating sample holder. Hence, we slightly increased *r*(CsI) from 0.4 to 0.5 Å/s in a second combinatorial deposition, to modify the CCS of the perovskite and analyzed the spatial distribution of the corresponding solar cells characteristics (Figure 3.3).

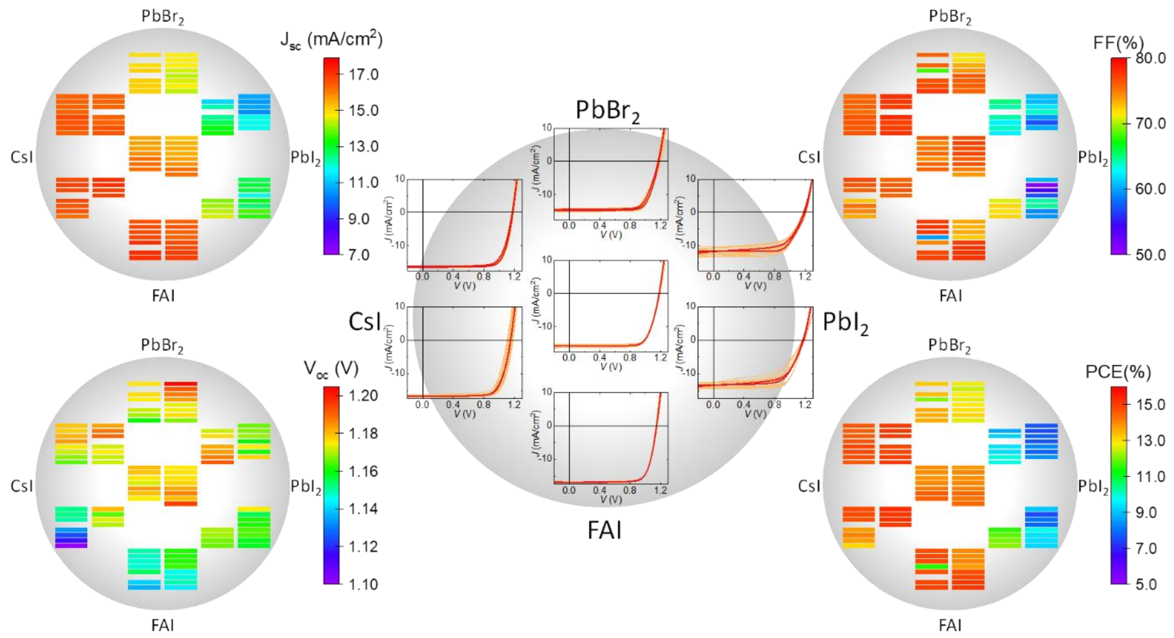

Figure 3.3. Results of combinatorial deposition of wide bandgap perovskite solar cells. 112 points color maps for J_{sc}, V_{oc}, (top), FF, and PCE (bottom) are shown together with the J-V curves for each substrate (the mathematical average of all J-V curves for each substrate are shown as a thick red line). The deposition rates for PbI_2, $PbBr_2$ and FAI are the same as in Figure 4.2, while the *r*(CsI) is increased from (a) 0.4 Å/s to (b) 0.5 Å/s.

One can immediately notice how the gradients in the different color maps are altered upon increasing *r*(CsI). J_{sc} is larger in the central substrate, from 13-14 mA/cm^2 to ≥ 16 mA/cm^2, while the highest values (up to 17 mA/cm^2) are still found for the three substrates placed on top of the CsI and FAI sources (bottom-left part of the map). In these very same substrates, however, the V_{oc} was found to diminish substantially (to 1.10 - 1.12 V), likely a consequence of the high Cs^+ content which can introduce non-radiative recombination channels in the material, as we have previously observed for similar compositions.[68] The gradient of the FF was found to be reduced, with high and rather homogeneous FF (mostly in the 75-80% range) in most of the solar cells, excluding those prepared near the PbI_2 source, that shows hindered charge extraction and low FF as also observed in the previous combinatorial deposition. The resulting PCE map shows that the highest values have been shifted closer to the center of the substrate, as hypothesized above. The solar cells in the central substrate have PCE > 14% on average, while there is more spreading in the pixels of the substrate standing between the CsI and FAI sources (bottom-left). In this substrates, some solar cells show higher (closer to 15%) PCE due to higher J_{sc}, while in other pixels the PCE is reduced due to a low V_{oc}, as previously discussed.

The J-V curves of the central and the bottom substrate show negligible hysteresis and almost no spreading in performance among the individual pixels. On the other substrates of this run, we observe that there is either a spreading in performance among individual pixels, and/or J-V hysteresis. In particular, closer to the PbX_2 source, a more significant spreading, and hysteresis is observed. Using the combinatorial approach, we see that a small change in the deposition rate of a single precursor generates a whole new set of samples with different compositions and solar cell parameters that can be investigated.

The CCS library obtained via combinatorial vacuum deposition of perovskites, as shown in Figure 4.3, has been subsequently characterized by spatially-resolved structural, morphological and optical analysis. Figure 3.4 shows the X-ray diffraction and Scanning Electron Microscopy characterization of different samples obtained without rotation. XRD is typically limited in spatial resolution, hence it was collected by measuring the 4 corners of each of the 7 substrates (28 measurements). Figure 3.4a highlights representative diffractograms for the 7 substrates focusing on the most relevant regions ($2\theta = 12°-15°$ and $2\theta = 27°-31°$ approximately; full diffractograms are given in Figures 3.5).

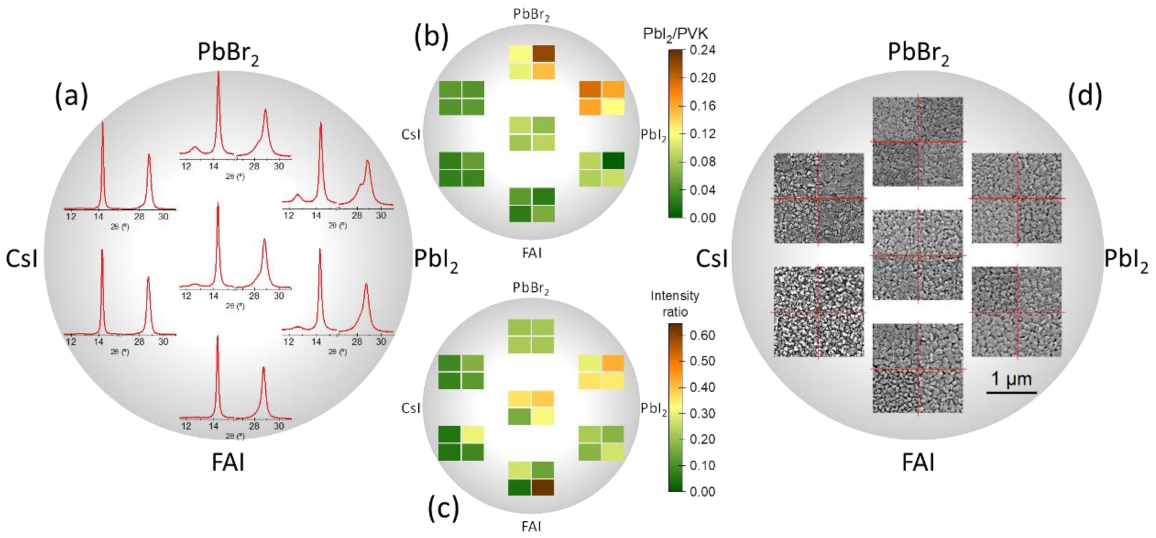

Figure 3.4. Structural and morphological analysis of the material library. (a) Selected XRD patterns for each of the 7 substrates, highlighting the most relevant regions (2θ = 12° - 15° and 2θ = 27° - 31° approximately). (b) Color map of the ratio between the calculated intensities of the (001) peak from PbI_2 (around 2θ = 12.7°) and the (020) peak of the perovskite phase (around 2θ = 14.3°). (c) Color map of the intensity ratio between the sum of (122) and (221) peaks over the main (040) one, where lower values indicate predominance of the higher symmetry cubic phase over tetragonal and/or orthorhombic distortions. (d) SEM images of selected areas of the surfaces of the seven substrates.

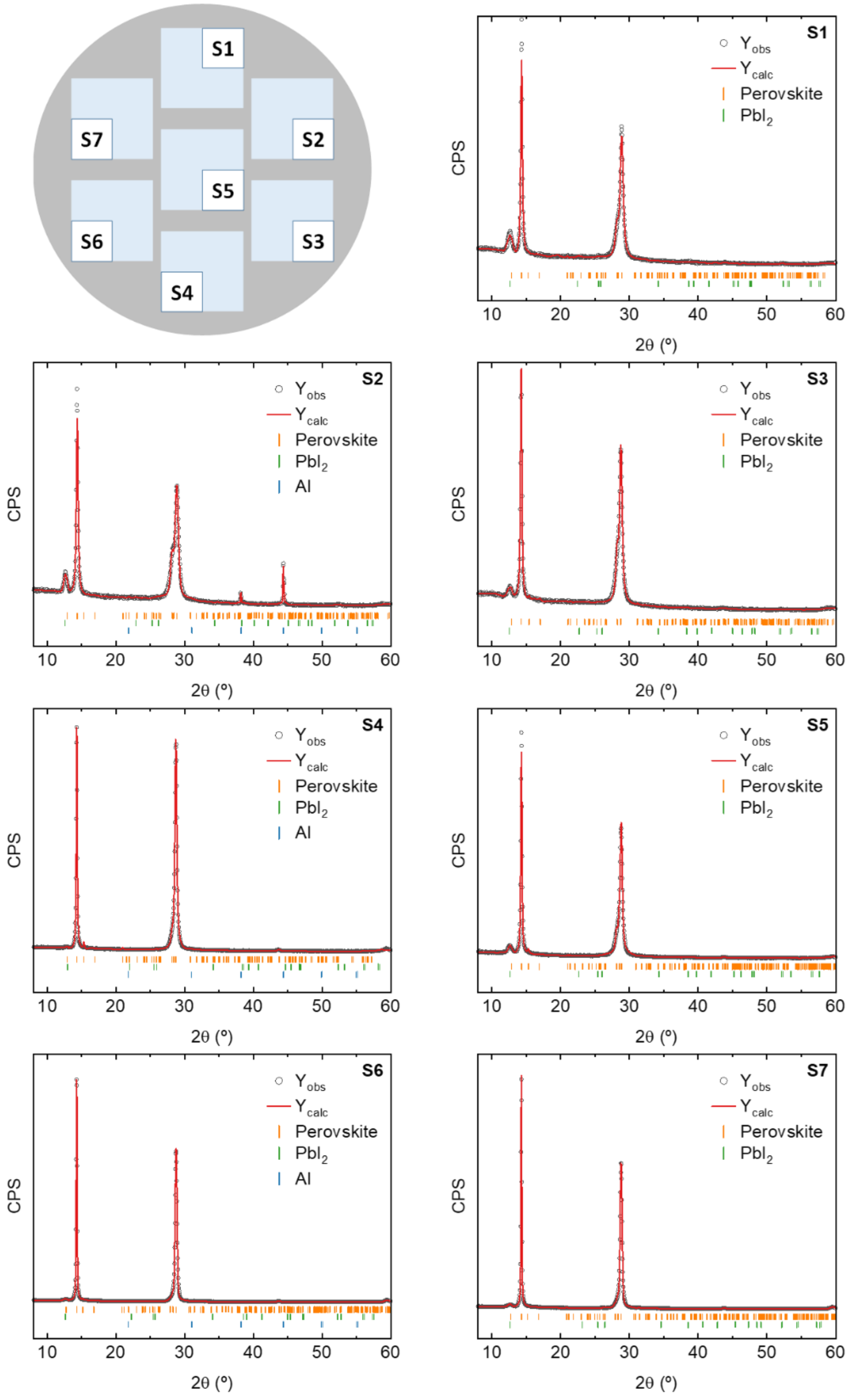

Figure 3.5. XRD patterns for selected corners of the seven substrates on the sample holders, as indicated in the upper scheme. Whole-pattern Le Bail fit (red line) of XRD patterns (open black circles). Vertical markers correspond to calculated Bragg's reflections for perovskite phase (yellow), PbI_2 (green) and Al (blue). The Al reflections come from the ample stage of the XRD tool, and is seen sometimes if the sample is not perfectly aligned with the X-ray beam.

There are clear differences between the bottom-left part closer to the A-cation sources (CsI and FAI) and the top-right part closer to the B-cation sources (PbI_2 and $PbBr_2$), meaning that a gradient in crystallographic properties is established in this case. In particular, two facts can be easily observed qualitatively when moving from the bottom-left (A-rich) to the top-right (Pb-rich) direction: (i) the main signal for crystalline PbI_2 ($2\theta = 12.7°$) relative to the perovskite peaks ($2\theta = 14.3°$ and $2\theta = 28.8°$, approximately) increases, and (ii) the perovskite peaks become broader and split into multiple reflections. The latter observation can be related to PbX_6 octahedra rotation and tilting from the cubic perovskite crystal structure towards a lower-symmetry configuration, as further discussed in the following.[127]

In order to go beyond these qualitative observations, we performed a whole-pattern fit of all 28 diffractograms (4 corners of each of the 7 substrates) for a semi-quantitative analysis. Details of the fitting procedure can be found in the experimental section. Figure 3.4b represents the relative PbI_2/Perovskite signal, which is established as the ratio between the calculated intensities of the (001) peak from PbI_2 (at approximately $2\theta = 12.7°$) and the (020) peak of the perovskite phase (around $2\theta = 14.3°$). These values are obviously related to the relative amounts of crystalline PbI_2 and perovskite in the film. However, due to the high crystallographic texture (preferential orientation) that is typical of vacuum deposited thin films,[128] it is not possible to quantify this ratio. Nevertheless, the semi-quantitative analysis presented in Figure 3.4b clearly highlights the gradient in the PbI_2/perovskite ratio, with noticeably higher fractions towards the Pb-sources, as could be expected. However, we note that the ratio may vary both because of an increase in crystalline PbI_2 and/or because of a decrease in crystalline perovskite (see further discussion on SEM characterization).

In addition, the shapes of the perovskite phase signals differ, as is clearly seen in the range $2\theta = 27°$-$31°$. It is well known that, depending on the exact composition as well as other factors (e.g., temperature) lead halide perovskites can crystallize in a higher-symmetry cubic crystal structure or lower-symmetry tetragonal or orthorhombic structures.[129] Diffractograms will show more distinct peaks when the symmetry of the phase is reduced. To assess this, we fitted all diffractograms considering an orthorhombic perovskite phase (space group = Pnma; $a \approx 8.1$ Å, $b \approx 12.4$ Å, $c \approx 8.3$ Å). This allows more freedom in the whole-pattern Le Bail fit and can lead to good fits even in the case of a cubic phase (the cubic perovskite can be seen as a particular or limited case of the orthorhombic structure, while the opposite is not true). As a result, we are in fact considering three overlapping peaks around $2\theta = 28.1°$, $2\theta = 28.4°$ and $2\theta = 28.8°$, corresponding to the (122), (221) and (040) planes, respectively. Figure 3.4c represents the intensity ratio between the sum of the (122) and (221) peaks over the main (040) one. In the case of a cubic perovskite this ratio should be 0 as only one peak is present. Hence, green pixels represent pure, or higher fraction of a cubic perovskite, and orange/brown pixels represent a higher fraction of lower-symmetry orthorhombic (or tetragonal) perovskites. As explained in Chapter 1, the Goldschmidt tolerance factor can be used to predict lead halide perovskite crystal structures. A low t value (low r_A and high r_B) around 0.7 - 0.8 will generally lead to orthorhombic perovskites, while a higher value of t around 0.9 - 1.0 will lead to cubic perovskites. Here, deriving a value for t is not straightforward given the multi-cation and multi-anion gradients formed in the combinatorial deposition. However, it is significant that, aside from one outlier pixel close to the FAI source, the values in Figure 3.4c are higher towards the Pb-sources (in particular closer to the PbI_2 source) and lower towards the *A*-cation sources. Indeed, this highlights an *A*-cation-deficiency in the top-right part of the sample holder (closer to the PbX_2 sources) that leads not only to higher PbI_2 over perovskite ratios (Figure 3.4b) but also to lower-symmetry perovskites (Figure 3.4c).

SEM characterization (Figure 3.4d) also reveals a more defined morphology towards the *A*-sources and a seemingly more amorphous behavior towards the Pb-sources. This is in good agreement with the XRD characterization. As we previously mentioned, the higher PbI_2/perovskite ratio towards the *B*-sources (Figure 3.4b) may not only come from a higher amount of crystalline PbI_2 in the film, but also from a lower amount of crystalline perovskite. When the diffractograms are overlapped without normalization (Figure 3.6), it is noticeable that the perovskite peaks are significantly more intense in samples that are closer to the A-cation sources (CsI and FAI). As all diffractograms are acquired with identical instrumental conditions, it is reasonable to ascribe the higher intensity to a higher fraction of crystalline (versus amorphous) perovskites in these samples.

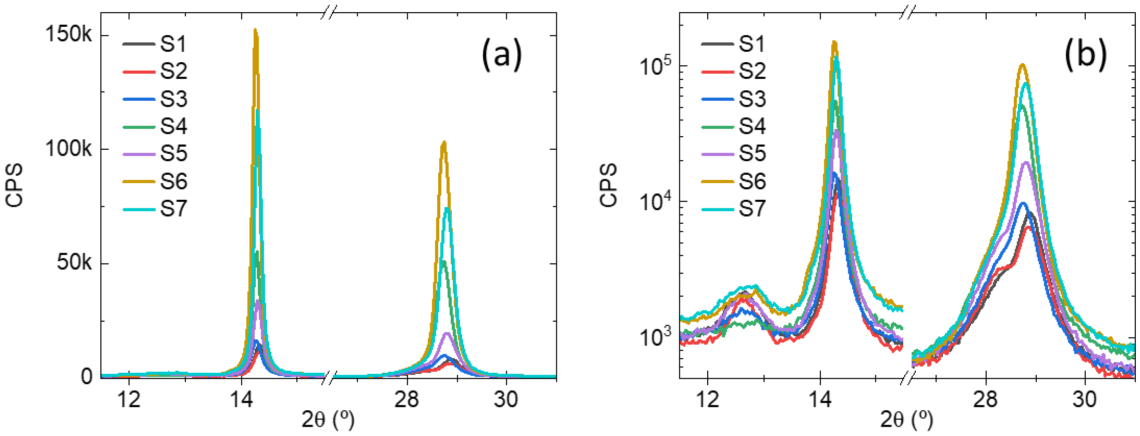

Figure 3.6. XRD patterns (same locations as in Figure 3.5) overlapped without normalization in (a) linear and (b) semi-logarithmic scale.

In summary, Figure 3.4 reveals a gradient in structural and morphological properties. Overall, a dominant perovskite phase is observed in all films with a minor contribution from PbI_2. In this sense, the crystallization is not highly inhomogeneous. Nevertheless, subtle differences generally point towards a deficiency of *A*-cations towards the PbX_2 sources, which leads to poorer morphology and crystallinity.

We then studied the optical properties of the material library, such as optical bandgap and photoluminescence quantum yield (PLQY), and correlated them with elemental composition. Figure 3.7a shows the E_g map extracted from the onset of the optical absorption of the films, measured at 112 points in the exact same position as the solar cells described in Figure 3.3 (selected absorption and PL spectra for each substrate are shown in Figure 3.7c). A clear E_g gradient can be observed in the map, with lower values (1.7 eV) close to the FAI source, increasing towards the center of the sample holder (1.73 - 1.74 eV), and maximum E_g values ≥ 1.76 eV in the films deposited near the $PbBr_2$ source, on the top of the map. This small variation across the holder would have been ignored unless high throughput measurements were performed to give high-resolution maps, showing a clear bandgap trend moving from the A-cation sources to the PbX_2 sources.

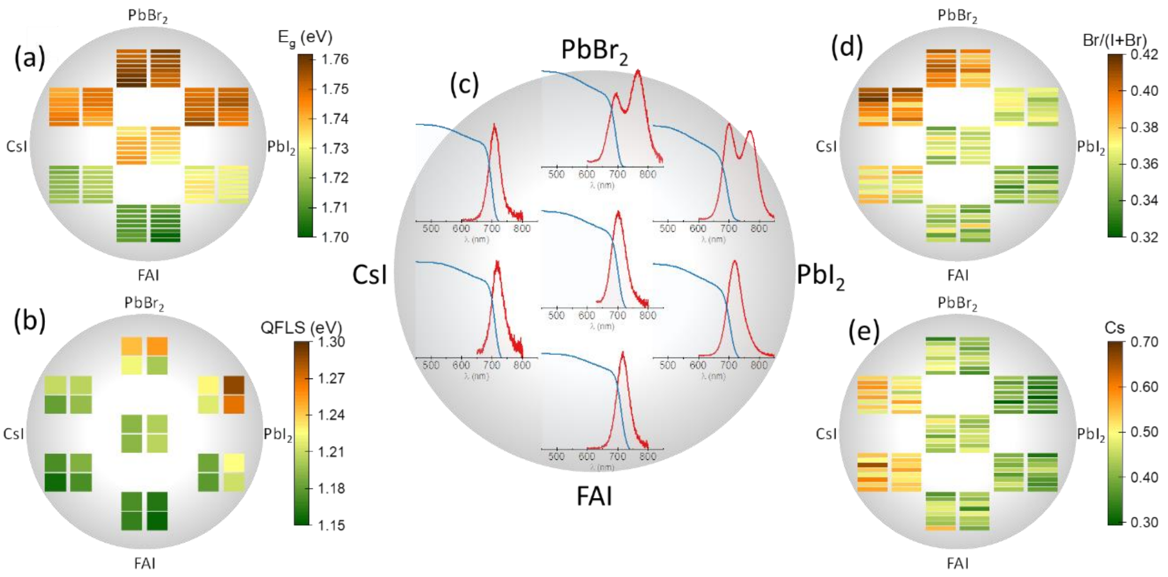

Figure 3.7. Optical and elemental characterization of the library of materials. (a) Bandgap (E_g) color map extracted from spatially resolved optical absorption. (b) PLQY map, measured at the corners of each substrate. (c) Representative absorption (blue) and PL (red) spectra for each substrate. EDS color map of (d) Br/(Br+I) and (e) Cs/Pb concentration ratios.

While E_g seems strongly related with the bromide content in the perovskite (as seen from the vertical gradient of the map in Figure 3.7a), a slight but apparent horizontal gradient can also be observed: in the bottom part of the sample holder, the materials grown closer to the PbI_2 source (right) have larger E_g ($\geq$ 1.73 eV) as compared to those near the CsI source (left, 1.71 - 1.72 eV). This might appear counterintuitive, however, partially converted perovskites (with residual PbX_2 phase) have been reported to show a wider bandgap as compared to the same phase-pure perovskite.[130] Here, the perovskite films in the vicinity of the PbI_2 source have a lower crystallinity and higher PbI_2/perovskite intensity ratio, as observed by XRD (Figure 3.4a-b). This implies a lower degree of conversion of the precursors into perovskite, hence a wider E_g.

We have also measured the elemental composition of the materials library by energy-dispersive X-ray spectroscopy in an SEM, for the same position where the E_g was estimated. Figure 3.7d shows a map of bromide ratio, expressed as the bromide concentration normalized for the sum of iodide and bromide content, while Figure 3.7e shows the Cs/Pb ratio map. Cs and Br were chosen because only one source is depositing these elements, allowing the effect of deposition without rotation and source location to be evaluated readily.

The Cs content decreases gradually from perovskites grown closest to the CsI source, to those farthest away and close to the PbI_2 substrate, leading to a clear horizontal gradient in the EDS map (Figure 3.7e). The gradient in the bromide mapping (Figure 3.7d) is not completely aligned with the E_g gradient (Figure 3.7a), suggesting a preferential bromide adsorption in Cs-rich formulations, and a lower intake for Pb-rich materials. Also, the bromide differential concentration over the whole material library is small (10% variation), while the Cs concentration decreases from 70% (near CsI) to 30% (far from CsI). These observations indicate a different evaporation cone for the two materials: that of CsI is more directional, with most of the Cs being incorporated in the films directly on top of the CsI thermal source, while that of $PbBr_2$ distributes more homogeneously over the whole substrate holder.

Calibrated, absolute PL measurements were also carried out on the 4 corners of each of the 7 substrates, allowing to map the PLQY over the material library. The PLQY map (Figure 3.7b) shows a clear trend, with Cs-rich compositions showing the lowest values (approximately 10^{-5}), and rising luminescence efficiency for materials on the right side of the sample holders, more rich in PbI_2. In all cases, however, the PLQY is low (maximum around $3 \cdot 10^{-4}$), indicating the presence of non-radiative recombination channels in the perovskite bulk or at its surface.[131–133] An important observation needs to be made regarding the PL spectra and the corresponding PLQY: the PLQY is calculated from the integrated intensity of the whole PL spectrum, and hence it contains all contributions arising from impurities or phase segregation. Considering the PL spectra reported in Figure 3.7c for each substrate, we can indeed observe that the PL spectra show two components for samples in the top-right part of the sample holder. This is a signature of the perovskite demixing into bromide-rich and iodide-rich domains, commonly referred to as halide segregation.[134–136] This effect is photoinduced and dynamic, and is only observed here for perovskite formulations which are lead bromide-rich and Cs-poor (Figure 3.8), in agreement with previous reports.[137]

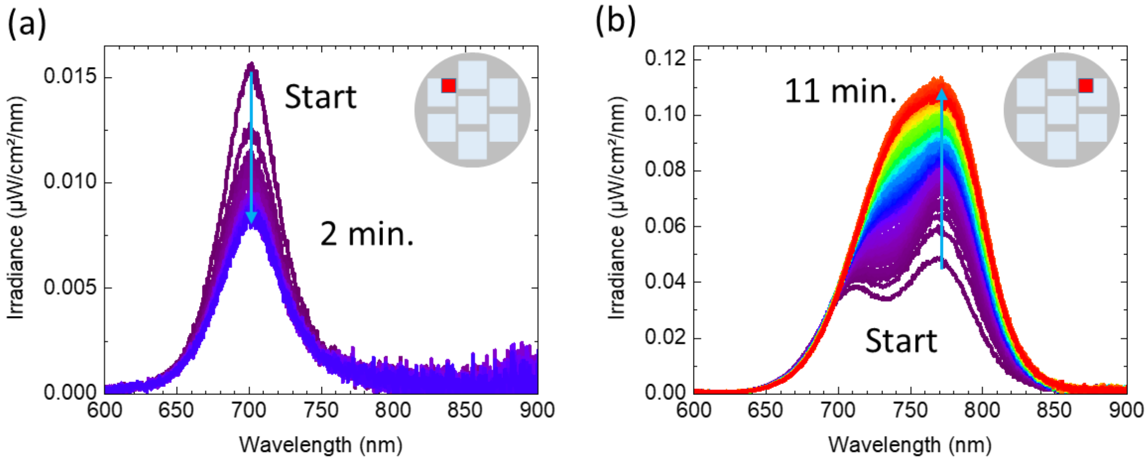

Figure 3.8. PL spectra for perovskite thin films at different locations of the material library (position in the sample holder is highlighted in the inset), showing (a) stable PL shape and (b) peak splitting due to photoinduced halide segregation. Samples are excited with a 522 nm CW laser with an intensity corresponding to approximately 1 sun.

As a matter of fact, the sample with the higher bromide content (top-left in Figure 3.7d) does not show any detectable halide segregation (Figure 3.7c), because of its equally high Cs concentration (Figure 3.7e). From the PLQY map, the quasi-Fermi level splitting was estimated using the reciprocity relation.[138] The QFLS map (Figure 3.9, where it is compared with the corresponding measured V_{oc}) shows a clear trend, increasing from 1.15 eV (bottom-left) to 1.25-1.30 eV in the top-right part of the material library. The QFLS gradient is a combination of the vertical gradient in bandgap and the horizontal gradient in PLQY. This trend agrees with the V_{oc} observed in the devices, the lowest values being those of solar cells prepared in between the CsI and FAI sources. The outliers in the top-right substrate of the QFLS map (highest QFLS values approaching 1.3 eV in Figure 3.9) are consequence of the PL peak splitting described above, which makes the QFLS calculation incorrect and is detrimental to the V_{oc} of the solar cells.

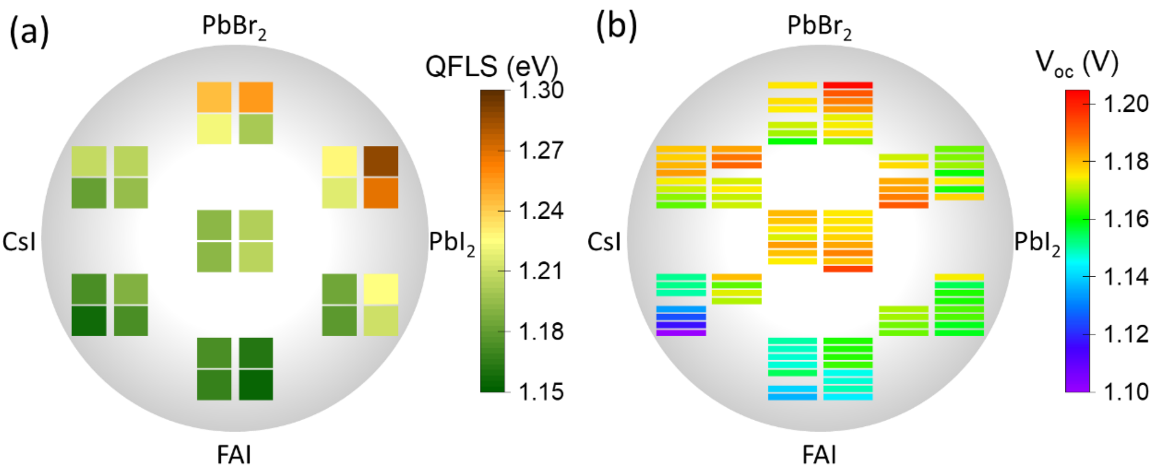

Figure 3.9. (a) QFLS map calculated from PLQY measurement on perovskite films using the reciprocity relation and (b) V_{oc} map for solar cells obtained with the same deposition parameters: $r(PbI_2)$ = 1.0 Å/s; $r(PbBr_2)$ = 0.2 Å/s; r(FAI) = 0.8 Å/s; r(CsI) = 0.5 Å/s.

To briefly summarize, using CMS together with vacuum deposition we were able to deposit a CCS library, where the gradients are directly controllable by the deposition rate of each precursor. This approach shows great potential for the development of novel perovskite formulations by multi-source vacuum deposition. We observed, in a single combinatorial deposition run, several features of the $FA_{1-n}Cs_nPb(I_{1-x}Br_x)_3$ perovskite family, which otherwise would have taken several batches to be identified. Among these, Cs-rich wide bandgap formulations are found to be more crystalline and with a more defined morphology, resulting in high J_{sc} and FF. However, the same Cs-rich perovskites have lower PLQY, leading to a higher V_{oc} loss in solar cells. While Cs-rich formulations have a high symmetry crystal structure (cubic), Cs-poor and Pb-rich perovskite are more disordered, with lower symmetry tetragonal or orthorhombic phases. Pb-rich perovskites with unconverted PbI_2 precursors show a wider bandgap as compared to phase pure perovskites. Also, as expected, halide segregation is observed only when high concentration of bromide is not compensated by sufficient Cs in the perovskite structure.

The combinatorial deposition can also be directly applied to the development of optoelectronic devices. As we showed in Figure 3.3, tuning the deposition rates shift the gradients accordingly. To explore the potential of this method, we performed another deposition run, using the same parameter set used in Figure 3.3, but this time with sample rotation. In a first approximation, the central substrate sees similar deposition rates for the different precursors in a deposition with and without rotation. The performance of the corresponding perovskite solar cells is reported and compared with that of devices obtained without rotation (central substrate in Figure 3.3).

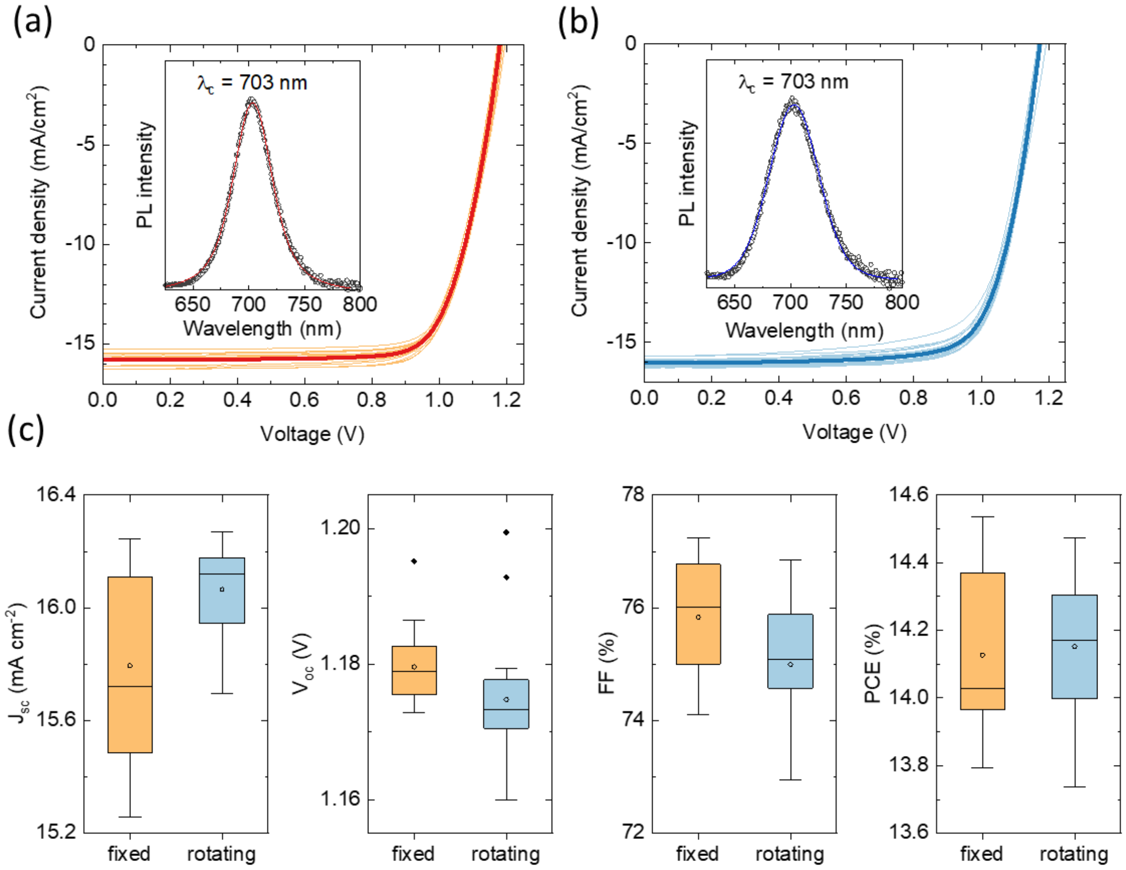

Figure 3.10. Comparison of solar cells obtained with fixed and rotating sample holders. (a) J-V curves under illumination for solar cells in the center of a non-rotating (fixed) sample holder and (b) J-V curves under illumination for solar cells obtained in a controlled deposition with sample rotation (the J-V curves for two substrates, one on the center and one on the edge of the sample holder are reported). Light colors indicate J-V curves for each single pixel, while the thick lines are the mathematical average of all J-V curves. The inset in (a) and (b) show the PL spectra fitted with a Voigt function to quantify the peak center. (c) Distribution of the PV parameters for the two sets of solar cells, obtained without and with sample rotation. The same deposition rates are used: $r(PbI_2)$ = 1.0 Å/s; $r(PbBr_2)$ = 0.2 Å/s; r(FAI) = 0.8 Å/s; r(CsI) = 0.5 Å/s.

Figure 3.10a shows the J-V curves under illumination for the central substrate obtained without rotation, and Figure 3.10b those for the solar cells obtained with rotation.

In the latter, we show the J-V curves for two substrates, one in the center of the sample holder, the other on the edge (to check for the homogeneity induced by the sample rotation). The PL spectra of the perovskites obtained with each method is reported as an inset, and fitted with a Voigt function to extract the peak center. A summary of the PV parameters for both batches of devices is reported in Figure 3.10c. The material properties appear to be similar, as the center of the PL spectra of the two batches is exactly at the same wavelength (only a small deviation in the peak width can be observed). Solar cells prepared with the two methods behave similarly in absolute values, especially when looking at V_{oc}, FF and resulting PCE. The main difference can be seen in the spread of the J_{sc}, which is larger for the solar cells prepared without rotation. This was already seen in Figure 3.3 and is expected in view of the bandgap variation induced by the gradient in chemical composition, also reported in Figure 3.7a. The similarity of the two samples teaches us that the middle sample on the holder can be compared to a rotating sample. Additionally, Figure 3.11 shows the statistics of the power conversion efficiency from perovskite solar cells prepared with rotation in 3 different batches, confirming the good reproducibility of corresponding solar cells. By placing more samples on the fixed holder, we can exploit the deposition to study more compositions, accelerating the progress of vacuum deposited halide perovskite research.

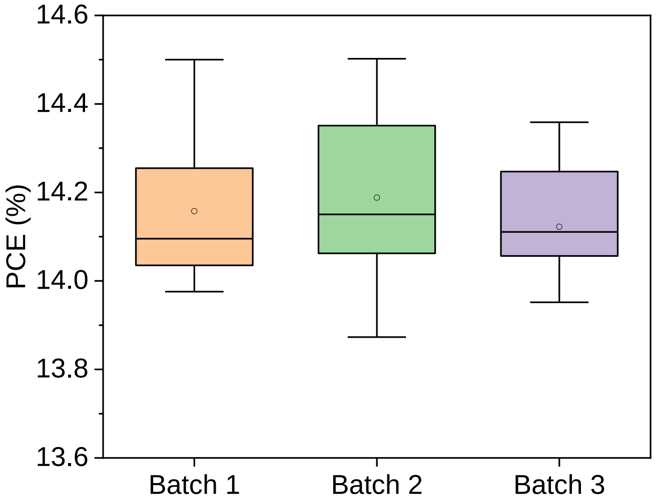

Figure 3.11. Statistics of the power conversion efficiency from perovskite solar cells prepared with rotation in 3 different batches.

3.4 Conclusions

We applied CMS on vacuum deposition process to the screening of lead halide perovskite formulations starting from 4 precursors placed in different thermal sources. By fixing the sample holder and spatially analyzing the performance of the solar cells and the material properties, we are able to extract a large amount of information and screen a wide parameter space in a single deposition run. As a model system, we targeted the wide bandgap perovskite of the type $FA_{1-n}Cs_nPb(I_{1-x}Br_x)_3$, which can be vacuum-processed starting from FAI, CsI, PbI_2 and $PbBr_2$. Several properties of this family of materials have been identified in a single combinatorial deposition run, in contrast to standard vacuum deposition experiments with rotating sample holder where only one set of parameters can be studied for each batch. CCS can be fine-tuned by adjusting the deposition parameters, and solar cells obtained in the central substrate (with equal distance from the 4 thermal sources) resemble closely those obtained with the same deposition parameters but with sample rotation, which is routinely used for the fabrication of perovskite solar cells. This feature can speed up substantially the development of novel perovskite composition: high throughput experiments can be carried out with a fixed substrate holder, the deposition rates can be adjusted by shifting the desired materials parameters towards the center of the sample holder, and finally this set of parameters can be used in a standard deposition process with sample rotation. We envision this route as the direction to take for the future development of vacuum-processed multi-component optoelectronic devices.

Chapter 4

Quadruple-cation wide bandgap perovskite solar cells with enhanced thermal stability enabled by vacuum deposition

Vacuum-processing of multi-component perovskites is not straightforward, as the number of precursors is in principle limited by the number of available thermal sources. Here we present a process which allows to increase the complexity of the formulation of vacuum-deposited lead halide perovskite films by multi-source deposition and pre-mixing both inorganic and organic components. We apply it to the preparation of wide bandgap $Cs^+/MA^+/FA^+$ (herein named CsMAFA) triple-cation perovskite solar cells, which are found to be efficient but not thermally stable. With the aim of stabilizing the perovskite phase, we add guanidinium (GA^+) to the material formulation, and obtained $Cs^+/MA^+/FA^+/GA^+$ (herein named CsMAFAGA) quadruple-cation perovskite films with enhanced thermal stability, as observed by X-ray diffraction and rationalized by microstructural analysis. The corresponding solar cells showed similar performance with improved thermal stability. This work paves the way towards the vacuum-processing of complex perovskite formulations, with important implications not only for photovoltaics but also for other applications.

4.1 Introduction

An important feature of perovskites is the possibility to fine tune their bandgap by compositional engineering,[32,139–141] making them suitable for single- and multi-junction solar cells.[142–148] As described in Chapter 1.4. regarding tandem devices, perovskite compositions with wide bandgaps > 1.65 eV are obtained by using mixed iodide/bromide formulations, where mixed A-site cations are typically employed to improve the photo- and thermal stability of the compounds.[34,36,44,134,149–151] Apart from mixed-cation and mixed-halide wide bandgap perovskites of the type $FA_{1-n}Cs_nPb(I_{1-x}Br_x)_3$ that have been prepared via vacuum deposition, Gil-Escrig *et al.* showed that wide-bandgap $Cs_{0.5}FA_{0.4}MA_{0.1}Pb(I_{0.83}Br_{0.17})_3$ perovskite films can be prepared in a 4-sources co-sublimation process, from PbI_2, CsBr, FAI and MAI precursors, where CsBr was used simultaneously as the source of Cs^+ and Br^-.[68] However, in order to increase the bandgap (E_g > 1.7 eV), substantial amount of Br^- had to be incorporated, resulting in an equally large cesium concentration. The excess of cesium was found to cause an irregular morphology, leading to poor device performance.[68] Recently, Igual- Muñoz *et al.* demonstrated the possibility to sublime mixed metal halide precursors from a single source, by pre-alloying two precursors via melting them in nitrogen atmosphere at ambient pressure.[152] This strategy liberates one thermal source which can be used to add another component in the perovskite deposition process.

In this work we demonstrate the vacuum-processing of triple-cation CsMAFA perovskite films from 4 sources, subliming simultaneously CsI, MAI, FAI, and a pre-alloyed mixture of PbI_2 and $PbBr_2$. This process leads to homogeneous perovskite films which can translate into efficient wide bandgap perovskite solar cells. However, the perovskite films and devices were found to be thermally unstable upon stressing at 85 °C. Hence, with the aim of stabilizing the structure of the CsMAFA perovskite, we added a fourth A-site cation. Guanidinium (GA^+) has been reported to stabilize both FA- and MA-based perovskites,[153–158] due to an increased number of H bonds with favorable orientation within the inorganic framework.[153] In addition, GA^+ can be incorporated (to a certain extent) in a lead halide perovskite lattice without braking the 3D structure, as its ionic radius (278 pm) is only slightly larger as compared to FA^+ (253 pm).[155] To add yet another component, we took advantage of the similar sublimation properties of GAI and FAI, and sublimed them together from a single thermal source. This led to a 4-source deposition process with 6 precursors, namely CsI, MAI, FAI, GAI, PbI_2 and $PbBr_2$, with FAI/GAI and $PbI_2/PbBr_2$ sublimed from single sources. The as-prepared films were found to be highly stable upon thermal stress and light soaking, and the corresponding solar cells show PCE similar to that of the triple-cation counterpart. Importantly, the thermal stability of the perovskite composition translates to solar cells with long lifetime at 85 ºC, comparable to best in class pure iodide perovskites prepared by vacuum deposition.

4.2 Experimental section

Materials: Poly(triaryl)amine (PTAA), fullerene (C_{60}) and $C(NH_2)_3I$ (GAI) were purchased from Merck KGaA. PbI_2, CH_3NH_3I (MAI) and bathocuproine (BCP) were purchased from Luminescence Technology Corp. $CH(NH_2)_2I$ (FAI) was purchased from Greatcell Solar. $PbBr_2$ was obtained from Alfa Aesar. All materials were used as received.

Thin films and solar cells fabrication: Devices were made in p-i-n configuration as described in the Chapter 2. Regarding the perovskite deposition, the substrates were transferred to a vacuum chamber integrated in a nitrogen-filled glovebox and evacuated to a pressure of 10^{-6} mbar. For thickness calibration, we individually sublimed each material, and a calibration factor was obtained by comparing the thickness inferred from the QCM sensors with that measured with a mechanical profilometer (Ambios XP1). During the perovskite deposition, the pressure of the chamber was maintained at $8 \cdot 10^{-6}$ mbar and the substrates were kept at room temperature. Typical sublimation temperatures for the precursors were approximately 155 ºC for FAI or FAI:GAI (r = 0.6 Å s^{-1}), 125 ºC for MAI (r = 0.3 Å s^{-1}), 310 ºC for $Pb(I_{1-x}Br_x)_3$ (r = 1.3 Å s^{-1}), and 485 ºC for CsI (r = 0.4 Å s^{-1}). The FAI:GAI mixture was prepared by weighting 1 g of FAI and 0.11 g of GAI in a vial, and by mixing them with a SpeedMixer^{TM} (DAC 150.1 FVZ) for 5 minutes at 3500 rpm. After mixing, they are transferred to the alumina crucible used for the sublimation. The mixed halide precursor $Pb(I_{0.8}Br_{0.2})_2$ was prepared by mixing in an alumina crucible 1 g of PbI_2 and 0.2 g of $PbBr_2$, and by heating them at 350 ºC for 5 minutes after complete melting of the mixture.

4.3 Results and discussion

Triple-cation perovskite films were prepared from 4 sources, subliming simultaneously CsI, MAI, FAI, and a pre-alloyed mixture of PbI_2 and $PbBr_2$ (schematics in

Figure 4.3a). As-prepared films were analyzed by SEM (Figure 4.1a), showing randomly oriented grains with typical size in the 100 nm range, as frequently observed for vacuum-deposited perovskites. The XRD characterization of the as-deposited triple-cation perovskite thin film is shown in Figure 4.1b. The signal can be fitted considering a single cubic perovskite phase (space group Pm-3m, more details in the end of the section) with a lattice parameter of 6.22 Å, with only a small contribution of PbI_2 as well as the underlying ITO substrate. The lattice parameter is smaller than that of pure-iodide hybrid organic-inorganic cubic perovskites such as $FA_{1-x}MA_xPbI_3$ due to the incorporation of the smaller anion Br^- and cation Cs^+.[159] Moreover, the film shows a slight preferential crystalline orientation perpendicular to the (100) plane, though reflections for other directions are not completely suppressed.

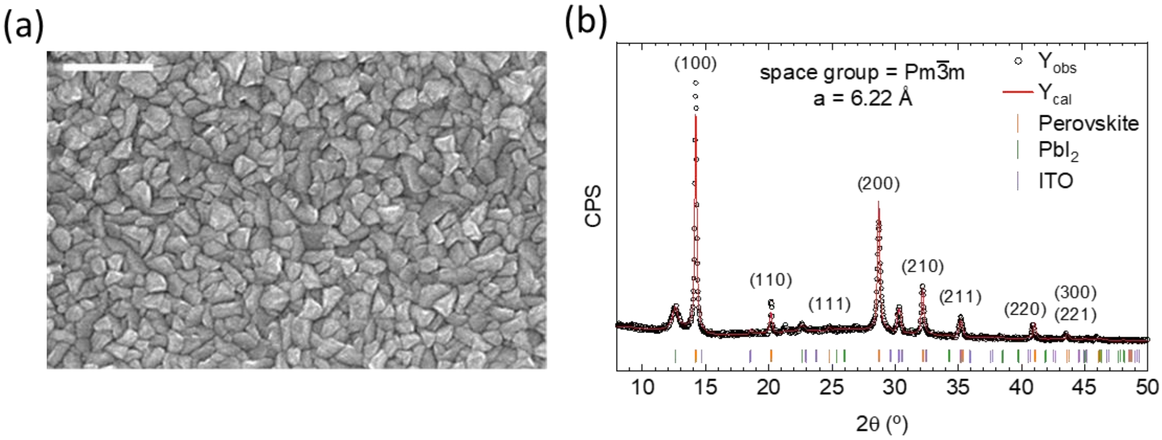

Figure 4.1. (a) SEM picture of the surface of an as-prepared CsMAFA triple-cation perovskite. Scale bar is 500 nm. (b) XRD characterization of as-deposited triple-cation perovskite thin film on ITO-coated glass slides. Observed (experimental) intensities are marked with open circles, Le Bail fit is represented in red and Braggs' reflection for the three different phases are indicated with vertical markers of different colors. Diffraction planes for the perovskite phase are indicated, as well as the considered space group and lattice parameter.

The absorbance spectra of a 500 nm thick wide-band gap CsMAFA perovskite film is reported in Figure 4.2a, showing the expected perovskite absorption profile, with absorbance > 1 for wavelength below approximately 550 nm and E_g = 1.73 eV, as estimated from the corresponding Tauc plot (Figure 4.2b). The photoluminescence spectrum (Figure

4.2c), obtained upon illumination with a 515 nm laser at carrier concentration equal to 1 sun illumination, shows a maximum at 1.735 eV and no halide segregation in as-prepared films.

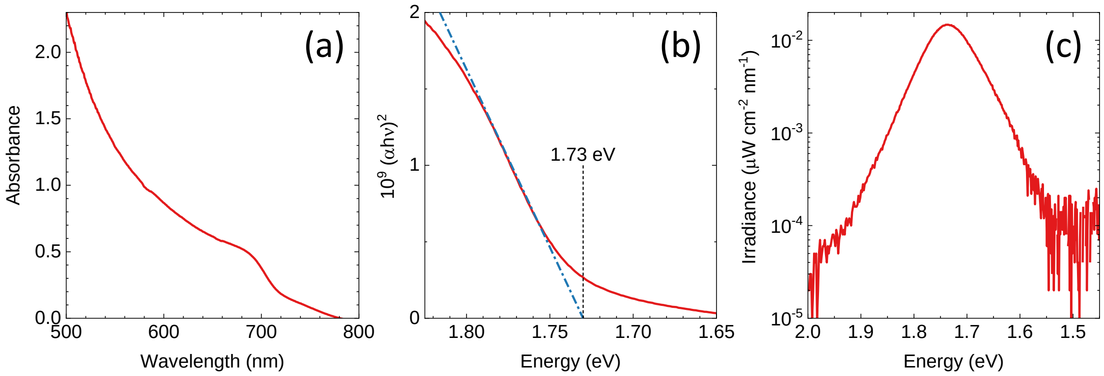

Figure 4.2. (a) Optical absorption spectra of a 500 nm thick film with corresponding (b) Tauc plot to estimate the bandgap. (c) Calibrated absolute photoluminescence spectra of the same film upon excitation with a 515 nm laser light source.

In view of the promising characteristics of the triple cation CsMAFA wide bandgap perovskite, we have used them to prepare thin-film solar cells in the p-i-n configuration (details of the device preparation are given in the Chapter 2). Briefly, patterned ITO transparent electrodes were coated with a thin layer (~ 5 nm) of PTAA as HTL. Afterwards, a 500 nm thick perovskite film was deposited on top and capped with an electron transport layer (ETL, C_{60}, 25 nm). A thin (8 nm) film of BCP was used to ensure ohmic contact in between the ETL and a silver electrode (100 nm thick).

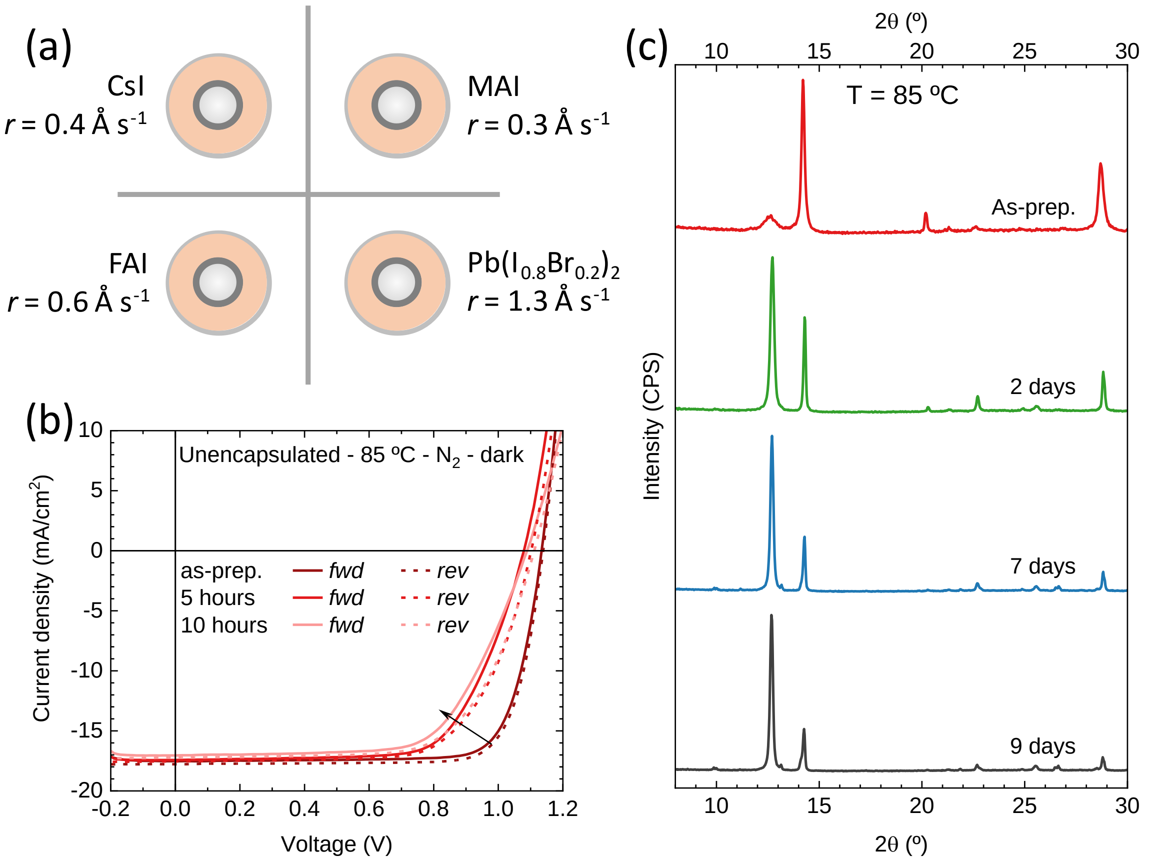

Figure 4.3. (a) Schematics of the deposition sources layout used in the vacuum processing of CsMAFA triple-cation perovskite films. Materials and corresponding deposition rates (r) are also reported. (b) J-V curves for a CsMAFA p-i-n solar cell taken at different times with the device kept at 85 °C on a hot plate in nitrogen atmosphere. The J-V curves are collected in forward (from short to open circuit, solid line) and reverse scan direction (from open to short circuit, dashed line). (c) XRD patterns for CsMAFA triple-cation perovskite films measured periodically ex situ during thermal stress.

The J-V curves under simulated solar illumination for a representative CsMAFA solar cell are reported in Figure 4.3b (statistics on the PV parameters in Figure 4.4a). The solar cells showed a high fill factor (80 % on average), indicating an efficient charge extraction of the photogenerated charge carriers. We also observed negligible hysteresis between the forward and reverse scans, which suggests that either ion migration or interface recombination (or both) are suppressed in these perovskite solar cells.[160,161] The average J_{sc} and V_{oc} were 17.4 mA cm^{-2} and 1157 mV, respectively, standing at the 80% of the theoretical maximum as described by the radiative limit for a semiconductor with a E_g = 1.73 eV.[162] The resulting average PCE was found to be 16.0%, with maximum values of 16.4%. We then evaluated the stability of the triple-cation CsMAFA perovskite devices via mpp tracking under illumination (Figure 4.4c).

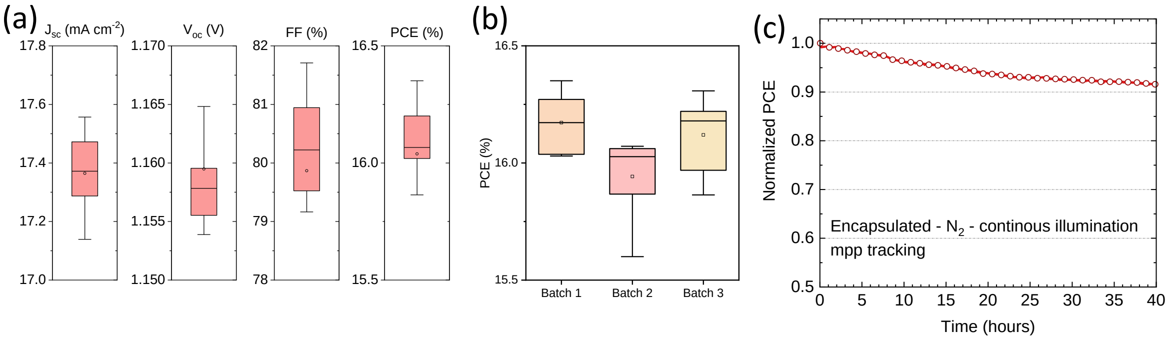

Figure 4.4. (a) Statistics of the photovoltaic parameters from 16 CsFAMA perovskite solar cells prepared in (b) 3 different batches. (c) Maximum power point tracking under simulated solar illumination for an encapsulated CsFAMA device, measured in inert atmosphere.

The devices were encapsulated with a UV-curable resin and a glass slide, and the stability was evaluated in a nitrogen atmosphere at RT to minimize the effect of environmental factors. Under these operational conditions the solar cell exhibited a limited stability, reaching 90% of the initial PCE after only 40 hours of continuous operation. We further tested the properties of the devices upon storing them in inert atmosphere at 85 ºC, and periodically measure their J-V characteristics (Figure 4.3b). The CsFAMA solar cells were also not stable under thermal stress, as in only 5 hours the V_{oc} and especially the FF were found to be strongly reduced (to approx. 1.1 V and 65%, respectively), a degradation which continued in the following time.

In order to shed light on the degradation mechanism leading to the fast loss of PCE of the CsMAFA triple-cation perovskite solar cells, we analyzed the XRD patterns of films under light and thermal stresses. In particular, different equivalent samples (from the same vacuum deposition run) were kept either under constant illumination (1 sun equivalent intensity) at 35 ºC (Figure 4.5) or on a hotplate at 85 ºC (Figure 4.3c) and periodically analyzed ex situ via XRD. Under light soaking (Figure 4.5) we observed a moderate rise in the PbI_2 signal (2θ = 12.7º) during the first 2 days, which then remains stable, suggesting that light-soaking under AM 1.5G alone is not a factor of degradation.

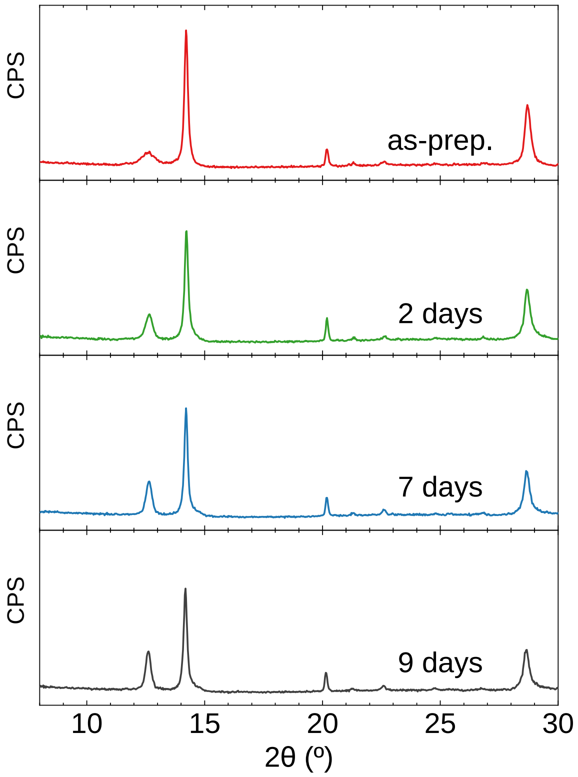

Figure 4.5. XRD patterns for CsMAFA triple-cation perovskite films measured periodically ex situ during light soaking at 1 sun equivalent intensity.

However, under constant thermal stress at 85 ºC (Figure 4.3c), the degradation into crystalline PbI_2 is accelerated, with its characteristic peak at $2\theta = 12.7^{o}$ becoming the most intense signal after only 2 days of thermal treatment and showing other new non-perovskite phases. These are ascribed to δ-$CsPbI_3$ and δ-$FAPbI_3$ yellow phases (Figure 4.6).[163] These findings indicate that the inclusion of bromide might hinder the high thermal stability of vacuum-deposited perovskites, which was otherwise demonstrated for pure-iodide formulation.[106,159,164–166]

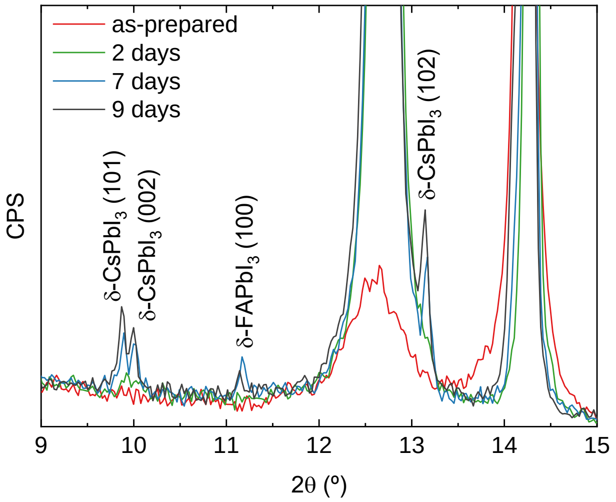

Figure 4.6. Low angle XRD patterns for CsMAFA triple-cation perovskite films upon ageing at 85 ºC, highlighting the formation of yellow phases.

To stabilize the perovskite composition, we added GAI as a forth A-site cation. FAI can be sublimed with a stable rate of 0.6 Å s^{-1} at an approximate temperature of 155-160 ºC, when pure GAI also sublimes (although with a slightly lower rate, r ~ 0.2 Å s^{-1}). As it has been previously shown, only a small amount of GA^+ is needed in order to structurally stabilize the perovskite without undermining the device functioning.[153,156,157] For this reason, we prepared a mixture of FAI:GAI with molar ratio 10:1 (see Experimental Section for details), and sublimed from the same crucible and at the same rate as for the triple-cation CsMAFA perovskites (schematics and summary in Figure 4.7a). The XRD characterization of the as-deposited quadruple-cation CsMAFAGA perovskite films is reported in Figure 4.7b. As with the triple-cation perovskite (Figure 4.1), we obtained a cubic perovskite with a similar lattice parameter of 6.22 Å. In principle, this suggests that guanidinium is not incorporated in large amounts within the crystal lattice (which would lead to a lattice expansion) in as-deposited films. Nevertheless, there are very marked effects on the material upon the addition of GAI, in particular the significant reduction of crystalline PbI_2 and a much more pronounced crystalline orientation of the perovskite film, with respect to the GA-free triple-cation perovskite films. The absorbance spectra of a 500 nm thick wide bandgap CsMAFAGA perovskite film is reported in Figure 4.7c, showing again the expected perovskite absorption profile, with absorbance > 1 for wavelength below approximately 550 nm and E_g = 1.72 eV, as estimated from the corresponding Tauc plot (Figure 4.7d). The photoluminescence spectrum (Figure 4.7e), obtained upon illumination with a 515 nm laser at carrier concentration equal to 1 sun illumination, shows a maximum at 1.727 eV and no halide segregation in as-prepared films.

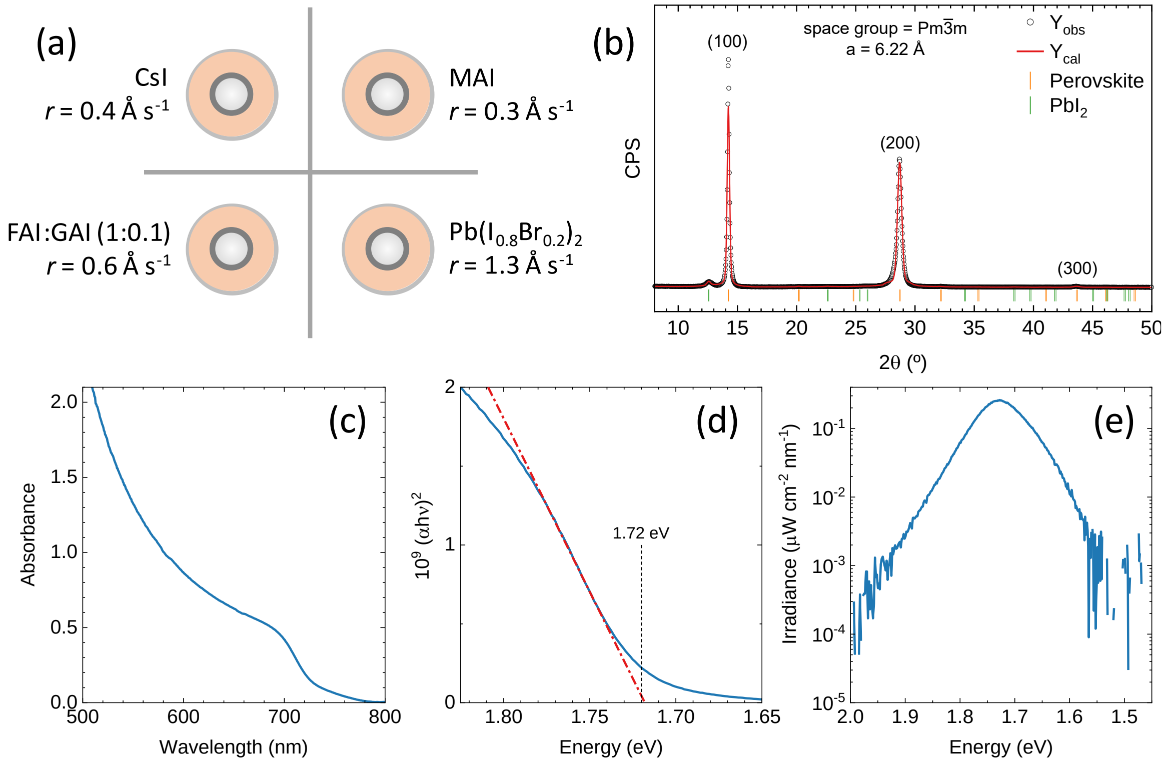

Figure 4.7. (a) Schematics of the deposition sources layout used in the vacuum processing of CsMAFAGA quadruple-cation perovskite films. Materials and corresponding deposition rates (*r*) are also reported. (b) XRD characterization of as-deposited quadruple-cation perovskite thin film on ITO. Observed (experimental) intensities are marked with open circles, Le Bail fit is represented in red and Braggs' reflection for the two different phases are indicated with vertical markers of different colors. Diffraction planes for the perovskite phase are indicated, as well as the considered space group and lattice parameter. (c) Optical absorption spectra of a 500 nm thick film with corresponding (d) Tauc plot to estimate the bandgap. (e) Calibrated absolute photoluminescence spectra of the same film upon excitation with a 515 nm laser light source.

In view of the low thermal stability of the triple-cation CsMAFA perovskite films, and in order to investigate the effect of the addition GA^+, we initially assessed the stability of quadruple-cation CsMAFAGA perovskite films, under light and thermal stresses. As described before, equivalent samples from the same vacuum deposition run were kept either under constant light soaking at 35 ºC (Figure 4.8a) or on a hotplate at 85 ºC (Figure 4.8b) and periodically analyzed ex situ via XRD. In both cases, the stability is remarkably improved with the addition of GAI. Note that the timespan in Figure 4.8 is 37 days, compared to the rapid degradation in only few days observed for the triple-cation perovskites. The XRD of the CsMAFAGA perovskite films do not show a marked increase in PbI_2 or other phases even after 5 weeks.

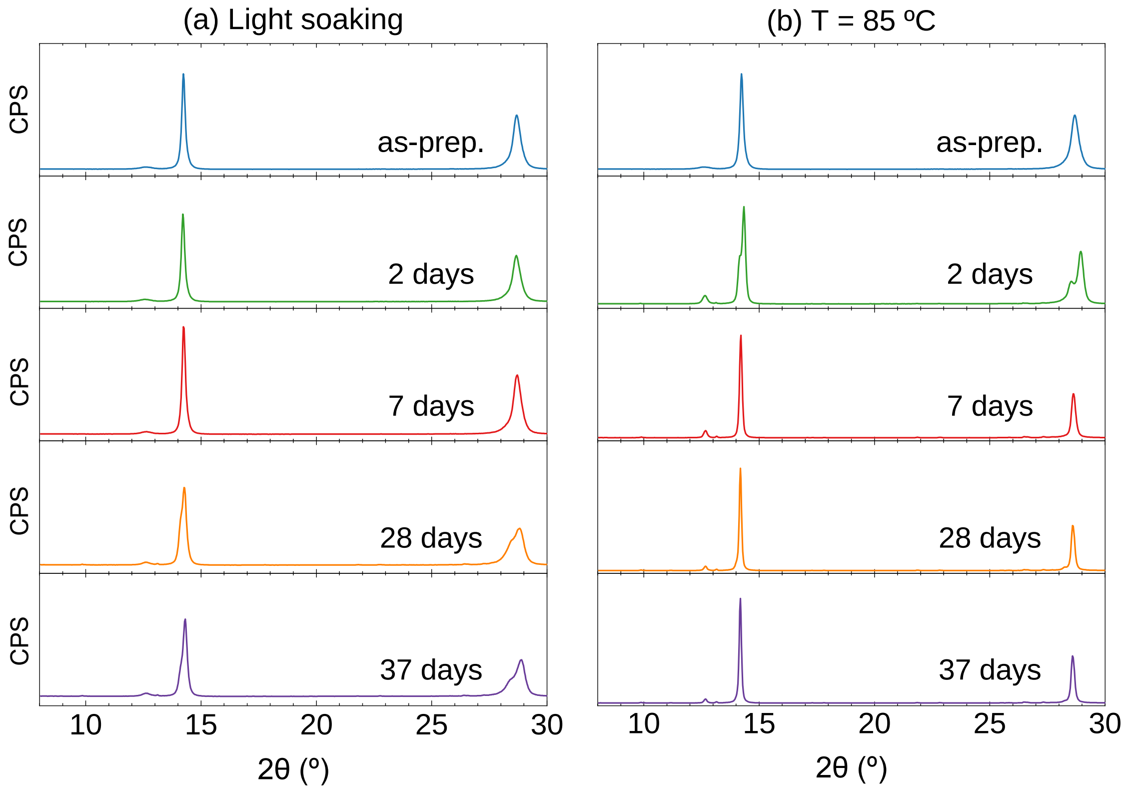

Figure 4.8. XRD patterns for quadruple-cation CsMAFAGA perovskite films measured periodically ex situ during (a) light soaking or (b) thermal stress.

Aside from this main observation, several additional transformations can be deduced from the XRD analysis. First, an apparent peak splitting occurs after 2 days at 85 ºC or 28 days under light soaking. It could be thought that such a peak splitting translates the coexistence of two phases. Nevertheless, the XRD signal can be fitted with a single lower-symmetry (orthorhombic) perovskite phase, isostructural to γ-$CsPbI_3$ (Figure 4.9a).[167]

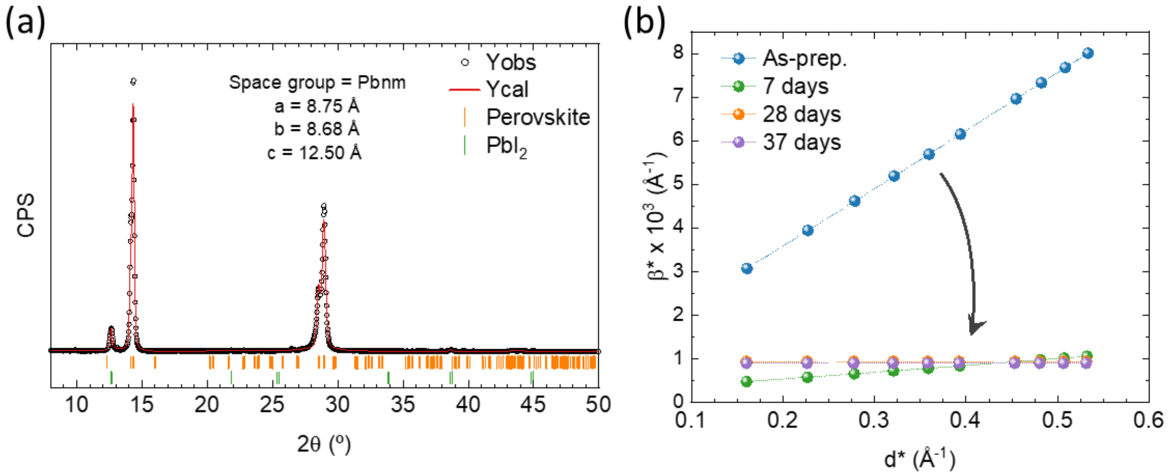

Figure 4.9. (a)Whole-pattern fit of quadruple-cation CsMAFAGA perovskite thin film after 2 days at 85 ºC. A single orthorhombic perovskite phase is considered in addition to PbI_2. (b) Williamson-Hall plots (inverse integral breadth versus inverse interatomic distance) for quadruple-cation films upon thermal stress. The most noticeable effect is a suppression of microstrain, related to the slope of the graph. Average crystallite size (inverse of extrapolated value at d* = 0) does not change significantly and remain around 100 nm.

In any case, this phase transition (or phase segregation) appears to be a transitional stage, as the diffractogram after one week at 85 ºC corresponds again to a single cubic perovskite phase. Interestingly, this new cubic perovskite phase (space group Pm-3m) has a larger lattice parameter a = 6.23 Å, which can be qualitatively observed by the shift to lower diffraction angles of the main perovskite peaks. The reason for the cubic lattice expansion between the pristine sample and the annealed sample is not fully elucidated (all measurements are carried out at room temperature) but could be due to the partial incorporation of guanidinium in the crystal lattice triggered by thermal stress. Furthermore, we observe a clear peak sharpening between pristine and annealed samples. A detailed microstructural analysis (Figure 4.9b) based on the whole-pattern Le Bail fit of the XRD signal and considering instrument resolution reveals that this peak sharpening is not strongly related to crystallite growth (note that crystallites are not identical to "grains" or domains observed by SEM),[168] but rather to a release in microstrain. This, linked to the previous observation, suggests that the GA^+ cations are not incorporated in the crystal lattice of the as-deposited films but rather are located at the grain boundaries. We deduce this as initially, the CsMAFAGA quadruple-cation perovskite has the same lattice constant as the CsMAFA triple-cation perovskite. This implies that the GA$^+$ cations are acting as structural defects (e.g., at grain boundaries), which induces microstrain.

As the films are thermally stressed, the GA$^+$ cations might be incorporated to some extent within the crystal, leading first to a transition to a lower-symmetry perovskite phase and ultimately to the stabilization of a cubic phase with larger unit cell volume and released microstrain. It must be noted that the use of multi-cation perovskites has already shown to play an important role in such a strain release.[169,170] Finally, we also observed a minor but persistent contribution from δ-CsPbI$_3$ and δ-FAPbI$_3$ after one week of thermal stress (Figure 4.10). The presence of these yellow phases, which remains marginal even after 5 weeks, seems not to be detrimental for the perovskite film stability, and could also partly contribute to the its stabilization by suppressing ion migration, as recently demonstrated by others.[171]

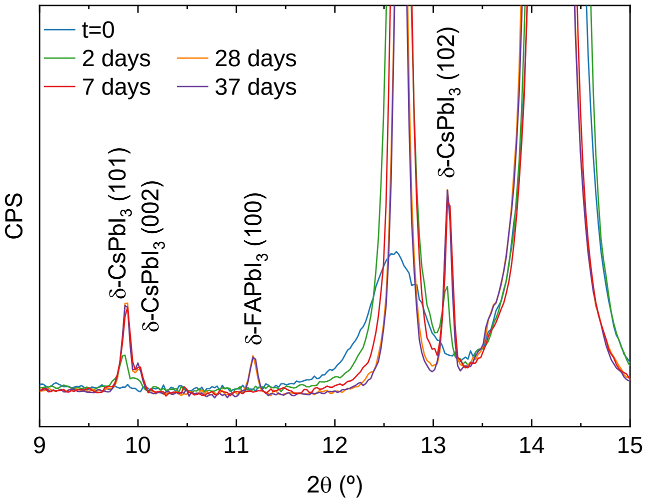

Figure 4.10. Low angle XRD patterns for quadruple-cation CsMAFAGA films upon ageing at 85 °C, highlighting the formation of yellow phases.

The quadruple-cation CsMAFAGA wide bandgap perovskite films were incorporated in thin-film solar cells with the same p-i-n configuration as described for the triple cation perovskites in the previous section. The J-V curves (forward and reverse bias) under simulated solar illumination for a representative CsMAFAGA solar cell, are reported in Figure 4.11a (statistics on the PV parameters is reported in Table 4.1). The solar cells showed a FF > 80 % indicating efficient charge extraction of the photogenerated charge carriers, similar to the above-described triple-cation perovskite solar cells. We again observed negligible hysteresis in between the forward and reverse scans, and measured J_{sc} and V_{oc} of 17.3 mA cm^{-2} and 1148 mV, respectively, essentially unaltered as compared to the triple-cation perovskite devices, indicating that the addition of GAI does not undermine (nor improve) the device functioning. The solar cells were encapsulated and the stability was initially evaluated in a nitrogen atmosphere at RT to minimize the effect of environmental factors on the degradation. The mpp tracking of the CsMAFAGA solar cells exhibited a remarkably enhanced stability, with the PCE being unaltered after 40 hours of continuous operation (Figure 4.11b).

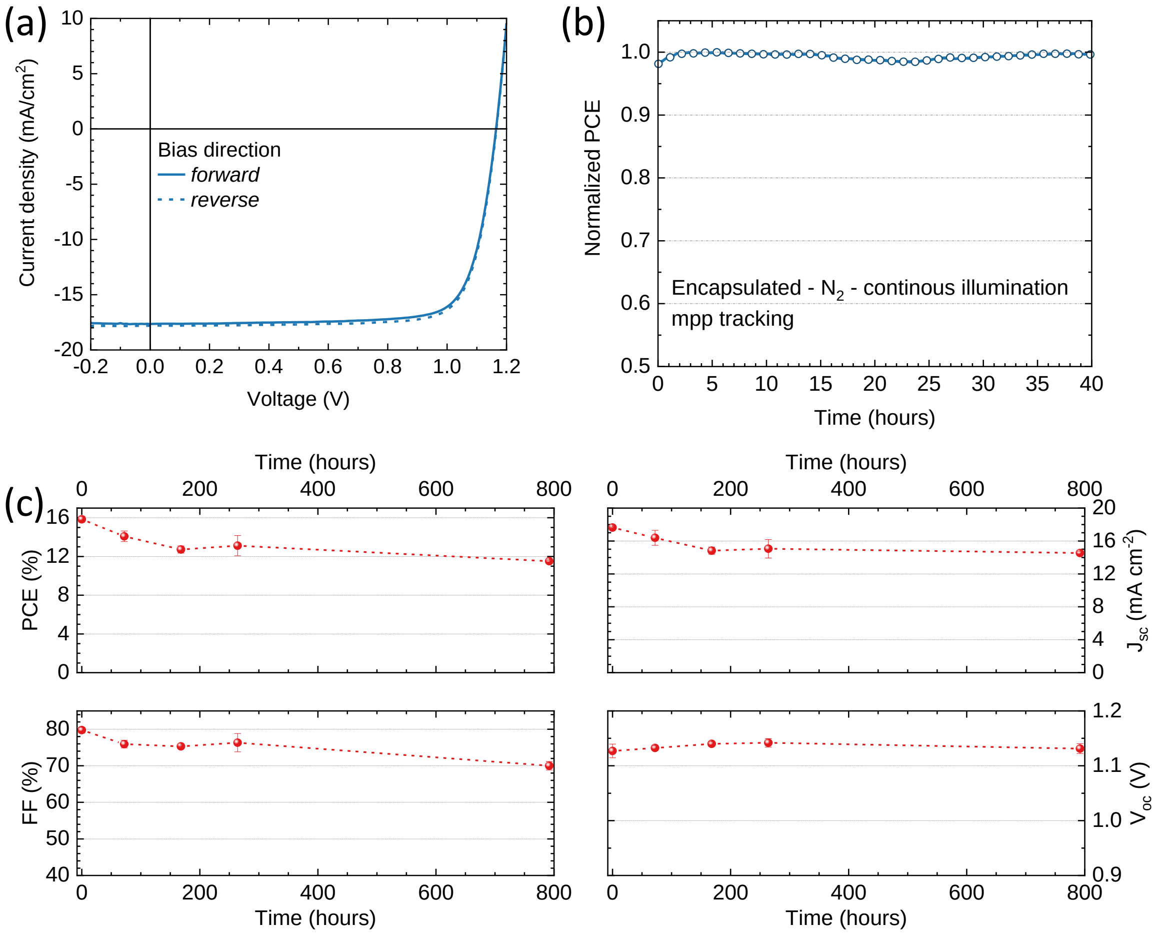

Figure 4.11. (a) J-V curves under illumination for a representative solar cells using a quadruple-cation CsMAFAGA perovskite as the absorber layer. The J-V curves are collected in forward (from short to open circuit, solid line) and reverse scan direction (from open to short circuit, dashed line). (b) Maximum power point tracking under simulated solar illumination for an encapsulated CsMAFAGA device, measured in inert atmosphere. (c) Shelf life thermal stability test for a similar solar cell: PV parameters extracted from J-V curves taken at different times for a device kept at 85 °C on a hot plate in nitrogen atmosphere.

Table 4.1. Average PV parameters extracted from the J-V characterization of quadruple-cation solar cells under simulated solar illumination.

Bias direction	**V_{oc} (V)**	**J_{sc} (mA cm^{-2})**	**FF (%)**	**PCE (%)**
Forward	1.148 ± 0.010	17.3 ± 0.2	82.4 ± 1.1	16.4 ± 0.2
Reverse	1.148 ± 0.070	17.3 ± 0.2	81.3 ± 1.5	16.1 ± 0.4

We further tested the stability of the devices by storing them at open circuit in an inert N_2 atmosphere at 85 ºC and periodically measuring their J-V characteristics under simulated 1 sun solar light at room temperature. Independently of the initial performance, we observed an increase in the FF of the solar cells (up to approximately 80%), and a small decrease of the V_{oc} (of about 20-25 mV). This does not change the initial efficiency for a well working device, but results in a net performance improvement for faulty pixels, which are found to be working correctly after annealing at 85 °C for 1 hour (Figure 4.12). The quadruple-cation CsMAFAGA solar cells were found to be very stable under thermal stress as compared to the triple-cation analogues (Figure 4.11c). The PCE dropped to about 80% of the initial value after 1 week of testing, and was found to be still above 75% of the initial PCE after 700 hours (roughly 1 month) of continuous thermal stress at 85 ºC, in analogy with the structural stability observed and describe in Figure 4.8. The PCE loss under thermal stress was mainly caused by small reductions in the J_{sc} and FF , while the V_{oc} was stable throughout the first month of test (Figure 4.11c).

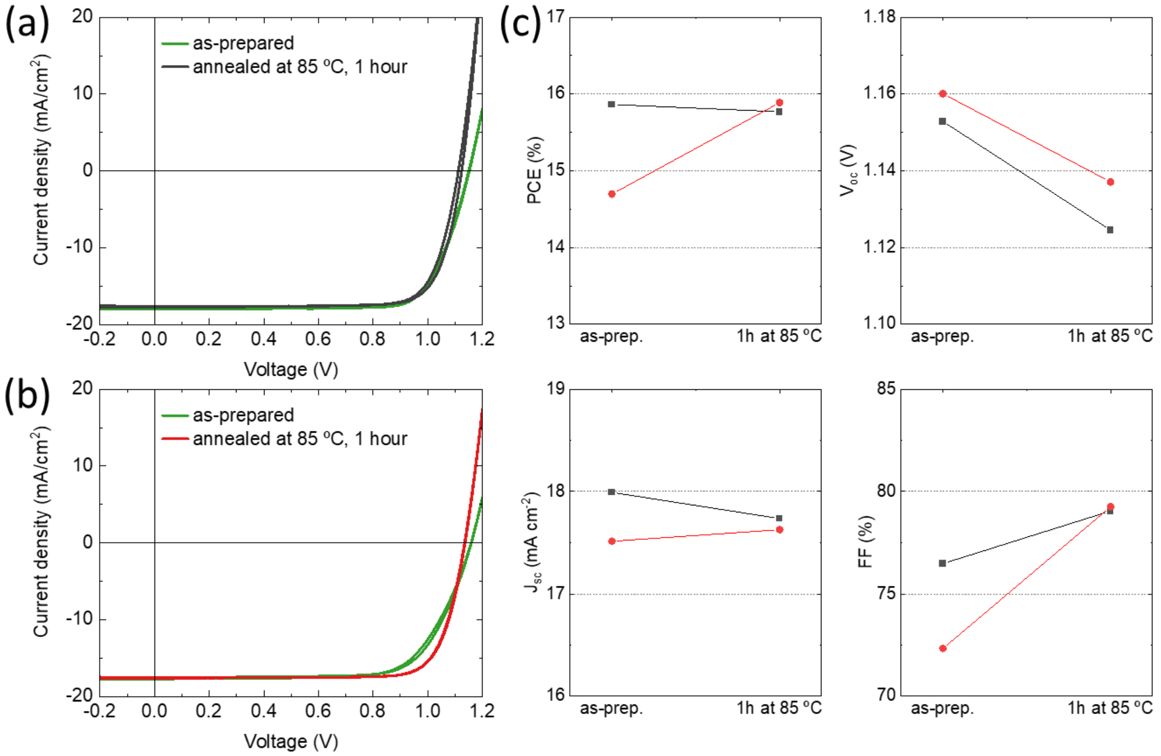

Figure 4.12. J-V curves under illumination for quadruple cation CsMAFAGA perovskite solar cell, as-prepared and after annealing at 85 °C for 1 hour. The curves correspond in particular to (a) a well-working device and (b) for a faulty pixel. After annealing, the (c) PV parameters are essentially unvaried for the well working device, while they are found to be substantially improved for the initially faulty solar cells.

4.4 Conclusions

In summary, we present a strategy to increase the complexity of the formulation of vacuum-deposited lead halide perovskites films by multi-source deposition and pre-mixing both inorganic and organic components. We applied this method to the preparation of wide bandgap CsMAFA triple-cation perovskite solar cells, which were found to be efficient but not stable, in particular when stressed at 85 °C. In an attempt to improve the stability, we added another A-site cation, GA^+, to the perovskite formulation. The resulting CsMAFAGA quadruple-cation perovskite films showed much improved thermal stability, with no sign of material degradation (not even by XRD) even after more than a month at 85 °C. Microstructural analysis suggests that GA^+ is initially not incorporated in the crystal structure, but it rather accumulates at the grain boundaries. However, during thermal stressing, a transition to a lower-symmetry perovskite phase and ultimately a stabilization of the cubic phase with larger unit cell volume is observed, indicating the incorporation of some GA^+ into the crystal (Figure 4.14). When used in solar cells, the wide bandgap CsMAFAGA quadruple-cation perovskite showed similar performance but enhanced thermal stability (as compared to the triple-cation perovskite), comparable to what is observed for bromide-free vacuum deposited perovskites. Future work will focus on a variety of different strategies, for example halide alloying,[35] the use different large ammonium cations,[172] and/or the study of MA-free formulations,[83,173] which have the potential to further enhance the thermal stability of the perovskite.

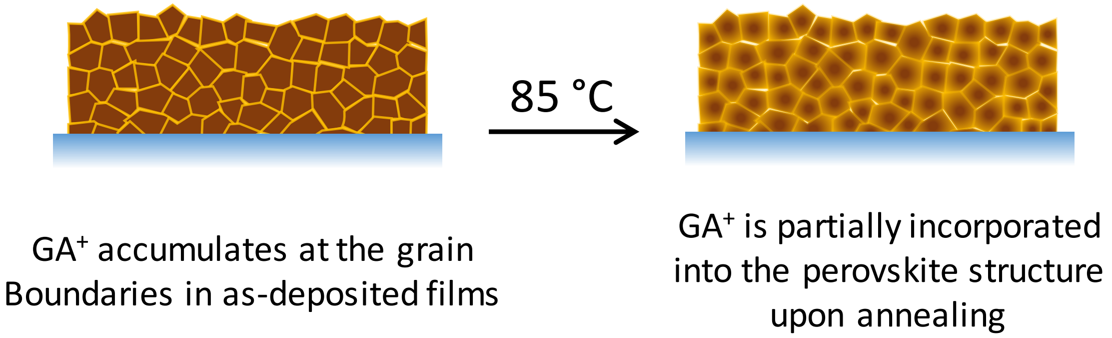

Figure 4.13. Schematics of GA^+ dynamic incorporation in vacuum-deposited, quadruple cation CsMAFAGA perovskite films. GA^+ initially accumulates at the grain boundaries, but upon annealing is progressively incorporated into the perovskite structure, stabilizing the material and preventing degradation.

Chapter 5

Pure iodide multi-cation wide bandgap perovskites by vacuum deposition

The $CsPbI_3$ perovskite has a suitable bandgap (≈1.7 eV) for application in tandem solar cells. One challenge for this compound is that the semiconducting perovskite phase is not stable at room temperature, when it tends to form a yellow non-perovskite phase with a bandgap of approximately 2.8 eV. Therefore, many reports have been focused on the stabilization of the $CsPbI_3$ black perovskite phase through the use of additives during solution processing. Vacuum deposited $CsPbI_3$ has been seldom reported, as in this case the insertion of stabilizing agents is more challenging. In this work, we demonstrate the vacuum processing of $CsPbI_3$ perovskite films at room temperature, obtained by incorporating dimethylammonium by co-sublimation with CsI and PbI_2. As-prepared films were applied in planar solar cells, leading to an average power conversion efficiency (PCE) exceeding 12%. In order to improve the device performances, we introduced a third A-site cation (methylammonium) in a four-source deposition process. This pure iodide formulation can be used in wide bandgap solar cells with a PCE up to 15%.

5.1 Introduction

Compared to hybrid mixed halide perovskites, pure inorganic perovskites such as $CsPbI_3$, with a bandgap of approximately 1.7 eV, are chemically simpler alternatives. However, in ambient conditions and at RT, $CsPbI_3$ transitions to a yellow non-perovskite phase with $E_g \approx 2.8$ eV, that is no longer interesting for PV applications.[174] Therefore many efforts have been focused on the stabilization of the $CsPbI_3$ black perovskite phase by adjusting the tolerance factor via substitution/addition of larger A-site cations and/or smaller B- or X-site species[51] (details in section 1.4). Dimethylammonium (DMA^+), with an ionic radius of 272 pm, has been successfully applied in the stabilization of the black perovskite phase of $CsPbI_3$.[175],[176],[48] It is worth noting that the stabilization of $CsPbI_3$ using the intermediate known as hydrogen lead iodide ($HPbI_3$), produced by adding HI in the solution, actually works via the formation of DMAI from the decomposition of dimethylformamide with HI, leading to a stable mixed A-cation $Cs_{1-x}DMA_xPbI_3$ phase.[177] There have been opposing reports of whether DMA is alloyed into the A-site or if it has a role of an additive in a crystallization process. Wang *et al.* demonstrate that the role of DMAI is a crystal growth additive achieving a record PCE of 18.4%, and up to 19.0% with additional phenyltrimethylammonium chloride passivation.[178] Marshall *et al.* revealed that DMA can be successfully incorporated into the $CsPbI_3$ perovskite to form an alloyed composition of $Cs_xDMA_{1-x}PbI_3$, which is more stable under atmospheric conditions than the original $CsPbI_3$.[175] The majority of these reports are based on solution-processing techniques (mainly spin coating), while vacuum deposition methods to prepare such stabilized $CsPbX_3$ compositions have been scarcely investigated. Huang *et al.* showed that an atmosphere controlled annealing process of vacuum deposited $CsPbI_3$ perovskite film results in high PCE up to 16%.[69] Nevertheless, the high temperature (350 ºC) needed for the fabrication limits the application of this method. Recently, Zang *et al.* demonstrated stable and efficient thermal evaporated γ-$CsPbI_3$ upon incorporation of phenetylammonium iodide (PEAI).[70],[179] The addition of PEAI during formation of the perovskite layer leads to preferred crystal orientation, improved microstructure and reduced density of defects. In this work, we demonstrate the vacuum processing of $CsPbI_3$ perovskite films at room temperature, obtained by incorporating DMAI by co-sublimation with CsI and PbI_2. As-prepared films were applied in planar solar cells, leading to an average PCE exceeding 12%. In order to improve the perovskite formulation and device performances, we introduced a third A-site cation (MA^+) in a four-source deposition process. This prompt the formation of homogenous films and efficient all-vacuum process wide bandgap solar cells with a PCE up to 15%.

5.2 Experimental section

Materials: TaTm and CsI were purchased from Tokyo Chemical Industry CO (TCI), Fullerene (C_{60}) was purchased from Merck KGaA. PbI_2, MAI, MoO_3, Spiro-TTB, TPBi, BCP were purchased from Luminescence Technology Corp. DMAI and FAI were purchased from Greatcell Solar. All materials were used as received.

Thin films and solar cells fabrication: Devices were made in both n-i-p and p-i-n configurations as described in the Chapter 2. Perovskite deposition was carried out in the vacuum chamber shown in Figure 2.2. All sources were individually calibrated for their respective materials and no cross-reading between the different QCMs is ensured by the relative position of the sources, shutters, sensors. For thickness calibration, we individually sublimed each material, and a calibration factor was obtained by comparing the thickness inferred from the QCM sensors with that measured with a mechanical profilometer (Ambios XP1). During the perovskite deposition, the pressure of the chamber was maintained at $8\cdot10^{-6}$ mbar and the substrates were kept at room temperature. Typical sublimation temperatures for the precursors were approximately 170 ºC for DMAI ($r = 0.2$ Å s^{-1}), 310 ºC for PbI_2 ($r = 1.2$ Å s^{-1}), 520 ºC for CsI ($r = 0.6$ Å s^{-1}), 100 ºC for MAI or FAI ($r = 0.1$ Å s^{-1}). All devices were encapsulated by ALD coating, as described in Chapter 2.

5.3 Results and discussion

The thin film deposition was carried out in a vacuum chamber equipped with 4 thermal sources, each with its own shutter and dedicated quartz crystal microbalance (QCM) thickness sensor. It is important to highlight that the perovskite layer was obtained at room temperature (RT), without additional step of annealing. Initially, we tested the simultaneous co-sublimation of CsI and PbI_2 (deposition rates r of 0.6 Å/s and 1.2 Å/s, respectively) from two geometrically opposite thermal sources with respect to the sample holder (Figure 5.1a), which was kept fixed during the deposition. This allows to create a compositional gradient and hence facilitate the direct observation of the eventual $CsPbI_3$ formation[180]. As clearly seen in Figure 1a, the substrates on the left side (closer to the CsI source) show a darker color, indicating the formation, to some extent, of $CsPbI_3$ in CsI-rich conditions. On the right, PbI_2-rich compositions do not lead to the formation of the perovskite phase, as the films appear yellow suggesting the formation of the δ-$CsPbI_3$ phase. This observation is expected and agrees with similar previous experiments carried out by Becker *et al.*, where the γ-$CsPbI_3$ perovskite phase was stabilized using CsI-rich formulations (and using a substrate temperature of 50 °C)[123]. In the attempt to obtain the γ-$CsPbI_3$ perovskite at RT, we co-sublimed also DMAI (r_{DMAI} = 0.3 Å/s) form a third sources placed in correspondence of the lower part of the sample holder, which is again fixed during the deposition. In the presence of DMAI, a dark $CsPbI_3$ phase is observed in the lower and central substrates (Figure 5.1b), extending also to the other surrounding substrates. As described in our previous work[180], the films composition in a deposition with substrate rotation resembles closely that of the central substrate when the sample holder is kept fixed. As the color of the central substrate in Figure 5.1b suggest the formation of the distorted γ-$CsPbI_3$ perovskite at RT, we prepared a series of films with different amount of DMAI, this time with rotating sample holder.

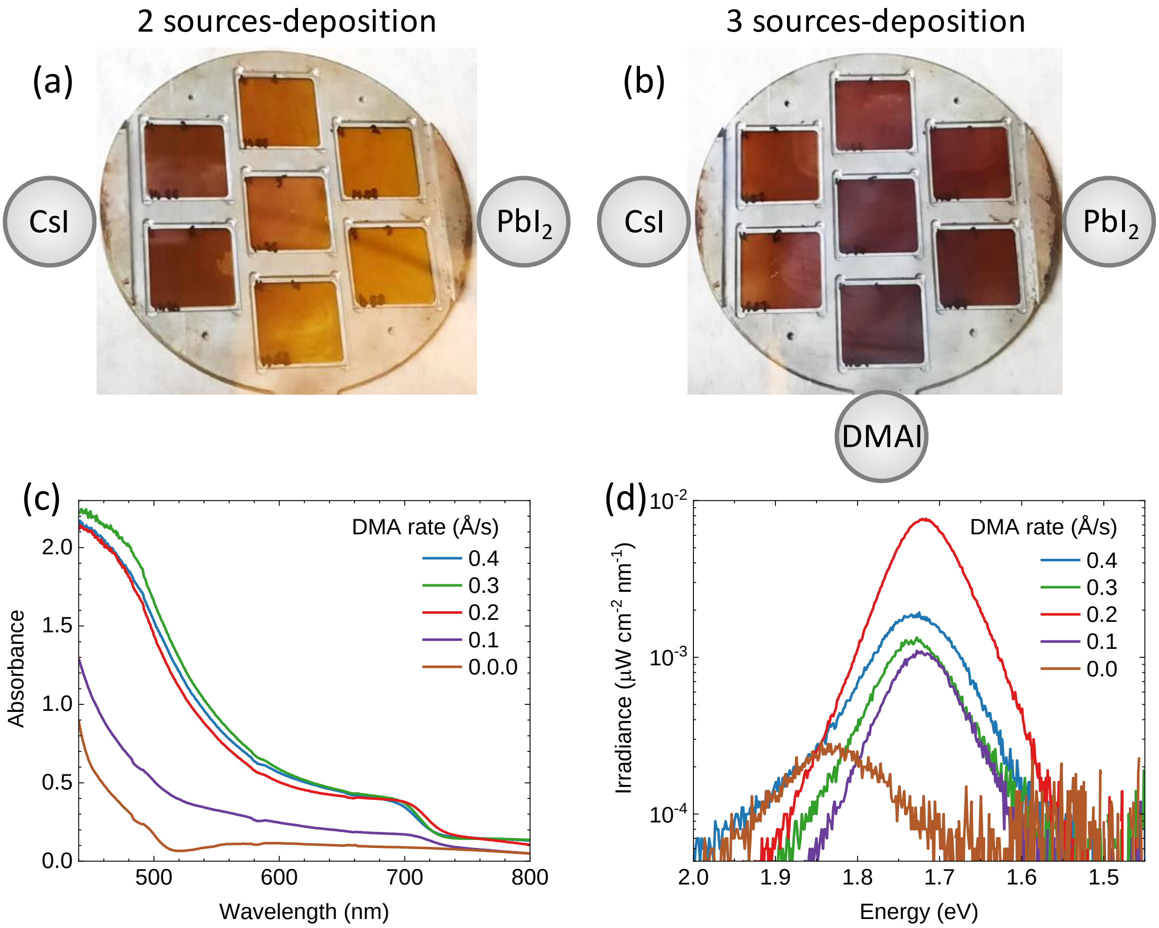

Figure 5.1. (a) Photograph of the sample holder with 7 as-deposited films after (a) 2-sources and (b) 3-sources vacuum deposition without sample rotation. The position of the thermal sources with respect to the sample holder and the corresponding materials are also reported. (c) Optical absorption and (d) photoluminescence spectra of a series of $CsDMAPbI_3$ perovskite films with varying DMA deposition rates, obtained with sample rotation.

The absorbance spectra of 250 nm thick perovskite films with increasing r_{DMAI} are reported in Figure 5.1c. In absence of DMAI, the perovskite is not formed, as indicated by the absorption profile which starts to raise only at approximately 520 nm (characteristic of the yellow δ-$CsPbI_3$ phase). With $r_{\mathrm{DMAI}} = 0.1$ Å/s, the absorbance is slightly increased and extends through the visible spectrum up to approximately 720 nm. For higher r_{DMAI}, as-deposited films show the expected perovskite absorption profile, with an absorption cutoff at 700-720 nm and a strong rise in absorbance for wavelengths below 600 nm. The photoluminescence (PL) spectra of the same films, collected upon illumination with a 515 nm laser using an intensity that leads to a carrier concentration equal to what would be obtained under 1 sun illumination, is reported in Figure 5.2d. The film without DMAI shows a very weak (note the semi-logarithmic scale) PL band centered at 1.83 eV maximum at 1.73 eV, which might be associated with the presence of small α-$CsPbI_3$ domains in the yellow δ-$CsPbI_3$ phase[181]. When DMAI is incorporated in the perovskite, the PL signal is enhanced and centered to 1.72 eV (720 nm), in agreement with previous reports on the mixed A-cation $Cs_nDMA_{1-n}PbI_3$ perovskite[177]. This indicates that the co-sublimation of DMAI with CsI and PbI_2 leads to the formation of a mixed A-cation perovskite, rather than solely stabilizing γ-$CsPbI_3$. The calibrated PL intensity (proportional to the PLQY) is observed to vary as a function of r_{DMAI}, with a maximum for r_{DMAI} = 0.2 Å/s. The X-ray diffraction of the as-deposited films (Figure 5.3) show a low signal-to-noise-ratio (SNR), suggesting low degree of crystallization and/or the presence of amorphous material. While the low SNR precludes a detailed discussion on the structural properties of the films, the mixed compound $Cs_nDMA_{1-n}PbI_3$ can be identified, together with a residual γ-$CsPbI_3$ phase.

In order to evaluate the potential of these materials, we used them in fully vacuum processed solar cells, prepared in both the p-i-n and n-i-p configurations (Figure 5.2a). Glass substrates with patterned indium tin oxide (ITO) were used for the device fabrication. The structure of p-i-n cells was: ITO/Spiro-TTB (5 nm)/Perovskite (250 nm)/C_{60} (25 nm)/BCP (8 nm)/Ag, where Spiro-TTB is 2,2′,7,7′- Tetrakis(N,N′-di-p-methylphenylamino)-9,9′-spirobifluorene, C_{60} is fullerene and BCP is bathocuproine. The inverted n-i-p cells had the structure: ITO/SnO_2 (20 nm)/C_{60} (10 nm)/Perovskite (250 nm)/TaTm (10 nm)/TPBi (2 nm)/MoO_3 (7 nm)/Au, where TaTm is N4,N4,N4″,N4″-tetra([1,1′- biphenyl]-4-yl)-[1,1′:4′,1″-terphenyl]-4,4″-diamine and TPBi is 2,2′,2"-(1,3,5-Benzinetriyl)-tris(1-phenyl-1-H-benzimidazole). SnO_2 was deposited by atomic layer deposition (ALD)[182], while MoO_3 was thermally evaporated in high vacuum. The fullerene layer was introduced in order to reduce carrier recombination at the SnO_2 electron transport layer, as previously observed for vacuum deposited n-i-p solar cells on titanium oxide[183],[184]. All devices were subsequently encapsulated with a 20 nm thick Al_2O_3 film deposited with a low temperature ALD process[165]. Details of the device fabrication are reported in the Experimental Section. Representative current-density versus voltage (J-V) curves (Figure 5.2b) under simulated solar illumination for p-i-n and n-i-p cells and statistics on the PV parameters (Figure 5.2c) for $CsDMAPbI_3$ with r_{DMA} = 0.2 Å/s, are reported in Figure 5.2. The J-V curves for p-i-n and n-i-p devices differs substantially. For p-i-n cells, we observed a kink in the J-V curve, resulting in an average fill factor (FF) of 48%, as well as hysteresis between J-V scans from short- to open circuit (forward, *fwd*) and open- to short circuit (reverse, *rev*). Both observations are likely related with interface and/or bulk charge recombination[185], which limits also the open-circuit voltage (V_{oc}) to 1.03 V, on average. In contrast, for n-i-p devices, we observed negligible hysteresis between forward and reverse scans, indicating that either ion migration or interface recombination (or both) are suppressed in this configuration.[160], [161] The V_{oc} in n-i-p cells is 1.12 V on average, with $FF > 70\%$ and short circuit current density (J_{sc}) of 15.3 mA/cm^2. Note that J_{sc} is higher for pin cells (16.4 mA/cm^2 on average), due to the absence for the highly absorbing C$_{60}$ film in the front part of the device. However, the resulting PCE for p-i-n cells was only slightly above 8%, while n-i-p cells delivered a promising average PCE of 12.1%. The reason for the superior performance of n-i-p solar cells is not yet clear, but it could be related with a higher diffusion length for holes as compared to electrons.

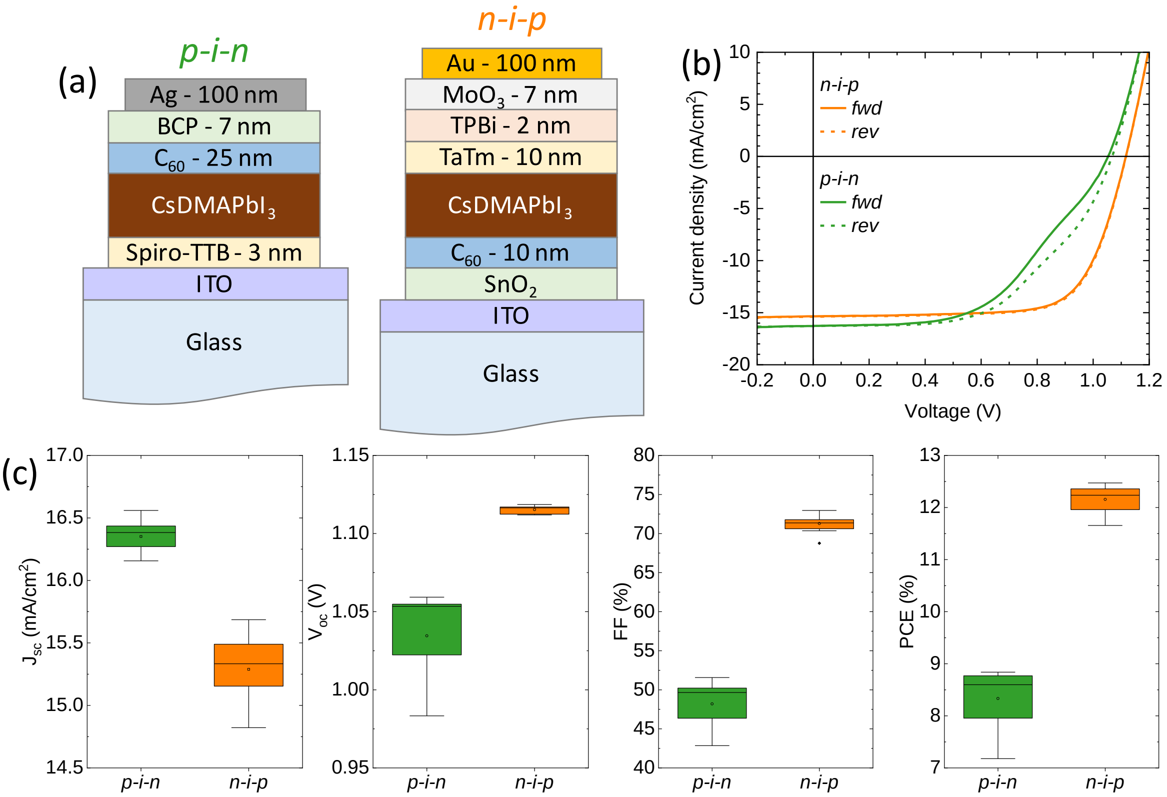

Figure 5.2. (a) Device layout for p-i-n and n-i-p cells used in this study. (b) Representative J−V curves for CsDMAPbI$_3$ solar cells, obtained with $r_{\mathrm{DMA}} = 0.2$ Å/s. The J−V curves are collected in forward (from short to open circuit, solid line) and reverse scan directions (from open to short circuit, dashed line). (c) PV parameters extracted from the same J-V curves.

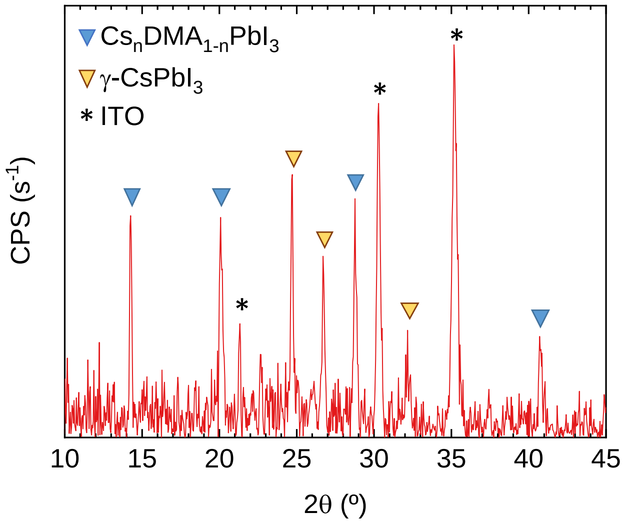

Figure 5.3. XRD pattern of a thin perovskite film deposited on ITO, obtained by co-sublimation of PbI_2 (1.2 Å/s), CsI (0.6 Å/s) and DMAI (0.2 Å/s). The main observable phases are assigned following literature reports.[177],[123]

With the aim to improove the optoelectronic properties of the $CsDMAPbI_3$ perovskite, we introduced a third A-cation, in particular MA^+ or FA^+. This led to a four-sources deposition process, subliming simultaneously CsI, PbI_2, DMAI, and MAI or FAI. As the intention is to introduce the A-cation as an additive, we kept its deposition rate low to 0.1 Å/s. The optical absorption of the triple-cation $CsMADMAPbI_3$ and $CsFADMAPbI_3$ films (Figure 5.4a) confirms the formation of perovskite in both cases, showing high absorbance below 600 nm and an absorption edge at approximately 700-720 nm and 720-740 nm when MAI and FAI is added, respectively. Perovskite films with incorporation of MAI exhibit a PL maximum (Figure 5.4b) at 1.73 eV (717 nm), whereas the perovskite films prepared with addition of FAI show the PL maximum at 1.70 eV (729 nm). From the above, the addition of MAI results in a slightly blue-shifted PL (wider bandgap) as compared to the reference $CsDMAPbI_3$ perovskite, while a narrower bandgap is observed upon addition of FAI. In a simplified view, this observation can be explained by the impact of the ionic radii of the additional cations: being smaller (217 pm), MA^+ would reduce the perovskite tolerance factor, slightly widening the bandgap, while FA^+ (253 pm) would have the opposite effect[186].

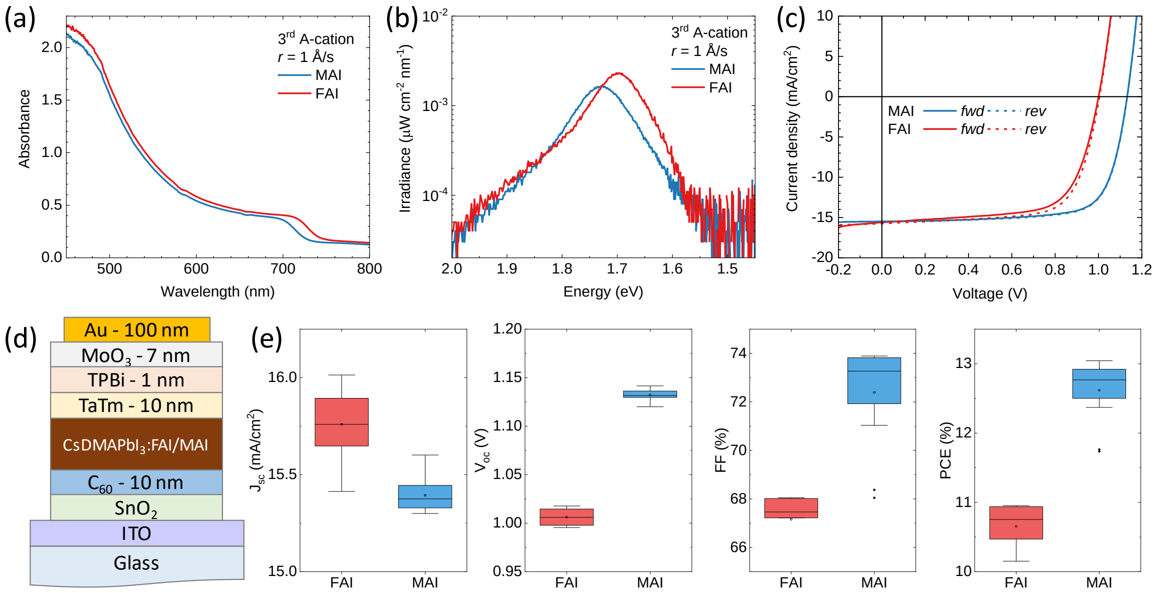

Figure 5.4. (a) Absorption and (b) PL spectra for triple cation perovskites obtained by adding MAI (blue) or FAI (red) to the previously developed $CsDMAPbI_3$ perovskite, using a fourth source and *r* = 0.1 Å/s. (a) J−V curves under illumination for a representative $MA\_DMACsPbI_3$ and $FA\_DMACsPbI_3$ solar cells and corresponding (b) PV parameters extracted from J-V curves.

The triple cation perovskite films were tested in n-i-p devices, with the structure reported in Figure 5.4d. The solar cells based on the perovskites obtained with FAI showed lower performance, reaching an average PCE of 10.7%. This is related with the low V_{oc} and FF (about 1 V and 67%, respectively). The solar cells prepared with $CsMADMAPbI_3$ results in slightly improved PCE, up to 13%, as compared to the $CsDMAPbI_3$ based devices showed in Figure 5.2, consequence of a small increase of the V_{oc} and FF (1.13 V and 73%, on average). The J_{sc} was found to be 15.4 mA/cm^2 on average, likely a consequence of the thin absorber layer used. From the EQE spectrum in Figure 5.5, one can notice a strong reduction of the EQE in the low energy region, which is a signature of insufficient thickness of the perovskite layer[29].

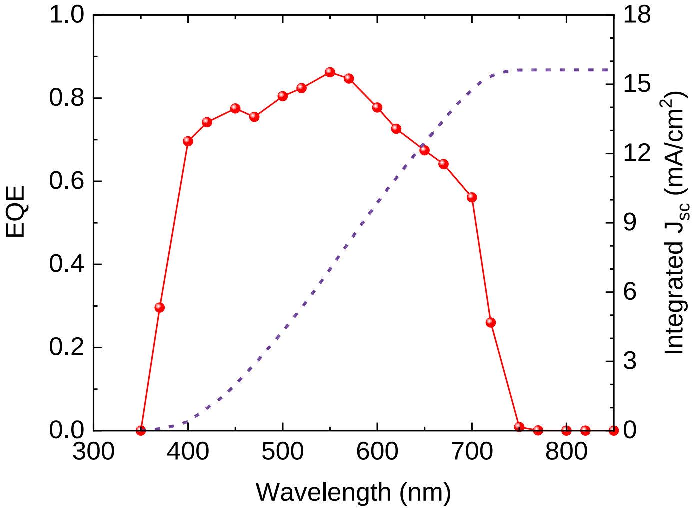

Figure 5.5. EQE spectrum (red) of a CsMADMAPbI$_3$ perovskite solar cell in the n-i-p configuration, with 250 nm thick perovskite, and corresponding integrated short-circuit current density with the AM1.5G solar irradiance spectrum.

Hence we fabricated solar cells with increased thickness of perovskite layer (400 nm), to try to compensate for the current density loss. The J-V curves of these devices (Figure 5.6a) did not show any appreciable hysteresis, resembling closely the ones with the thinner perovskite absorber (Figure 5.4c), but the current density was found to be increased to 17 mA/cm^2. This is a consequence of the enhanced spectral response in the red part of the visible spectrum. The V_{oc} and FF were almost unaltered (about 1.15 V and 74%), resulting in a very promising PCE of 14.4% on average and with record pixels close to 15%. This value is on par with the best reported, pure iodide wide bandgap perovskite solar cells[70] prepared by thermal evaporation.

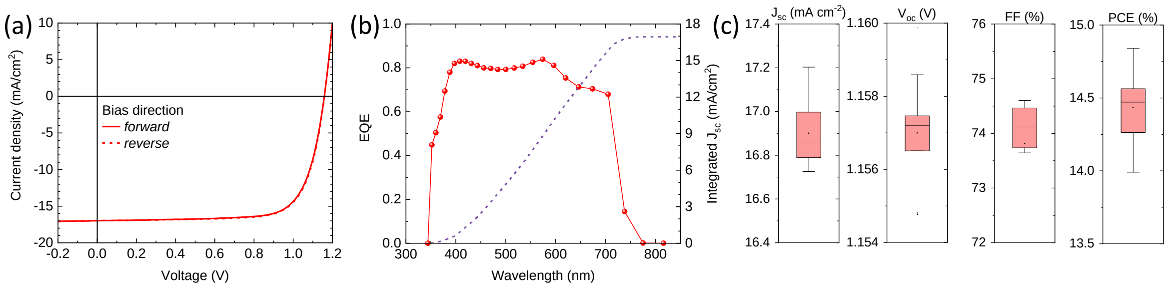

Figure 5.6. (a) J−V curves for a triple cation CsMADMAPbI$_3$ perovskite solar cell, with a 400 nm thick absorber layer. (b) EQE spectrum with integrated current density and (c) PV parameters extracted from J-V curves.

Among the major benefits of thermal evaporation is the wide substrate compatibility, for example allowing the deposition of perovskite films on both flat and textured surfaces. Here we show a conformal coating of the triple cation $CsMADMAPbI_3$ perovskite on top of textured silicon substrate with 3 - 5 μm pyramidal height. The cross-section SEM shows a conformal coating of the textured silicon with the $CsMADMAPbI_3$ perovskite (Figure 5.7a). Importantly, the perovskite film is uniform in terms of morphology and thickness, and appears very compact with low porosity. Therefore, this perovskite composition is also promising for perovskite/silicon tandem devices, where complete and conformal coverage is desired.

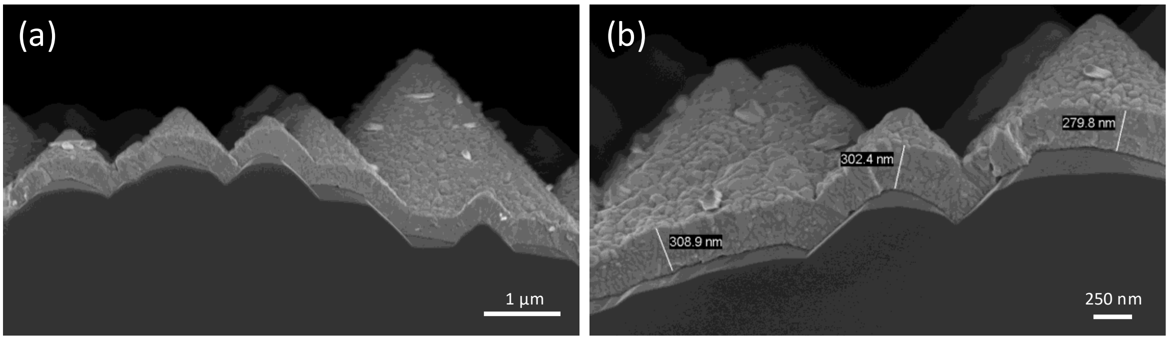

Figure 5.7. (a) Cross-sectional SEM of a $CsMADMAPbI_3$ perovskite film deposited on a textured silicon substrate. (b) Zoom of the same sample highlighting the uniform thickness and low porosity of the perovskite coating.

5.4 Conclusions

In summary, we investigated the vacuum deposition of pure iodide wide bandgap perovskites at room temperature. $CsPbI_3$ deposition at RT results predominantly in the formation of the yellow δ-phase, as previously reported. The black phase can be stabilized with the incorporation of a larger cation, DMAI, allowing the formation of a mixed $CsDMAPbI_3$ perovskite at RT. We have investigated the optoelectronic properties of this material in planar p-i-n and n-i-p solar cells, with the latter exhibiting superior performance, likely due to a non ambipolar charge transport in the material. We have further studied the use of a third A-site cation, adding formamidinium (FA^+) and methylammonium (MA^+) in a four-sources vacuum deposition process. The use of MAI resulted in more favorable optoelectronic properties, and by tuning the perovskite thickness, promising efficiency of up to 15% were obtained for pure iodide, wide bandgap perovskite solar cells completely prepared by vacuum/vapor deposition methods. This triple cation perovskite can be coated on top of the textured silicon used in Si solar cells, making the material and process promising for perovskite/silicon tandem solar cells.

Chapter 6

Conclusions

The aim of the thesis was to advance the development of vacuum deposited wide bandgap perovskite films, as well as to investigate their properties when incorporated in planar solar cells. The findings and insights acquired from this thesis will contribute to the advancement of perovskite photovoltaics, as improved material formulations were developed using deposition techniques that can be readily adopted by the industry.

In the third chapter, we performed combinatorial vacuum deposition of wide bandgap perovskites of the type $FA_{1-n}Cs_nPb(I_{1-x}Br_x)_3$, by using 4 sources and a non-rotating sample holder, producing >100 solar cells with distinct perovskite absorbers in a single deposition run. These materials were thoroughly analyzed using spatially resolved techniques such as optical, morphological, and structural analyses. Through precise adjustment of the deposition rates, we were able to modify the gradient and replicate the most efficient formulations in standard depositions with rotation. This approach shows great potential for the development of novel perovskite formulations overcoming the current limitations of vacuum deposition.

In the fourth chapter, we introduced the method that allows to increase the complexity of the formulation of vacuum-deposited perovskite films by multi-source deposition and pre-mixing both inorganic and organic components. We applied it to the preparation of wide bandgap triple-cation perovskite solar cells, which demonstrate high efficiency but low thermal stability. To address this issue and enhance the stability of the perovskite phase, we introduce guanidinium into the material formulation. As a result, we successfully obtained quadruple-cation perovskite films that exhibit improved thermal stability, as confirmed by X-ray diffraction and explained through microstructural analysis. The solar cells based on these films showed similar performance with enhanced thermal stability. This study opens up possibilities for the vacuum-based fabrication of complex perovskite compositions, which has significant implications not only in the field of photovoltaics but also in other optoelectronic applications.

In the fifth chapter, we stabilized the black perovskite phase of $CsPbI_3$ at room temperature by incorporation of a larger cation, DMAI. We have studied the optoelectronic properties of this material employing it in planar p-i-n and n-i-p solar cells. The n-i-p configuration exhibited superior performance, possibly attributed to the material's non-ambipolar charge transport. Additionally, we explored the incorporation of a third A-site cation, formamidinium, and methylammonium, using a four-sources vacuum deposition technique. The addition of MAI resulted in improved optoelectronic properties, and by fine-tuning the perovskite thickness, we achieved efficiency up to 15%, which is very promising for fully vacuum deposited and pure iodide wide bandgap perovskite solar cells.

Chapter 7

Resumen en Castellano

Capítulo 1: Introducción y objetivo de la tesis

1.1 Calentamiento global y energía fotovoltaica

En el último siglo, la población mundial ha aumentado de 2.000 millones a aproximadamente 8.000 millones, lo que ha ido acompañado de un incremento igualmente elevado de la demanda de energía. Hoy en día, las principales fuentes de energía son los combustibles fósiles, como el petróleo, el gas natural y el carbón, que son finitos y al quemarse liberan grandes cantidades de CO_2 en la atmósfera. El CO_2 es un gas de efecto invernadero, directamente responsable del calentamiento global. Por ello, es necesario un cambio en el modelo de generación de energía, incrementando el uso de fuentes de energía renovables, como la solar y la eólica, que son más limpias y sostenibles. A pesar de que el uso de fuentes de energía renovables haya aumentado considerablemente, siguen representando sólo un pequeño porcentaje (aproximadamente el 15%) de la generación mundial de energía. El reto consiste en seguir explorando y desarrollando nuevas tecnologías más eficientes, rentables y sostenibles, que contribuyan a reducir las emisiones de gases y el uso de recursos finitos. Entre todas las reservas renovables, la energía solar es la más abundante y accesible. Por ello, una de las más prometedoras tecnologías renovables es la fotovoltaica, que consiste en la conversión directa de energía solar en eléctrica. La tecnología fotovoltaica puede clasificarse en tres generaciones. El mercado fotovoltaico está actualmente dominado por las células solares de silicio, que constituyen la primera y más madura generación de células solares. Esta primera generación incluye el silicio monocristalino, policristalino y multicristalino, pero también semiconductores cristalinos III-V como el GaAs. La segunda generación consiste en capas de semiconductores de sólo unos micrómetros de grosor (por ello denominados de capa fina), y las tres principales tecnologías son el silicio amorfo, el telururo de cadmio (CdTe) y el sulfuro/seleniuro de cobre, indio y galio (CIGS). Actualmente, la investigación se centra en dispositivos de tercera generación basados en semiconductores no convencionales con el potencial de ser baratos y, al mismo tiempo, ofrecer una alta eficiencia energética. Los principales ejemplos son las células solares orgánicas (OSC), las células solares sensibilizadas por colorantes (DSSC), las células solares de perovskita (PSC) y las células solares de puntos cuánticos (QD). Las perovskitas son las más prometedoras debido a sus propiedades optoelectrónicas.

En la última década, las células solares de perovskita se han estudiado y desarrollado de manera muy rápida, alcanzando una eficiencia récord que supera el 25%.

1.2 Funcionamiento de las células solares

Una célula solar genera energía eléctrica produciendo una corriente y un voltaje cuando se expone a la luz. Los procesos generales en el funcionamiento de una célula solar son: absorción de fotones, generación y recombinación de portadores de carga, y su posterior transporte y recogida a los electrodos. La capa absorbente es un semiconductor que se define por su banda prohibida (E_g, "bandgap" por su nombre en inglés), una región de energía prohibida sin estados electrónicos intrínsecos. Cuando el semiconductor se expone a la luz, los fotones con energía $E_{ph} = h\nu$ mayor o igual que E_g serán absorbidos, dando lugar a la generación de pares electrón-hueco. Los fotones con $E_{ph} < E_g$ no son absorbidos, sino transmitidos o reflejados por el semiconductor. El exceso de energía ($h\nu - E_g$) de los fotones absorbidos se disipa en forma de calor en la estructura cristalina del semiconductor, mediante un proceso llamado termalización.

Tras la generación de pares electrón-hueco, los electrones y los huecos son extraídos selectivamente por los materiales de transporte de huecos y electrones, y recogidos en los electrodos. Sin embargo, el transporte y la recogida de carga compiten con los procesos de recombinación que se producen en el volumen o en las interfaces del material. Existen dos mecanismos principales de recombinación: la recombinación radiativa (con emisión de fotones) y la no radiativa (Shockley-Read-Hall).

El rendimiento de recolección de portadores de carga en las células solares puede cuantificarse mediante la eficiencia cuántica externa (EQE). El EQE es la relación entre el número de portadores de carga extraídos de la célula solar y el número de fotones incidentes con una energía determinada. Para una célula solar ideal, en la que se absorben todos los fotones de una determinada longitud de onda y se recogen todos los portadores resultantes, el espectro de EQE sería unitario y constante para $h\nu \geq E_g$. Sin embargo, en las células solares reales el EQE es siempre < 1 debido a varios mecanismos de pérdida, como la recombinación no radiativa y las pérdidas ópticas.

Cuando una célula solar está en la oscuridad se comporta como un simple diodo, conduciendo corriente sólo en polarización directa. La relación entre corriente y tensión en un diodo puede observarse en la curva de densidad de corriente frente a tensión (J-V) que se describe mediante la ecuación de Shockley. Cuando una célula solar se expone a la luz, se genera una fotocorriente (negativa) y la curva J-V se desplaza hacia valores negativos en el eje vertical. Para la caracterización de las células solares, la principal figura de mérito es la eficiencia de conversión de potencia (PCE), definida por los siguientes parámetros: corriente de cortocircuito (J_{sc}), voltaje de circuito abierto (V_{oc}) y factor de llenado (FF). Estos parámetros pueden extraerse de las curvas J-V características de una célula solar bajo iluminación.

En 1961, Shockley y Queisser propusieron un modelo para calcular la máxima eficiencia posible de un dispositivo fotovoltaico, conocido como límite de Shockley-Queisser o límite radiativo. En el límite radiativo, la eficiencia de una célula solar está limitada principalmente por la fracción de fotones absorbidos y por la termalización de los portadores de carga. Un método para superar esta limitación consiste en incluir múltiples capas semiconductoras con bandgap complementarios en la estructura del dispositivo, formando células solares multiunión. Las más comunes contienen dos semiconductores de diferente bandgap y se denominan células solares tipo tándem. Cada semiconductor tiene un bandgap diferente y absorbe una parte distinta del espectro solar, lo que permite minimizar las pérdidas por termalización y alcanzar PCE más elevados. Las perovskitas son candidatos prometedores para esta aplicación, debido a la facilidad con la cual puede modificarse el bandgap en la región de 1.2-3.0 eV. Pueden emplearse en combinación con Si, CIGS u otra perovskita para formar células solares de alta eficiencia.

1.3 Perovskitas

Las perovskitas, descubiertas por Gustav Rose en 1839, se refieren a la estructura cristalina del mineral $CaTiO_3$ y deben su nombre al mineralogista ruso Lev Perovski. La estructura de las perovskitas de haluro metálico, las que se están investigando para su uso en optoelectrónica y que se han estudiado en esta tesis, se describe mediante la fórmula general ABX_3, donde A es un catión monovalente inorgánico u orgánico, como Cs^+, metilamonio ($CH_3NH_3^+$) o formamidinio ($CH_3(NH_2)^{2+}$), B es un metal divalente (normalmente Pb^{2+}, Sn^{2+}, pero también Ge^{2+}) y X es un haluro (I^-, Br^-, Cl^-).

La estabilidad estructural de la perovskita puede estimarse considerando su factor de tolerancia geométrica, descrito por Victor Goldschmidt en 1926, que depende del tamaño de los átomos de la estructura. En el caso de las perovskitas de haluro, se obtienen compuestos estables para un factor de tolerancia entre 0.8 y 1. Un ejemplo es la perovskita más estudiada,

$MAPbI_3$, en el que el catión A es MA^+ y el del sitio B es Pb^{2+}, para la cual se han identificado tres fases, siendo la de estructura tetragonal la más estable a temperatura ambiente. La transición de la fase tetragonal a la cúbica se produce aproximadamente a 330 K (57 °C), mientras que, a bajas temperaturas, por debajo de 160 K, la fase estable es una estructura ortorrómbica.

Por otro lado, si sustituimos el MA^+ por un catión más pequeño como el Cs^+, el factor de tolerancia se vuelve demasiado bajo y la estructura cúbica pierde estabilidad. En el caso del $CsPbI_3$, la estructura más estable a temperatura ambiente es una fase ortorrómbica amarilla, que sufre una transición a la fase perovskita aproximadamente a 300 °C. Si se introduce un catión orgánico más grande, la estructura colapsa en un material 2D de baja dimensionalidad. Las perovskitas 2D consisten en láminas inorgánicas de haluro de plomo octaédrico separadas por capas dobles de cationes orgánicos ($n = 1$), mientras que las perovskitas cuasi-2D se obtienen cuando las capas inorgánicas están formada por n capas de haluro metálico octaédrico ($n = 2, 3,...$).

1.4 Propiedades físicas

Las perovskitas son semiconductores de bandgap directo que presentan muchas propiedades favorables para aplicaciones en optoelectrónica. Algunas de ellas son: alto coeficiente de absorción, baja energía de enlace de los excitones, posibilidad de modificar el bandgap mediante simples variaciones composicionales, buena movilidad de electrones y huecos y alta constante dieléctrica.

1.5 Perovskitas de bandgap ancho

Los semiconductores con bandgap > 1.6 eV son de gran interés para las células solares multiunión, y las perovskitas de haluro metálico son especialmente adecuadas para esta tarea. La forma más sencilla de obtener perovskitas de bandgap ancho es utilizar formulaciones mixtas de yoduro/bromuro, ya que el bandgap aumenta al sustituir el iodo con bromo. Sin embargo, al aumentar el contenido de bromuro, las perovskitas de haluro mixto pueden sufrir segregación de fase bajo iluminación, separándose en dominios ricos en I de bandgap más estrecho y dominios ricos en Br de bandgap más grande. Se han introducido varias estrategias para suprimir la segregación de haluros, como la ingeniería composicional, la formación de perovskitas 2D/3D y la modificación química de la interfaz.

1.6 Técnicas de deposición

Actualmente se emplean distintos métodos para formar capa de perovskitas, que pueden dividirse en dos categorías: técnicas de procesamiento en disolución y técnicas de deposición de vapor o en vacío. La deposición en vacío presenta varias ventajas en comparación con el procesamiento en disolución: procesamiento sin uso de disolventes, control preciso del grosor y la estequiometría de la capa, compatibilidad con la mayoría de sustratos y con procesado a larga escala sobre grandes superficies.

Las técnicas de deposición en vacío se clasifican en función de su complejidad: deposición de fuente única, deposición de doble fuente, deposición multi-fuente y evaporación secuencial.

1.7 Arquitectura del dispositivo

Las células solares de perovskita incluyen un electrodo transparente (normalmente un óxido conductor), una lámina de perovskita intercalada entre dos capas que permiten el transporte selectivo de electrones (ETL) y de huecos (HTL), y un contraelectrodo. Dependiendo de la posición de la capa de transporte con respeto al electrodo transparente del dispositivo, podemos distinguir dos estructuras: n-i-p, cuando la luz solar pasa primero por la capa de transporte de electrones, y p-i-n, cuando la luz entrante llega primero a la capa de transporte de huecos. En esta tesis se prepararon y estudiaron ambas arquitecturas, utilizando diferentes HTL y ETL.

1.8 Objetivos de la tesis

Para la aplicación en dispositivos tándem de alta eficiencia, es crucial desarrollar células solares eficientes con perovskita de bandgap ancho, fabricadas mediante técnicas escalables a la industria. Por lo tanto, el objetivo de esta tesis es desarrollar capas de perovskita de bandgap ancho con una formulación mejorada mediante sublimación, para luego incorporarlas en células solares.

La evaporación térmica de capas de perovskita con sistemas a nivel de laboratorio es un proceso lento, lo que conlleva un largo plazo de tiempo para optimizar incluso una única composición del material. En el Capítulo 3, se presenta un método para acelerar el desarrollo de nuevas composiciones de perovskita mediante evaporación combinatoria. Este método permite producir más de 100 células solares con diferentes composiciones de perovskita en una sola deposición.

La fabricación de perovskitas multi-componentes mediante sublimación tiene algunas limitaciones, entre las cuales que el número de precursores está limitado por el número de fuentes térmicas disponibles. En el capítulo 4 se presenta un método novedoso para aumentar la complejidad de la formulación de capas de perovskita depositadas por sublimación. Mediante la preparación previa de precursores mixtos, se demuestra la deposición de capas de perovskitas de cuádruple catión y doble anión, que tienen una estabilidad térmica muy elevada.

Se han llevado a cabo numerosas investigaciones para estabilizar la fase de perovskita del $CsPbI_3$ a temperatura ambiente, añadiendo otras componentes que aumentan el factor de tolerancia. En el Capítulo 5, se demuestra la fabricación por sublimación de capas de perovskita $CsPbI_3$ a temperatura ambiente mediante la incorporación del catión DMAI. Además, estas capas se incorporan en células solares totalmente procesadas en vacío, preparadas en las configuraciones p-i-n y n-i-p.

Capítulo 2: Técnicas experimentales y de caracterización

2.1 Fabricación de células solares de perovskita

La preparación de los dispositivos se llevó a cabo en una sala limpia de clase 10000, y todos los procesos de fabricación se realizaron en cajas secas de nitrógeno. El primer paso para la preparación de un dispositivo es la limpieza del sustrato. Después, los sustratos se transfieren a una cámara de vacío integrada en una caja seca, que se evacua a una presión de aproximadamente 10^{-6} mbar para depositar las capas de transporte.

En el capítulo 3, se empleó la estructura p-i-n: ITO/ MoO_3 (5 nm)/TaTm (10 nm)/perovskita/ C_{60} (10 nm)/BCP(8 nm)/Ag(100 nm). Todas las capas se fabricaron por sublimación. En el capítulo 4, se fabricó una configuración p-i-n utilizando una fina capa (~ 5 nm) de PTAA como HTL. En el capítulo 5 se prepararon e investigaron configuraciones p-i-n (ITO/Spiro-TTB/perovskita/ C_{60}/BCP/Ag) y n-i-p (ITO/SnO_2 (20 nm)/C_{60} (10 nm)/perovskita/TaTm (10 nm)/TPBi (2 nm)/MoO_3 (7 nm)/Au.

La deposición de la perovskita se llevó a cabo en una cámara de alto vacío integrada en una caja seca de atmósfera inerte, sublimando simultáneamente los precursores y formando la capa de perovskita. El espesor total de la capa de perovskita se controló mediante un sensor QCM colocado a la altura del soporte del sustrato. En esta tesis se obtuvieron e investigaron diferentes formulaciones de perovskita:

1. $FA_{1-n}Cs_nPb(I_{1-x}Br_x)_3$: deposición de vapor de cuatro fuentes utilizando FAI, PbI_2, $PbBr_2$ y CsI como precursores (Capítulo 3).
2. $CsMAFAGAPb(I_{1-x}Br_x)_3$: deposición de vapor de cuatro fuentes utilizando MAI, CsI, FAI:GAI y $Pb(I_{0.8}Br_{0.2})_2$ como precursores (Capítulo 4).
3. $CsMADMAPbI_3$: proceso de deposición de cuatro fuentes sublimando simultáneamente DMAI, PbI_2, CsI, MAI o FAI (Capítulo 5).

2.2 Técnicas de caracterización

Para determinar las propiedades de las capas de perovskita se emplearon varias técnicas de análisis. El grosor se midió con un perfilómetro mecánico, la morfología superficial se investigó mediante SEM, el análisis estructural se llevó a cabo con XRD, y la composición se estimó mediante EDAX. Para las propiedades ópticas de las capas se utilizó absorbancia y fotoluminiscencia.

Para determinar las características de las células solares se emplearon distintas técnicas de caracterización, como medidas de EQE y de curvas J-V. Las medidas de estabilidad de las células solares se llevaron a cabo utilizando un sistema de seguimiento del punto de máxima potencia (mppt).

Capítulo 3: Deposición combinatoria en vacío de capas y células solares de perovskita de bandgap ancho

3.1 Introducción

La deposición en vacío no es un proceso trivial en el caso de composiciones complejas de perovskita, dado que el número de fuentes térmicas limita el número de precursores que pueden co-sublimarse. Pero también hay otro factor, la deposición térmica en alto vacío (10^{-6} mbar) implica la sublimación simultánea de varios precursores con una velocidad de deposición global en el rango de 1-4 Å/s. Esto lleva a un tiempo de deposición de > 1 hora (normalmente 2 horas teniendo en cuenta la evacuación y ventilación de la cámara) para capas de perovskita con grosor de alrededor de 500 nm. Es importante destacar, además, que en un proceso de deposición sólo se puede utilizar un único conjunto de parámetros. Todos estos factores implican un largo período de tiempo para optimizar incluso una única composición de perovskita.

La ciencia combinatoria de materiales (CMS) es un método que puede utilizarse para acelerar el estudio de perovskitas de composición compleja. La CMS se utiliza ampliamente en la investigación y el desarrollo de catalizadores, biomateriales y nanomateriales. Cuando la CMS se aplica a capas finas, se deposita un gradiente con una variación de los parámetros de deposición, como la composición, el grosor o la temperatura, en un único sustrato de gran superficie, denominado biblioteca, formando un conjunto de materiales en una única deposición. A continuación, la biblioteca de materiales se investiga con técnicas resueltas en espacio, para identificar aquellas composiciones con las propiedades físicas o químicas más interesantes, que posteriormente pueden reproducirse como materiales homogéneos aislados. En la literatura existen algunos ejemplos simples de CMS de perovskita producidos por co-evaporación en vacío. Se han reportado gradientes composicionales utilizando dos fuentes térmicas con un sustrato fijo, dando lugar a gradientes lineales de dos precursores. El gradiente composicional formado durante la evaporación puede reproducirse sistemáticamente en otro proceso controlado.

En este capítulo se describe la deposición combinatoria en vacío de perovskitas de bandgap ancho del tipo $FA_{1-n}Cs_nPb(I_{1-x}Br_x)_3$, utilizando 4 fuentes y un portamuestras fijo. Con un conjunto inicial de velocidades de deposición para cada precursor, calculado en base a la estequiometría deseada de la perovskita, llevamos a cabo una deposición combinatoria y su caracterización. Mediante el uso de sustratos con píxeles pequeños, se pueden producir más de 100 células solares con diferentes composiciones de perovskita en una sola deposición. Los materiales se caracterizan minuciosamente mediante métodos resueltos en el espacio, para obtener propiedades ópticas, morfológicas y estructurales. Mediante el ajuste fino de las tasas de deposición, podemos posteriormente alterar el gradiente y reproducir las formulaciones de mejor rendimiento en deposiciones estándar con rotación. Consideramos que este enfoque puede acelerar el descubrimiento de materiales y servir de base para crear prototipos de otras composiciones (con bandgap estrecho, sin plomo), superando las limitaciones actuales de la deposición en vacío como herramienta de investigación para capas de perovskita.

3.2 Conclusión

Desarrollamos el proceso combinatorio de deposición en vacío de perovskita de haluro de plomo a partir de 4 precursores colocados en diferentes fuentes térmicas. Fijando el soporte de la muestra y analizando espacialmente el rendimiento de las células solares y las propiedades del material, podemos extraer una gran cantidad de información en una única deposición. Como sistema modelo, nos centramos en la perovskita de bandgap ancho del tipo $FA_{1-n}Cs_nPb(I_{1-x}Br_x)_3$, que puede procesarse en vacío a partir de FAI, CsI, PbI_2 y $PbBr_2$. Se han identificado varias propiedades de esta familia de materiales en un único proceso de deposición combinatoria, a diferencia de los experimentos estándar de deposición en vacío con portamuestras giratorio, en los que sólo puede estudiarse un conjunto de parámetros por cada lote. El gradiente de materiales obtenido mediante la deposición combinatoria puede modificarse ajustando los parámetros de deposición, y es posible reproducir las propiedades obtenidas en el sustrato central en una deposición con rotación, que es la que se utiliza habitualmente para la fabricación de células solares de perovskita. Esta característica puede acelerar el desarrollo de nuevas composiciones de perovskita: los experimentos combinatorios pueden llevarse a cabo con un soporte de sustrato fijo, las tasas de deposición pueden ajustarse desplazando los parámetros de los materiales deseados hacia el centro del soporte de la muestra y, finalmente, este conjunto de parámetros puede utilizarse en un proceso de deposición estándar con rotación de la muestra. Consideramos que esta ruta es la dirección a seguir para el futuro desarrollo de dispositivos optoelectrónicos procesados en vacío.

Capítulo 4: Células solares de perovskita de bandgap ancho con cuatro cationes y estabilidad térmica mejorada mediante deposición en vacío

4.1 Introducción

Una característica importante de las perovskitas es la posibilidad de ajustar con precisión su bandgap, lo que las hace adecuadas para células solares de una o varias uniones. Las composiciones de perovskita con bandgap ancho > 1.65 eV suelen emplear cationes mixtos para mejorar la fotoestabilidad y la estabilidad térmica de los compuestos. Aparte de las perovskitas de bandgap ancho de catión mixto y de haluro mixto del tipo $FA_{1-n}Cs_nPb(I_{1-x}Br_x)_3$ que se han preparado mediante deposición en vacío, Gil-Escrig *et al*. demostraron que las capas de perovskita de bandgap ancho $Cs_{0.5}FA_{0.4}MA_{0.1}Pb(I_{0.83}Br_{0.17})_3$ pueden prepararse en un proceso de co-sublimación de 4 fuentes, a partir de precursores PbI_2, CsBr, FAI y MAI, donde el CsBr se utilizó simultáneamente como fuente de Cs^+ y Br^-. Sin embargo, para aumentar el bandgap (E_g > 1.7 eV), se tuvo que incorporar una cantidad sustancial de Br^-, lo que dio lugar a una concentración de cesio igualmente grande. Recientemente, Igual-Muñoz *et al.* han demostrado la posibilidad de sublimar precursores de haluros metálicos mixtos a partir de una única fuente, mezclando previamente dos precursores mediante su fusión en atmósfera inerte a presión ambiente. Esta estrategia libera una fuente térmica que puede utilizarse para añadir otro componente en el proceso de deposición de la perovskita.

En este trabajo demostramos la deposición de capas de perovskita de triple catión CsMAFA a partir de 4 fuentes, sublimando simultáneamente CsI, MAI, FAI, y una mezcla de PbI_2 y $PbBr_2$. Este proceso resulta en capas de perovskita homogéneas que pueden incorporarse en células solares de perovskita de bandgap ancho eficientes. Sin embargo, las capas de perovskita y los dispositivos resultaron ser térmicamente inestables al someterlos a test térmicos a 85 °C. Por lo tanto, con el objetivo de estabilizar la estructura de la perovskita CsMAFA, añadimos un cuarto catión monovalente de tipo A, el guanidinio (GA^+). Se ha reportado que el GA^+ estabiliza tanto las perovskitas basadas en FA^+ como en MA^+, debido a la formación de un mayor número de enlaces de hidrógeno con una orientación favorable dentro de la estructura inorgánica. Además, el GA^+ puede incorporarse (hasta cierto punto) en una red de perovskita de haluro de plomo sin romper la estructura 3D, ya que su radio iónico (278 pm) es sólo ligeramente mayor que el del FA^+ (253 pm). Para añadir un componente más, aprovechamos las propiedades de sublimación similares del GAI y el FAI, y los sublimamos juntos desde una única fuente térmica. Esto se traduce en un proceso de deposición de 4 fuentes con 6 precursores, CsI, MAI, FAI, GAI, PbI_2 y $PbBr_2$, con FAI/GAI y PbI_2/$PbBr_2$ sublimados a partir de dos fuentes. Las capas preparadas resultaron ser muy estables al estrés térmico y a la iluminación, y las células solares correspondientes mostraron un PCE similar al de las homólogas de triple catión. Es importante destacar que las células solares muestran una alta estabilidad térmica, comparable a las mejores perovskitas de yoduro preparadas por deposición en vacío.

4.2 Conclusión

En resumen, presentamos una estrategia para aumentar la complejidad de la formulación de capas de perovskitas de haluro de plomo depositadas en vacío mediante la deposición multifuente y la mezcla de componentes inorgánicos y orgánicos. Aplicamos este método a la preparación de células solares de perovskita de triple catión CsMAFA de bandgap ancho, que resultaron ser eficientes, pero no estables, en particular cuando se sometían a temperaturas de 85 °C. En un intento de mejorar la estabilidad, añadimos otro catión, GA^+, en la formulación de la perovskita. Las capas de perovskita de cuádruple catión CsMAFAGA mostraron una estabilidad térmica mejorada, sin signos de degradación del material (ni siquiera por DRX) incluso después de más de un mes a 85 °C. El análisis microestructural sugiere que el GA^+ no se incorpora inicialmente a la estructura cristalina, sino que se acumula en los bordes de grano. Sin embargo, durante el estrés térmico, se observa una transición a una fase perovskita de menor simetría y, en última instancia, una estabilización de la fase cúbica con mayor volumen de celda unitaria, lo que indica la incorporación de GA^+ en el cristal. Cuando se utilizó en células solares, la perovskita de cuádruple catión CsMAFAGA de bandgap ancho mostró un rendimiento similar pero una mayor estabilidad térmica (en comparación con la perovskita de triple catión). El trabajo futuro se centrará en una variedad de estrategias diferentes, por ejemplo, la aleación de haluros, el uso de diferentes cationes de amonio, y/o el estudio de formulaciones sin MA, que tienen el potencial de mejorar aún más la estabilidad térmica de la perovskita.

Capítulo 5: Perovskitas multicationes de yoduro de bandgap ancho mediante deposición al vacío

5.1 Introducción

En comparación con las perovskitas híbridas de haluro mixto, las perovskitas puras inorgánicas como el $CsPbI_3$, con un bandgap de aproximadamente 1.7 eV, son alternativas químicamente más sencillas. Sin embargo, a temperatura ambiente, la fase estable del $CsPbI_3$ es una fase amarilla ortorrómbica con $E_g \approx 2.8$ eV, que no es interesante para aplicaciones fotovoltaicas. Por lo tanto, se han realizado muchos estudios para intentar estabilizar la fase negra de perovskita del $CsPbI_3$, principalmente ajustando el factor de tolerancia mediante la sustitución/adición de cationes de tipo A más grandes y/o con aniones más pequeños. El dimetilamonio (DMA^+), con un radio iónico de 272 pm, se ha aplicado con éxito en la estabilización de la fase negra de capas de $CsPbI_3$ procesadas por disolución. Existen experimentos contradictorios sobre si el DMA se incorpora en la perovskita o si tiene un rol de aditivo en el proceso de cristalización. Wang *et al*. demuestran que el rol del DMA^+ es el de un aditivo en el crecimiento cristalino, alcanzando un PCE récord del 18.4%, y de hasta el 19.0% con pasivación adicional de cloruro de feniltrimetilamonio. Marshall *et al*. revelaron que el DMA puede incorporarse con éxito a la perovskita $CsPbI_3$ para formar una composición mixta $Cs_xDMA_{1-x}PbI_3$, que es más estable en condiciones atmosféricas que el $CsPbI_3$ original. La mayoría de estos informes se basan en técnicas de procesamiento en solución, mientras que los métodos de deposición en vacío para preparar estas composiciones apenas se han investigado. Huang *et al*. demostraron por primera vez células solares de $CsPbI_3$ depositadas en vacío con un alto PCE de hasta el 16%. Sin embargo, la alta temperatura (350 °C) necesaria para la estabilización de la perovskita limita la aplicación de este método. Recientemente, Zang *et al*. han conseguido estabilizar capas evaporadas de γ-$CsPbI_3$ mediante la incorporación de yoduro de fenetilamonio (PEAI). La adición de PEAI durante la formación de la capa de perovskita conduce a una orientación preferente del cristal, una microestructura mejorada y una reducida densidad de defectos. En este trabajo, demostramos la deposición en vacío de capas de perovskita $CsPbI_3$ a temperatura ambiente, obtenidas mediante la incorporación de DMAI por co-sublimación con CsI y PbI_2. Las capas preparadas se emplearon en células solares planares, obteniéndose un PCE medio superior al 12%. Para mejorar la formulación de la perovskita y el rendimiento de los dispositivos, introdujimos un tercer catión de tipo A (MA^+) en un proceso de deposición de cuatro fuentes. De este modo, se obtuvieron capas homogéneas y células solares de bandgap ancho con un PCE de hasta el 15%.

5.2 Conclusión

En resumen, hemos investigado la deposición en vacío de perovskitas de bandgap ancho puras de yoduro, a temperatura ambiente. La deposición de $CsPbI_3$ a temperatura ambiente da lugar predominantemente a la formación de la fase δ amarilla, tal como se había descrito anteriormente. La fase negra puede estabilizarse con la incorporación de un catión mayor, DMAI, permitiendo la formación de una perovskita mixta $CsDMAPbI_3$ a temperatura ambiente. Hemos investigado las propiedades optoelectrónicas de este material en células solares p-i-n y n-i-p, donde n-i-p muestra un rendimiento superior, probablemente debido a un transporte de carga no ambipolar en el material. Hemos estudiado además el uso de un tercer catión, añadiendo formamidinio (FA^+) y metilamonio (MA^+) en un proceso de deposición en vacío de cuatro fuentes. El uso de MAI dio lugar a propiedades optoelectrónicas más favorables y, ajustando el espesor de la perovskita, se obtuvieron eficiencias prometedoras de hasta el 15%. Además, esta perovskita de triple catión puede recubrir de manera homogénea substratos de silicio texturizado, lo que hace que el material y el proceso sean prometedores para su aplicación en células solares de tipo tándem perovskita/silicio.

Capítulo 6: Conclusiones

El objetivo de esta tesis ha sido el desarrollo de perovskitas de bandgap ancho mediante métodos de sublimación en vacío, y su posterior aplicación en células solares.

En el tercer capítulo, desarrollamos un proceso de sublimación combinatoria de perovskitas del tipo $FA_{1-n}Cs_nPb(I_{1-x}Br_x)_3$, utilizando 4 fuentes y un portamuestras fijo, produciendo >100 células solares con distintas composiciones en una sola deposición. Para caracterizar estos materiales, empleamos diversas técnicas resueltas en el espacio, tanto ópticas, morfológicas como estructurales. A través de un ajuste fino de las velocidades de deposición, pudimos modificar el gradiente y reproducir las formulaciones más eficientes en deposiciones estándar con rotación. Este método muestra un gran potencial para el desarrollo de nuevas formulaciones de perovskita, de forma rápida y eficiente.

En el cuarto capítulo, presentamos un método que permite aumentar la complejidad de la formulación de capas de perovskita depositadas por sublimación, mediante deposición multifuente y mezcla de componentes inorgánicos y orgánicos. Lo empleamos en la preparación de células solares de perovskita de CsMAFA de bandgap ancho, que demuestran una alta eficiencia, pero baja estabilidad térmica. Para resolver este problema y mejorar la estabilidad de la perovskita, introducimos guanidinio en la formulación del material. Como resultado, obtuvimos con éxito capas de perovskita de cuatro cationes CsMAFAGA que presentan una estabilidad térmica mejorada, como confirmado por análisis microestructural en difracción de rayos X. Las células solares basadas en estas capas mostraron un rendimiento similar, pero con mejor estabilidad mejorada. Este estudio abre posibilidades para la fabricación por sublimación de composiciones aún más complejas de perovskita, lo que tiene implicaciones significativas no sólo en el campo de la fotovoltaica sino también en otras aplicaciones optoelectrónicas.

En el quinto capítulo, logramos estabilizar capas de perovskita $CsPbI_3$ a temperatura ambiente mediante la incorporación de un catión más grande, DMA^+. Hemos estudiado las propiedades optoelectrónicas de este material empleándolo en células solares de tipo p-i-n y n-i-p. La configuración n-i-p mostró un rendimiento superior, posiblemente atribuido al transporte de carga no ambipolar del material. Además, exploramos la incorporación de un tercer catión, como el formamidinio y el metilamonio, mediante sublimación con cuatro fuentes. La adición de MA^+ mejoró las propiedades optoelectrónicas y, ajustando el grosor de la perovskita, se consiguieron eficiencias prometedoras de hasta el 15% en células solares de perovskita de yodo de bandgap ancho.

Appendix A

Bibliography

[1] IEA, *Analysis and forecast to 2027*, **2022**.

[2] M. Perez, R. Perez, *Sol. Energy Adv.* **2022**, *2*, 100014.

[3] E. Becquerel, *The Discover of Photovoltaics*, **1839**.

[4] K. Ahmad, W. Raza, *Perovskite materials for energy and environmental applications*, **2021**.

[5] NREL, *Best Research-Cell Efficiency Chart*, **2023**.

[6] K. Yoshikawa, H. Kawasaki, W. Yoshida, T. Irie, K. Konishi, K. Nakano, T. Uto, D. Adachi, M. Kanematsu, H. Uzu, K. Yamamoto, *Nat. Energy* **2017**, *2*, 17032.

[7] M. A. Green, E. D. Dunlop, G. Siefer, M. Yoshita, N. Kopidakis, K. Bothe, X. Hao, *Prog. Photovoltaics Res. Appl.* **2023**, *31*, 3.

[8] M. A. Green, A. Ho-Baillie, H. J. Snaith, *Nat. Photonics* **2014**, *8*, 506.

[9] A. Kojima, K. Teshima, Y. Shirai, T. Miyasaka, *J. Am. Chem. Soc.* **2009**, *131*, 6050.

[10] J. H. Im, C. R. Lee, J. W. Lee, S. W. Park, N. G. Park, *Nanoscale* **2011**, *3*, 4088.

[11] H. S. Kim, C. R. Lee, J. H. Im, K. B. Lee, T. Moehl, A. Marchioro, S. J. Moon, R. Humphry-Baker, J. H. Yum, J. E. Moser, M. Grätzel, N. G. Park, *Sci. Rep.* **2012**, *2*, 1.

[12] C. A. Gueymard, D. Myers, K. Emery, **2003**, *73*, 443.

[13] W. Shockley, H. J. Queisser, **2004**, *519*, 510.

[14] A. Polman, M. Knight, E. C. Garnett, B. Ehrler, W. C. Sinke, *Science (80-.).* **2016**, *352*.

[15] M. Anaya, G. Lozano, M. E. Calvo, H. Míguez, *Joule* **2017**, *1*, 769.

[16] T. Leijtens, K. A. Bush, R. Prasanna, M. D. McGehee, *Nat. Energy* **2018**, *3*, 828.

[17] H. Li, W. Zhang, *Chem. Rev.* **2020**, *120*, 9835.

[18] A. De Vos, *J. Phys. D. Appl. Phys.* **1980**, *13*, 839.

[19] T. V Torchynska, G. Polupan, *Superf. y Vacío* **2004**, *17*, 21.

[20] M. A. Green, E. D. Dunlop, J. Hohl-Ebinger, M. Yoshita, N. Kopidakis, X. Hao,

Prog. Photovoltaics Res. Appl. **2022**, *30*, 3.

[21] V. M. Goldschmidt, B. Bhnlichkeit, E. Menschenalter, D. Arbeiten, E. Mi, F. Ax, *Zs.fass. Vor. gehalten Vor der Dtsch. Chem. Gesellschaf* **1927**, 1263.

[22] M. R. Filip, G. Volonakis, F. Giustino, *Hybrid Halide Perovskites: Fundamental Theory and Materials Design*, **2018**.

[23] O. J. Weber, D. Ghosh, S. Gaines, P. F. Henry, A. B. Walker, M. S. Islam, M. T. Weller, *Chem. Mater.* **2018**, *30*, 3768.

[24] Q. Zhao, A. Hazarika, L. T. Schelhas, J. Liu, E. A. Gaulding, G. Li, M. Zhang, M. F. Toney, P. C. Sercel, J. M. Luther, *ACS Energy Lett.* **2020**, *5*, 238.

[25] M. D. Smith, E. J. Crace, A. Jaffe, H. I. Karunadasa, *Annu. Rev. Mater. Res.* **2018**, *48*, 111.

[26] N. G. Park, *Mater. Today* **2015**, *18*, 65.

[27] M. J. P. Alcocer, T. Leijtens, L. M. Herz, A. Petrozza, H. J. Snaith, *Science (80-.).* **2013**, *342*, 341.

[28] G. Xing, N. Mathews, S. S. Lim, Y. M. Lam, S. Mhaisalkar, T. C. Sum, *Science (80-.).* **2013**, *6960*, 498.

[29] Q. Lin, A. Armin, R. C. R. Nagiri, P. L. Burn, P. Meredith, *Nat. Photonics* **2015**, *9*, 106.

[30] W. J. Yin, T. Shi, Y. Yan, *Adv. Mater.* **2014**, *26*, 4653.

[31] S. Tao, I. Schmidt, G. Brocks, J. Jiang, I. Tranca, K. Meerholz, S. Olthof, *Nat. Commun.* **2019**, *10*, 2560.

[32] L. Protesescu, S. Yakunin, M. I. Bodnarchuk, F. Krieg, R. Caputo, C. H. Hendon, R. X. Yang, A. Walsh, M. V. Kovalenko, *Nano Lett.* **2015**, *15*, 3692.

[33] E. T. Hoke, D. J. Slotcavage, E. R. Dohner, A. R. Bowring, H. I. Karunadasa, M. D. McGehee, *Chem. Sci.* **2015**, *6*, 613.

[34] K. A. Bush, K. Frohna, R. Prasanna, R. E. Beal, T. Leijtens, S. A. Swifter, M. D. McGehee, *ACS Energy Lett.* **2018**, *3*, 428.

[35] J. Xu, C. C. Boyd, Z. J. Yu, A. F. Palmstrom, D. J. Witter, B. W. Larson, R. M.

France, J. Werner, S. P. Harvey, E. J. Wolf, W. Weigand, S. Manzoor, M. F. A. M. Van Hest, J. J. Berry, J. M. Luther, Z. C. Holman, M. D. McGehee, *Science (80-.).* **2020**, *367*, 1097.

[36] D. P. McMeekin, G. Sadoughi, W. Rehman, G. E. Eperon, M. Saliba, M. T. Hörantner, A. Haghighirad, N. Sakai, L. Korte, B. Rech, M. B. Johnston, L. M. Herz, H. J. Snaith, *Science (80-.).* **2016**, *351*, 151.

[37] M. Saliba, T. Matsui, J. Y. Seo, K. Domanski, J. P. Correa-Baena, M. K. Nazeeruddin, S. M. Zakeeruddin, W. Tress, A. Abate, A. Hagfeldt, M. Grätzel, *Energy Environ. Sci.* **2016**, *9*, 1989.

[38] R. Prasanna, A. Gold-Parker, T. Leijtens, B. Conings, A. Babayigit, H. G. Boyen, M. F. Toney, M. D. McGehee, *J. Am. Chem. Soc.* **2017**, *139*, 11117.

[39] T. Duong, Y. L. Wu, H. Shen, J. Peng, X. Fu, D. Jacobs, E. C. Wang, T. C. Kho, K. C. Fong, M. Stocks, E. Franklin, A. Blakers, N. Zin, K. McIntosh, W. Li, Y. B. Cheng, T. P. White, K. Weber, K. Catchpole, *Adv. Energy Mater.* **2017**, *7*, 1.

[40] M. Abdi-Jalebi, Z. Andaji-Garmaroudi, S. Cacovich, C. Stavrakas, B. Philippe, J. M. Richter, M. Alsari, E. P. Booker, E. M. Hutter, A. J. Pearson, S. Lilliu, T. J. Savenije, H. Rensmo, G. Divitini, C. Ducati, R. H. Friend, S. D. Stranks, *Nature* **2018**, *555*, 497.

[41] L. Wang, G. Wang, Z. Yan, J. Qiu, C. Jia, W. Zhang, C. Zhen, C. Xu, K. Tai, X. Jiang, S. Yang, *Sol. RRL* **2020**, *4*, 1.

[42] Y. Zheng, T. Niu, X. Ran, J. Qiu, B. Li, Y. Xia, Y. Chen, W. Huang, *J. Mater. Chem. A* **2019**, *7*, 13860.

[43] Z. Wang, Q. Lin, F. P. Chmiel, N. Sakai, L. M. Herz, H. J. Snaith, *Nat. Energy* **2017**, *2*, 1.

[44] A. Rajagopal, R. J. Stoddard, S. B. Jo, H. W. Hillhouse, A. K. Y. Jen, *Nano Lett.* **2018**, *18*, 3985.

[45] Z. Xiao, L. Zhao, N. L. Tran, Y. L. Lin, S. H. Silver, R. A. Kerner, N. Yao, A. Kahn, G. D. Scholes, B. P. Rand, *Nano Lett.* **2017**, *17*, 6863.

[46] S. Gharibzadeh, B. Abdollahi Nejand, M. Jakoby, T. Abzieher, D. Hauschild, S.

Moghadamzadeh, J. A. Schwenzer, P. Brenner, R. Schmager, A. A. Haghighirad, L. Weinhardt, U. Lemmer, B. S. Richards, I. A. Howard, U. W. Paetzold, *Adv. Energy Mater*. **2019**, *9*, 1.

[47] A. F. Palmstrom, G. E. Eperon, T. Leijtens, R. Prasanna, S. N. Habisreutinger, W. Nemeth, E. A. Gaulding, S. P. Dunfield, M. Reese, S. Nanayakkara, T. Moot, J. Werner, J. Liu, B. To, S. T. Christensen, M. D. McGehee, M. F. A. M. van Hest, J. M. Luther, J. J. Berry, D. T. Moore, *Joule* **2019**, *3*, 2193.

[48] G. E. Eperon, K. H. Stone, L. E. Mundt, T. H. Schloemer, S. N. Habisreutinger, S. P. Dunfield, L. T. Schelhas, J. J. Berry, D. T. Moore, G. E. Eperon, D. T. Moore, *ACS Energy Lett.* **2020**, *5*, 1856.

[49] Y. Zhou, Y. Zhao, *Energy Environ. Sci.* **2019**, *12*, 1495.

[50] S. Dastidar, D. A. Egger, L. Z. Tan, S. B. Cromer, A. D. Dillon, S. Liu, L. Kronik, A. M. Rappe, A. T. Fafarman, *Nano Lett.* **2016**, *16*, 3563.

[51] A. Swarnkar, W. J. Mir, A. Nag, *ACS Energy Lett.* **2018**, *3*, 286.

[52] R. J. Sutton, G. E. Eperon, L. Miranda, E. S. Parrott, B. A. Kamino, J. B. Patel, M. T. Hörantner, M. B. Johnston, A. A. Haghighirad, D. T. Moore, H. J. Snaith, *Adv. Energy Mater.* **2016**, *6*, 1.

[53] K. Wang, Z. Jin, L. Liang, H. Bian, H. Wang, J. Feng, Q. Wang, S. (Frank) Liu, *Nano Energy* **2019**, *58*, 175.

[54] Z. Shao, Z. Wang, Z. Li, Y. Fan, H. Meng, R. Liu, Y. Wang, A. Hagfeldt, G. Cui, S. Pang, *Angew. Chemie - Int. Ed.* **2019**, *58*, 5587.

[55] Z. Li, M. Yang, J. S. Park, S. H. Wei, J. J. Berry, K. Zhu, *Chem. Mater.* **2016**, *28*, 284.

[56] T. Zhang, M. I. Dar, G. Li, F. Xu, N. Guo, M. Grätzel, Y. Zhao, *Sci. Adv.* **2017**, *3*, 1.

[57] Y. Zheng, X. Yang, R. Su, P. Wu, Q. Gong, R. Zhu, *Adv. Funct. Mater.* **2020**, *30*, 2000457.

[58] M. Tai, Y. Zhou, X. Yin, J. Han, Q. Zhang, Y. Zhou, H. Lin, *J. Mater. Chem. A* **2019**, *7*, 22675.

[59] Y. Jiang, J. Yuan, Y. Ni, J. Yang, Y. Wang, T. Jiu, M. Yuan, J. Chen, *Joule* **2018**, *2*,

1356.

[60] T. Li, J. Xu, R. Lin, S. Teale, H. Li, Z. Liu, C. Duan, Q. Zhao, K. Xiao, P. Wu, B. Chen, S. Jiang, S. Xiong, H. Luo, S. Wan, L. Li, Q. Bao, Y. Tian, X. Gao, J. Xie, E. H. Sargent, H. Tan, *Nat. Energy* **2023**, *8*, 610.

[61] X. Chu, Q. Ye, Z. Wang, C. Zhang, F. Ma, Z. Qu, Y. Zhao, Z. Yin, H.-X. Deng, X. Zhang, J. You, *Nat. Energy* **2023**, *8*, 372.

[62] J. Ávila, C. Momblona, P. P. Boix, M. Sessolo, H. J. Bolink, *Joule* **2017**, *1*, 431.

[63] G. Longo, C. Momblona, M. G. La-Placa, L. Gil-Escrig, M. Sessolo, H. J. Bolink, *ACS Energy Lett.* **2018**, *3*, 214.

[64] J. Huang, S. Xiang, J. Yu, C.-Z. Li, *Energy Environ. Sci.* **2019**, *12*, 929.

[65] R. Ji, Z. Zhang, C. Cho, Q. An, F. Paulus, M. Kroll, M. Löffler, F. Nehm, B. Rellinghaus, K. Leo, Y. Vaynzof, *J. Mater. Chem. C* **2020**, *8*, 7725.

[66] Y. H. Chiang, M. Anaya, S. D. Stranks, *ACS Energy Lett.* **2020**, *5*, 2498.

[67] L. Gil-Escrig, C. Dreessen, F. Palazon, Z. Hawash, E. Moons, S. Albrecht, M. Sessolo, H. J. Bolink, *ACS Energy Lett.* **2021**, *6*, 827.

[68] L. Gil-Escrig, C. Momblona, M. G. La-Placa, P. P. Boix, M. Sessolo, H. J. Bolink, *Adv. Energy Mater.* **2018**, *8*, 1.

[69] Q. Huang, F. Li, M. Wang, Y. Xiang, L. Ding, M. Liu, *Sci. Bull.* **2021**, *66*, 757.

[70] Z. Zhang, R. Ji, M. Kroll, Y. J. Hofstetter, X. Jia, D. Becker-Koch, F. Paulus, M. Löffler, F. Nehm, K. Leo, Y. Vaynzof, *Adv. Energy Mater.* **2021**, *11*, 1.

[71] N. J. Jeon, J. H. Noh, Y. C. Kim, W. S. Yang, S. Ryu, S. Il Seok, *Nat. Mater.* **2014**, *13*, 897.

[72] J. W. Jung, S. T. Williams, A. K. Y. Jen, *RSC Adv.* **2014**, *4*, 62971.

[73] J. Burschka, N. Pellet, S. J. Moon, R. Humphry-Baker, P. Gao, M. K. Nazeeruddin, M. Grätzel, *Nature* **2013**, *499*, 316.

[74] K. Liang, D. B. Mitzi, M. T. Prikas, *Chem. Mater.* **2013**, *4756*, 403.

[75] R. Swartwout, M. T. Hoerantner, V. Bulović, *Energy Environ. Mater.* **2019**, *2*, 119.

[76] J. Lee, K. Lee, K. Kim, N. G. Park, *Sol. RRL* **2022**, *6*, 1.

[77] D. B. Mitzi, M. T. Prikas, K. Chondroudis, *Chem. Mater.* **1999**, *11*, 542.

[78] G. Longo, L. Gil-Escrig, M. J. Degen, M. Sessolo, H. J. Bolink, *Chem. Commun.* **2015**, *51*, 7376.

[79] M. Era, T. Hattori, T. Taira, T. Tsutsui, *Chem. Mater.* **1997**, *9*, 8.

[80] M. Liu, M. B. Johnston, H. J. Snaith, *Nature* **2013**, *501*, 395.

[81] L. Zheng, D. Zhang, Y. Ma, Z. Lu, Z. Chen, S. Wang, L. Xiao, Q. Gong, *Dalt. Trans.* **2015**, *44*, 10582.

[82] C.-W. Chen, H.-W. Kang, S.-Y. Hsiao, P.-F. Yang, K.-M. Chiang, H.-W. Lin, *Adv. Mater.* **2014**, *26*, 6647.

[83] J. Jeong, M. Kim, J. Seo, H. Lu, P. Ahlawat, A. Mishra, Y. Yang, M. A. Hope, F. T. Eickemeyer, M. Kim, Y. J. Yoon, I. W. Choi, B. P. Darwich, S. J. Choi, Y. Jo, J. H. Lee, B. Walker, S. M. Zakeeruddin, L. Emsley, U. Rothlisberger, A. Hagfeldt, D. S. Kim, M. Grätzel, J. Y. Kim, *Nature* **2021**, *592*, 381.

[84] Z. Hawash, L. K. Ono, Y. Qi, *Adv. Mater. Interfaces* **2018**, *5*, 1700623.

[85] W. S. Yang, J. H. Noh, N. J. Jeon, Y. C. Kim, S. Ryu, J. Seo, S. Il Seok, *Science (80-.).* **2015**, *348*, 1234.

[86] W. Chen, Y. Wu, Y. Yue, J. Liu, W. Zhang, X. Yang, H. Chen, E. Bi, I. Ashraful, M. Grätzel, L. Han, *Science (80-.).* **2015**, *350*, 944.

[87] K. A. Bush, C. D. Bailie, Y. Chen, A. R. Bowring, W. Wang, W. Ma, T. Leijtens, F. Moghadam, M. D. McGehee, *Adv. Mater.* **2016**, *28*, 3937.

[88] T. H. Schloemer, J. A. Christians, J. M. Luther, A. Sellinger, *Chem. Sci.* **2019**, *10*, 1904.

[89] S. S. Shin, S. J. Lee, S. Il Seok, *Adv. Funct. Mater.* **2019**, *29*, 1.

[90] N. B. Kotadiya, H. Lu, A. Mondal, Y. Ie, D. Andrienko, P. W. M. Blom, G. J. A. H. Wetzelaer, *Nat. Mater.* **2018**, *17*, 329.

[91] C. Momblona, L. Gil-Escrig, E. Bandiello, E. M. Hutter, M. Sessolo, K. Lederer, J. Blochwitz-Nimoth, H. J. Bolink, *Energy Environ. Sci.* **2016**, *9*, 3456.

[92] J. Avila, L. Gil-Escrig, P. P. Boix, M. Sessolo, S. Albrecht, H. J. Bolink, *Sustain. Energy Fuels* **2018**, *2*, 2429.

[93] E. Castro, J. Murillo, O. Fernandez-Delgado, L. Echegoyen, *J. Mater. Chem. C* **2018**, *6*, 2635.

[94] H. Gommans, B. Verreet, B. P. Rand, R. Muller, J. Poortmans, P. Heremans, J. Genoe, *Adv. Funct. Mater.* **2008**, *18*, 3686.

[95] W. H. Lee, C. Y. Chen, C. S. Li, S. Y. Hsiao, W. L. Tsai, M. J. Huang, C. H. Cheng, C. I. Wu, H. W. Lin, *Nano Energy* **2017**, *38*, 66.

[96] K. Wang, M. Neophytou, E. Aydin, M. Wang, T. Laurent, G. T. Harrison, J. Liu, W. Liu, M. De Bastiani, J. I. Khan, T. D. Anthopoulos, F. Laquai, S. De Wolf, *Adv. Mater. Interfaces* **2019**, *6*, 1.

[97] X. Liu, H. Yu, L. Yan, Q. Dong, Q. Wan, Y. Zhou, B. Song, Y. Li, *ACS Appl. Mater. Interfaces* **2015**, *7*, 6230.

[98] A. Y. Anderson, Y. Bouhadana, H.-N. Barad, B. Kupfer, E. Rosh-Hodesh, H. Aviv, Y. R. Tischler, S. Rühle, A. Zaban, *ACS Comb. Sci.* **2014**, *16*, 53.

[99] Z. Li, T. R. Klein, D. H. Kim, M. Yang, J. J. Berry, M. F. A. M. van Hest, K. Zhu, *Nat. Rev. Mater.* **2018**, *3*, 18017.

[100] Q. Guesnay, F. Sahli, C. Ballif, Q. Jeangros, *APL Mater.* **2021**, *9*.

[101] Y. Jiang, S. He, L. Qiu, Y. Zhao, Y. Qi, *Appl. Phys. Rev.* **2022**, *9*, 021305.

[102] S. R. Bae, D. Y. Heo, S. Y. Kim, *Mater. Today Adv.* **2022**, *14*, 100232.

[103] M. Liu, M. B. Johnston, H. J. Snaith, *Nature* **2013**, *501*, 395.

[104] V. S. Chirvony, K. S. Sekerbayev, D. Pérez-del-Rey, J. P. Martínez-Pastor, F. Palazon, P. P. Boix, T. I. Taurbayev, M. Sessolo, H. J. Bolink, *J. Phys. Chem. Lett.* **2019**, *10*, 5167.

[105] J. B. Patel, A. D. Wright, K. B. Lohmann, K. Peng, C. Q. Xia, J. M. Ball, N. K. Noel, T. W. Crothers, J. Wong-Leung, H. J. Snaith, L. M. Herz, M. B. Johnston, *Adv. Energy Mater.* **2020**, *10*, 1903653.

[106] J. Li, H. Wang, X. Y. Chin, H. A. Dewi, K. Vergeer, T. W. Goh, J. W. M. Lim, J. H.

Lew, K. P. Loh, C. Soci, T. C. Sum, H. J. Bolink, N. Mathews, S. Mhaisalkar, A. Bruno, *Joule* **2020**, *4*, 1035.

[107] M. Saliba, *Adv. Energy Mater.* **2019**, *9*, 1803754.

[108] X.-D. Xiang, *Annu. Rev. Mater. Sci.* **1999**, *29*, 149.

[109] L. Gouda, K. J. Rietwyk, J. Hu, A. Kama, A. Ginsburg, M. Priel, D. A. Keller, S. Tirosh, S. Meir, R. Gottesman, A. Zaban, *ACS Energy Lett.* **2017**, *2*, 2356.

[110] H.-N. Barad, M. Alarcón-Correa, G. Salinas, E. Oren, F. Peter, A. Kuhn, P. Fischer, *Mater. Today* **2021**, *50*, 89.

[111] P. J. McGinn, *ACS Comb. Sci.* **2019**, *21*, 501.

[112] I. Takeuchi, R. B. van Dover, H. Koinuma, *MRS Bull.* **2002**, *27*, 301.

[113] R. Potyrailo, K. Rajan, K. Stoewe, I. Takeuchi, B. Chisholm, H. Lam, *ACS Comb. Sci.* **2011**, *13*, 579.

[114] H. Näsström, P. Becker, J. A. Márquez, O. Shargaieva, R. Mainz, E. Unger, T. Unold, *J. Mater. Chem. A* **2020**, *8*, 22626.

[115] S. Moradi, S. Kundu, M. Rezazadeh, V. Yeddu, O. Voznyy, M. I. Saidaminov, *Commun. Mater.* **2022**, *3*, 13.

[116] X. Cao, L. Zhi, Y. Jia, Y. Li, K. Zhao, X. Cui, L. Ci, D. Zhuang, J. Wei, *ACS Appl. Mater. Interfaces* **2019**, *11*, 7639.

[117] M. Lv, X. Dong, X. Fang, B. Lin, S. Zhang, J. Ding, N. Yuan, *RSC Adv.* **2015**, *5*, 20521.

[118] I. Lignos, S. Stavrakis, G. Nedelcu, L. Protesescu, A. J. DeMello, M. V. Kovalenko, *Nano Lett.* **2016**, *16*, 1869.

[119] H. Anwar, A. Johnston, S. Mahesh, K. Singh, Z. Wang, D. A. Kuntz, I. Tamblyn, O. Voznyy, G. G. Privé, E. H. Sargent, *ACS Cent. Sci.* **2022**.

[120] Y. Zhao, J. Zhang, Z. Xu, S. Sun, S. Langner, N. T. P. Hartono, T. Heumueller, Y. Hou, J. Elia, N. Li, G. J. Matt, X. Du, W. Meng, A. Osvet, K. Zhang, T. Stubhan, Y. Feng, J. Hauch, E. H. Sargent, T. Buonassisi, C. J. Brabec, *Nat. Commun.* **2021**, *12*, 2191.

[121] Y. Zhao, T. Heumueller, J. Zhang, J. Luo, O. Kasian, S. Langner, C. Kupfer, B. Liu, Y. Zhong, J. Elia, A. Osvet, J. Wu, C. Liu, Z. Wan, C. Jia, N. Li, J. Hauch, C. J. Brabec, *Nat. Energy* **2022**, *7*, 144.

[122] K. Kawashima, Y. Okamoto, O. Annayev, N. Toyokura, R. Takahashi, M. Lippmaa, K. Itaka, Y. Suzuki, N. Matsuki, H. Koinuma, *Sci. Technol. Adv. Mater.* **2017**, *18*, 307.

[123] P. Becker, J. A. Márquez, J. Just, A. Al-Ashouri, C. Hages, H. Hempel, M. Jošt, S. Albrecht, R. Frahm, T. Unold, *Adv. Energy Mater.* **2019**, *9*, 16.

[124] J. Li, P. Du, S. Li, J. Liu, M. Zhu, Z. Tan, M. Hu, J. Luo, D. Guo, L. Ma, Z. Nie, Y. Ma, L. Gao, G. Niu, J. Tang, *Adv. Funct. Mater.* **2019**, *29*, 1903607.

[125] I. Levine, O. G. Vera, M. Kulbak, D.-R. Ceratti, C. Rehermann, J. A. Márquez, S. Levcenko, T. Unold, G. Hodes, I. Balberg, D. Cahen, T. Dittrich, *ACS Energy Lett.* **2019**, *4*, 1150.

[126] I. Levine, K. Shimizu, A. Lomuscio, M. Kulbak, C. Rehermann, A. Zohar, M. Abdi-Jalebi, B. Zhao, S. Siebentritt, F. Zu, N. Koch, A. Kahn, G. Hodes, R. H. Friend, H. Ishii, D. Cahen, *J. Phys. Chem. C* **2021**, *125*, 5217.

[127] Q. A. Akkerman, L. Manna, *ACS Energy Lett.* **2020**, *5*, 604.

[128] F. Palazon, D. Pérez-del-Rey, B. Dänekamp, C. Dreessen, M. Sessolo, P. P. Boix, H. J. Bolink, *Adv. Mater.* **2019**, *31*, 1902692.

[129] M. T. Weller, O. J. Weber, P. F. Henry, A. M. Di Pumpo, T. C. Hansen, *Chem. Commun.* **2015**, *51*, 4180.

[130] D. H. Cao, C. C. Stoumpos, C. D. Malliakas, M. J. Katz, O. K. Farha, J. T. Hupp, M. G. Kanatzidis, *APL Mater.* **2014**, *2*, 091101.

[131] S. Mahesh, J. M. Ball, R. D. J. Oliver, D. P. McMeekin, P. K. Nayak, M. B. Johnston, H. J. Snaith, *Energy Environ. Sci.* **2020**, *13*, 258.

[132] D. W. deQuilettes, K. Frohna, D. Emin, T. Kirchartz, V. Bulovic, D. S. Ginger, S. D. Stranks, *Chem. Rev.* **2019**, *119*, 11007.

[133] C. M. Wolff, P. Caprioglio, M. Stolterfoht, D. Neher, *Adv. Mater.* **2019**, *31*, 1902762.

[134] E. T. Hoke, D. J. Slotcavage, E. R. Dohner, A. R. Bowring, H. I. Karunadasa, M. D. McGehee, *Chem. Sci.* **2015**, *6*, 613.

[135] D. J. Slotcavage, H. I. Karunadasa, M. D. McGehee, *ACS Energy Lett.* **2016**, *1*, 1199.

[136] A. J. Knight, L. M. Herz, *Energy Environ. Sci.* **2020**, *13*, 2024.

[137] D. P. McMeekin, G. Sadoughi, W. Rehman, G. E. Eperon, M. Saliba, M. T. Hörantner, A. Haghighirad, N. Sakai, L. Korte, B. Rech, M. B. Johnston, L. M. Herz, H. J. Snaith, *Science (80-.).* **2016**, *351*, 151.

[138] U. Rau, *Phys. Rev. B - Condens. Matter Mater. Phys.* **2007**, *76*, 1.

[139] G. E. Eperon, S. D. Stranks, C. Menelaou, M. B. Johnston, L. M. Herz, H. J. Snaith, *Energy Environ. Sci.* **2014**, *7*, 982.

[140] R. J. Sutton, G. E. Eperon, L. Miranda, E. S. Parrott, B. A. Kamino, J. B. Patel, M. T. Hörantner, M. B. Johnston, A. A. Haghighirad, D. T. Moore, H. J. Snaith, *Adv. Energy Mater.* **2016**, *6*.

[141] J. H. Noh, S. H. Im, J. H. Heo, T. N. Mandal, S. Il Seok, *Nano Lett.* **2013**, *13*, 1764.

[142] G. E. Eperon, T. Leijtens, K. A. Bush, R. Prasanna, T. Green, J. T.-W. Wang, D. P. McMeekin, G. Volonakis, R. L. Milot, R. May, A. Palmstrom, D. J. Slotcavage, R. A. Belisle, J. B. Patel, E. S. Parrott, R. J. Sutton, W. Ma, F. Moghadam, B. Conings, A. Babayigit, H.-G. Boyen, S. Bent, F. Giustino, L. M. Herz, M. B. Johnston, M. D. McGehee, H. J. Snaith, *Science (80-.).* **2016**, *354*, 861.

[143] F. Sahli, J. Werner, B. A. Kamino, M. Bräuninger, R. Monnard, B. Paviet-Salomon, L. Barraud, L. Ding, J. J. Diaz Leon, D. Sacchetto, G. Cattaneo, M. Despeisse, M. Boccard, S. Nicolay, Q. Jeangros, B. Niesen, C. Ballif, *Nat. Mater.* **2018**, *17*, 820.

[144] Q. Han, Y.-T. Hsieh, L. Meng, J.-L. Wu, P. Sun, E.-P. Yao, S.-Y. Chang, S.-H. Bae, T. Kato, V. Bermudez, Y. Yang, *Science (80-.).* **2018**, *361*, 904.

[145] J. Tong, Z. Song, D. H. Kim, X. Chen, C. Chen, A. F. Palmstrom, P. F. Ndione, M. O. Reese, S. P. Dunfield, O. G. Reid, J. Liu, F. Zhang, S. P. Harvey, Z. Li, S. T. Christensen, G. Teeter, D. Zhao, M. M. Al-Jassim, M. F. A. M. van Hest, M. C. Beard, S. E. Shaheen, J. J. Berry, Y. Yan, K. Zhu, *Science (80-.).* **2019**, *364*, 475.

[146] A. Al-Ashouri, E. Köhnen, B. Li, A. Magomedov, H. Hempel, P. Caprioglio, J. A. Márquez, A. B. Morales Vilches, E. Kasparavicius, J. A. Smith, N. Phung, D. Menzel, M. Grischek, L. Kegelmann, D. Skroblin, C. Gollwitzer, T. Malinauskas, M. Jošt, G. Matič, B. Rech, R. Schlatmann, M. Topič, L. Korte, A. Abate, B. Stannowski, D. Neher, M. Stolterfoht, T. Unold, V. Getautis, S. Albrecht, *Science (80-.).* **2020**, *370*, 1300.

[147] G. Coletti, S. L. Luxembourg, L. J. Geerligs, V. Rosca, A. R. Burgers, Y. Wu, L. Okel, M. Kloos, F. J. K. Danzl, M. Najafi, D. Zhang, I. Dogan, V. Zardetto, F. Di Giacomo, J. Kroon, T. Aernouts, J. Hüpkes, C. H. Burgess, M. Creatore, R. Andriessen, S. Veenstra, *ACS Energy Lett.* **2020**, *5*, 1676.

[148] R. Lin, J. Xu, M. Wei, Y. Wang, Z. Qin, Z. Liu, J. Wu, K. Xiao, B. Chen, S. M. Park, G. Chen, H. R. Atapattu, K. R. Graham, J. Xu, J. Zhu, L. Li, C. Zhang, E. H. Sargent, H. Tan, *Nature* **2022**, *603*, 73.

[149] S. Gharibzadeh, B. Abdollahi Nejand, M. Jakoby, T. Abzieher, D. Hauschild, S. Moghadamzadeh, J. A. Schwenzer, P. Brenner, R. Schmager, A. A. Haghighirad, L. Weinhardt, U. Lemmer, B. S. Richards, I. A. Howard, U. W. Paetzold, *Adv. Energy Mater.* **2019**, *9*, 1803699.

[150] F. Peña-Camargo, P. Caprioglio, F. Zu, E. Gutierrez-Partida, C. M. Wolff, K. Brinkmann, S. Albrecht, T. Riedl, N. Koch, D. Neher, M. Stolterfoht, *ACS Energy Lett.* **2020**, *5*, 2728.

[151] H. Xie, M. Lira-Cantu, *J. Phys. Energy* **2020**, *2*, 024008.

[152] A. M. Igual-Muñoz, J. Navarro-Alapont, C. Dreessen, F. Palazon, M. Sessolo, H. J. Bolink, *Chem. Mater.* **2020**, *32*, 8641.

[153] A. D. Jodlowski, C. Roldán-Carmona, G. Grancini, M. Salado, M. Ralaiarisoa, S. Ahmad, N. Koch, L. Camacho, G. de Miguel, M. K. Nazeeruddin, *Nat. Energy* **2017**, *2*, 972.

[154] O. Nazarenko, M. R. Kotyrba, S. Yakunin, M. Aebli, G. Rainò, B. M. Benin, M. Wörle, M. V. Kovalenko, *J. Am. Chem. Soc.* **2018**, *140*, 3850.

[155] W. Zhang, J. Xiong, J. Li, W. A. Daoud, *J. Mater. Chem. A* **2019**, *7*, 9486.

[156] D. J. Kubicki, D. Prochowicz, A. Hofstetter, M. Saski, P. Yadav, D. Bi, N. Pellet, J.

Lewiński, S. M. Zakeeruddin, M. Grätzel, L. Emsley, *J. Am. Chem. Soc.* **2018**, *140*, 3345.

[157] R. J. Stoddard, A. Rajagopal, R. L. Palmer, I. L. Braly, A. K. Y. Jen, H. W. Hillhouse, *ACS Energy Lett.* **2018**, *3*, 1261.

[158] D. W. Ferdani, S. R. Pering, D. Ghosh, P. Kubiak, A. B. Walker, S. E. Lewis, A. L. Johnson, P. J. Baker, M. S. Islam, P. J. Cameron, *Energy Environ. Sci.* **2019**, *12*, 2264.

[159] L. Gil-Escrig, C. Dreessen, I. C. Kaya, B. S. Kim, F. Palazon, M. Sessolo, H. J. Bolink, *ACS Energy Lett.* **2020**, *5*, 3053.

[160] S. Van Reenen, M. Kemerink, H. J. Snaith, *J. Phys. Chem. Lett.* **2015**, *6*, 3808.

[161] P. Calado, A. M. Telford, D. Bryant, X. Li, J. Nelson, B. C. O'Regan, P. R. F. Barnes, *Nat. Commun.* **2016**, *7*, 1.

[162] S. Rühle, *Sol. Energy* **2016**, *130*, 139.

[163] C. C. Stoumpos, C. D. Malliakas, M. G. Kanatzidis, *Inorg. Chem.* **2013**, *52,* 9019.

[164] H. A. Dewi, J. Li, H. Wang, B. Chaudhary, N. Mathews, S. Mhaisalkar, A. Bruno, *Adv. Funct. Mater.* **2021**, *31*, 2100557.

[165] I. C. Kaya, K. P. S. Zanoni, F. Palazon, M. Sessolo, H. Akyildiz, S. Sonmezoglu, H. J. Bolink, *Adv. Energy Sustain. Res.* **2021**, *2*, 2000065.

[166] M. Roß, S. Severin, M. B. Stutz, P. Wagner, H. Köbler, M. Favin-Lévêque, A. Al-Ashouri, P. Korb, P. Tockhorn, A. Abate, B. Stannowski, B. Rech, S. Albrecht, *Adv. Energy Mater.* **2021**, *11*, 2101460.

[167] B. Zhao, S. F. Jin, S. Huang, N. Liu, J. Y. Ma, D. J. Xue, Q. Han, J. Ding, Q. Q. Ge, Y. Feng, J. S. Hu, *J. Am. Chem. Soc.* **2018**, *140*, 11716.

[168] L. A. Muscarella, E. M. Hutter, S. Sanchez, C. D. Dieleman, T. J. Savenije, A. Hagfeldt, M. Saliba, B. Ehrler, *J. Phys. Chem. Lett.* **2019**, *10*, 6010.

[169] M. Saliba, T. Matsui, K. Domanski, J. Seo, A. Ummadisingu, S. M. Zakeeruddin, J. P. Correa-Baena, W. R. Tress, A. Abate, A. Hagfeldt, M. Gratzel, *Science (80-.).* **2016**, *5557*, 1.

[170] G. Kim, H. Min, K. S. Lee, D. Y. Lee, S. M. Yoon, S. Il Seok, *Science (80-.).* **2020**, *370*, 108.

[171] I. M. Pavlovetc, M. C. Brennan, S. Draguta, A. Ruth, T. Moot, J. A. Christians, K. Aleshire, S. P. Harvey, S. Toso, S. U. Nanayakkara, J. Messinger, J. M. Luther, M. Kuno, *ACS Energy Lett.* **2020**, *5*, 2802.

[172] X. Zheng, Y. Hou, C. Bao, J. Yin, F. Yuan, Z. Huang, K. Song, J. Liu, J. Troughton, N. Gasparini, C. Zhou, Y. Lin, D. J. Xue, B. Chen, A. K. Johnston, N. Wei, M. N. Hedhili, M. Wei, A. Y. Alsalloum, P. Maity, B. Turedi, C. Yang, D. Baran, T. D. Anthopoulos, Y. Han, Z. H. Lu, O. F. Mohammed, F. Gao, E. H. Sargent, O. M. Bakr, *Nat. Energy* **2020**, *5*, 131.

[173] S.-H. Turren-Cruz, A. Hagfeldt, M. Saliba, *Science (80-.).* **2018**, *362*, 449.

[174] M. B. Faheem, B. Khan, C. Feng, M. U. Farooq, F. Raziq, Y. Xiao, Y. Li, *ACS Energy Lett.* **2020**, *5*, 290.

[175] A. R. Marshall, H. C. Sansom, M. M. McCarthy, J. H. Warby, O. J. Ashton, B. Wenger, H. J. Snaith, *Sol. RRL* **2021**, *5*.

[176] H. Meng, Z. Shao, L. Wang, Z. Li, R. Liu, Y. Fan, G. Cui, S. Pang, *ACS Energy Lett.* **2020**, *5*, 263.

[177] W. Ke, I. Spanopoulos, C. C. Stoumpos, M. G. Kanatzidis, *Nat. Commun.* **2018**, *9*.

[178] Y. Wang, X. Liu, T. Zhang, X. Wang, M. Kan, J. Shi, Y. Zhao, *Angew. Chemie* **2019**, *131*, 16844.

[179] R. Ji, Z. Zhang, Y. J. Hofstetter, R. Buschbeck, C. Hänisch, F. Paulus, Y. Vaynzof, *Nat. Energy* **2022**, *7*, 1170.

[180] I. Susic, A. Kama, L. Gil-Escrig, C. Dreessen, F. Palazon, D. Cahen, M. Sessolo, H. J. Bolink, *Adv. Mater. Interfaces* **2022**.

[181] 2 Abhishek Swarnkar, 1, 3 Ashley R. Marshall, 1, E. M. Sanehira, 4 Boris D. Chernomordik 1, 1 1 David T. Moore, J. A., 1 Christians, 5 Joseph M. Luther1* Tamoghna Chakrabarti, *Science (80-.).* **2016**, *354*, 92.

[182] P. Sebastia-Luna, M. Sessolo, F. Palazon, H. J. Bolink, *Energy Technol.* **2021**, *9*, 1.

[183] R. C. Shallcross, S. Olthof, K. Meerholz, N. R. Armstrong, *ACS Appl. Mater.*

Interfaces **2019**, *11*, 32500.

[184] D. Pérez-Del-Rey, P. P. Boix, M. Sessolo, A. Hadipour, H. J. Bolink, *J. Phys. Chem. Lett.* **2018**, *9*, 1041.

[185] N. Tessler, Y. Vaynzof, *ACS Energy Lett.* **2020**, *5*, 1260.

[186] J. W. Lee, S. Tan, S. Il Seok, Y. Yang, N. G. Park, *Science (80-.).* **2022**, *375*.

Appendix B

List of Abbreviations

2D	Two dimensional
3D	Three dimensional
BSE	Backscattered electrons
CB	Conduction band
CCS	Continuous compositional spread
CIGS	Copper indium gallium selenide
CMS	Combinatorial materials science
CdTe	Cadmium telluride
DMF	Dimethyl formamide
DMSO	Dimethyl sulfoxide
DPO	2-(1,10-phenanthrolin-3-yl) naphth-6-yl)diphenylphosphine oxide
DSSC	Dye sensitized solar cell
EDS	Energy-dispersive x-ray spectroscopy
EQE	External quantum efficiency
ETL	Electron-transport layer
E_g	Bandgap
FF	Fill factor
FTO	Fluorine doped tin oxide
GaAs	Gallium arsenide
GBA	γ-butyrolactone
HTL	Hole-transport layer
HTM	Hole-transport material
ITO	Indium tin oxide
J-V curve	Current-voltage curve

J_{sc}	Short-circuit current density
LED	Light emitting diode
NREL	National Renewable Energy Laboratory
OLED	Organic Light-Emitting Diode
OSC	Organic solar cells
$PbBr_2$	Lead bromide
PbI_2	Lead iodide
PCE	Power Conversion Efficiency
PL	Photoluminescence
PLQY	Photoluminescence Quantum Yield
PSC	Perovskite solar cell
PTAA	Poly(triaryl)amine
PV	Photovoltaic
QCM	Quartz crystal microbalance
QD	Quantum dot
QFLS	Quasi-Fermi level splitting
RT	Room temperature
SE	Secondary Electrons
SEM	Scanning Electron Microscopy
TCO	Transparent Conductive Oxide
UV-Vis	Ultraviolet-Visible
V_{oc}	Open-circuit voltage
VB	Valence band
WF	Work function

XRD	X-Ray Diffraction

Appendix C

Index of Figures and Tables

Index of Figures

Figure 1.18. Schematic illustration of a) multiple source vacuum-deposition and b) two-step single source vacuum-deposition processes.

Figure 1.19. Schematic diagram of n-i-p and p-i-n solar cell architectures. Blue arrows indicate the direction of the sunlight.

Figure 1.20. Energy band diagram of a typical solar cell with schematic electron and hole extraction.

Figure 2.1. Scheme of the p-i-n solar cells employed in (a) Chapter 3 (b) Chapter 4 (c) Chapter 5 and (d) n-i-p solar cells employed in Chapter 5.

Figure 2.2. Picture of the baseplate of the evaporation chamber employed for the deposition of perovskite thin films.

Figure 2.3. (a) Top view of the substrate holder, position of the thermal sources, dimensions and layout of a single substrate. (b) Schematic illustration of evaporation chamber.

Figure 3.1. Details of the setup and device layout used in the combinatorial study. (a) Top view of the substrate holder, position of the thermal sources, dimensions and layout of a single substrate. (b) Without sample rotation, a gradient of each precursor is deposited on the substrate, resulting in CCS library of thin film perovskites. (c) Device architecture that was used in this study.

Figure 3.2. Results of combinatorial deposition of wide bandgap perovskite solar cells. 112 points color maps for J_{sc}, V_{oc}, (top) FF, and PCE (bottom) are shown together with the J-V curves for each substrate (the mathematical average of all J-V curves for each substrate are shown as a thick blue line). The deposition rates for PbI_2, $PbBr_2$, CsI and FAI are those reported in Table 4.1 as the initial parameter set.

Figure 3.3. Results of combinatorial deposition of wide bandgap perovskite solar cells. 112 points color maps for J_{sc}, V_{oc}, (top), FF, and PCE (bottom) are shown together with the J-V curves for each substrate (the mathematical average of all J-V curves for each substrate are shown as a thick red line). The deposition rates for PbI_2, $PbBr_2$ and FAI are the same as in Figure 4.2, while the r(CsI) is increased from (a) 0.4 Å/s to (b) 0.5 Å/s.

Figure 3.4. Structural and morphological analysis of the material library. (a) Selected XRD patterns for each of the 7 substrates, highlighting the most relevant regions (2θ = 12° - 15° and 2θ = 27° - 31° approximately). (b) Color map of the ratio between the calculated intensities of the (001) peak from PbI_2 (around 2θ = 12.7°) and the (020) peak of the perovskite phase (around 2θ = 14.3°). (c) Color map of the intensity ratio between the sum

of (122) and (221) peaks over the main (040) one, where lower values indicate predominance of the higher symmetry cubic phase over tetragonal and/or orthorhombic distortions. (d) SEM images of selected areas of the surfaces of the seven substrates.

Figure 3.5. XRD patterns for selected corners of the seven substrates on the sample holders, as indicated in the upper scheme. Whole-pattern Le Bail fit (red line) of XRD patterns (open black circles). Vertical markers correspond to calculated Bragg's reflections for perovskite phase (yellow), PbI_2 (green) and Al (blue). The Al reflections come from the ample stage of the XRD tool, and is seen sometimes if the sample is not perfectly aligned with the X-ray beam.

Figure 3.6. XRD patterns (same locations as in Figure 3.5) overlapped without normalization in (a) linear and (b) semi-logarithmic scale.

Figure 3.7. Optical and elemental characterization of the library of materials. (a) Bandgap (E_g) color map extracted from spatially resolved optical absorption. (b) PLQY map, measured at the corners of each substrate. (c) Representative absorption (blue) and PL (red) spectra for each substrate. EDS color map of (d) Br/(Br+I) and (e) Cs/Pb concentration ratios.

Figure 3.8. PL spectra for perovskite thin films at different locations of the material library (position in the sample holder is highlighted in the inset), showing (a) stable PL shape and (b) peak splitting due to photoinduced halide segregation. Samples are excited with a 522 nm CW laser with an intensity corresponding to approximately 1 sun.

Figure 3.9. (a) QFLS map calculated from PLQY measurement on perovskite films using the reciprocity relation and (b) V_{oc} map for solar cells obtained with the same deposition parameters: $r(PbI_2)$ = 1.0 Å/s; $r(PbBr_2)$ = 0.2 Å/s; r(FAI) = 0.8 Å/s; r(CsI) = 0.5 Å/s.

Figure 3.10. Comparison of solar cells obtained with fixed and rotating sample holders. (a) J-V curves under illumination for solar cells in the center of a non-rotating (fixed) sample holder and (b) J-V curves under illumination for solar cells obtained in a controlled deposition with sample rotation (the J-V curves for two substrates, one on the center and one on the edge of the sample holder are reported). Light colors indicate J-V curves for each single pixel, while the thick lines are the mathematical average of all J-V curves. The inset in (a) and (b) show the PL spectra fitted with a Voigt function to quantify the peak center. (c) Distribution of the PV parameters for the two sets of solar cells, obtained without and with sample rotation. The same deposition rates are used: $r(PbI_2)$ = 1.0 Å/s; $r(PbBr_2)$ = 0.2 Å/s; r(FAI) = 0.8 Å/s; r(CsI) = 0.5 Å/s.

absorption spectra of a 500 nm thick film with corresponding (d) Tauc plot to estimate the bandgap. (e) Calibrated absolute photoluminescence spectra of the same film upon excitation with a 515 nm laser light source.

Figure 4.8. XRD patterns for quadruple-cation CsMAFAGA perovskite films measured periodically ex situ during (a) light soaking or (b) thermal stress.

Figure 4.9. (a)Whole-pattern fit of quadruple-cation CsMAFAGA perovskite thin film after 2 days at 85 ºC. A single orthorhombic perovskite phase is considered in addition to PbI_2. (b) Williamson-Hall plots (inverse integral breadth versus inverse interatomic distance) for quadruple-cation films upon thermal stress. The most noticeable effect is a suppression of microstrain, related to the slope of the graph. Average crystallite size (inverse of extrapolated value at $d^* = 0$) does not change significantly and remain around 100 nm.

Figure 4.10. Low angle XRD patterns for quadruple-cation CsMAFAGA films upon ageing at 85 ºC, highlighting the formation of yellow phases.

Figure 4.11. (a) J-V curves under illumination for a representative solar cells using a quadruple-cation CsMAFAGA perovskite as the absorber layer. The J-V curves are collected in forward (from short to open circuit, solid line) and reverse scan direction (from open to short circuit, dashed line). (b) Maximum power point tracking under simulated solar illumination for an encapsulated CsMAFAGA device, measured in inert atmosphere. (c) Shelf life thermal stability test for a similar solar cell: PV parameters extracted from J-V curves taken at different times for a device kept at 85 °C on a hot plate in nitrogen atmosphere.

Figure 4.12. J-V curves under illumination for quadruple cation CsMAFAGA perovskite solar cell, as-prepared and after annealing at 85 °C for 1 hour. The curves correspond in particular to (a) a well-working device and (b) for a faulty pixel. After annealing, the (c) PV parameters are essentially unvaried for the well working device, while they are found to be substantially improved for the initially faulty solar cells.

Figure 4.13. Schematics of GA^+ dynamic incorporation in vacuum-deposited, quadruple cation CsMAFAGA perovskite films. GA^+ initially accumulates at the grain boundaries, but upon annealing is progressively incorporated into the perovskite structure, stabilizing the material and preventing degradation.

Figure 5.1. (a) Photograph of the sample holder with 7 as-deposited films after (a) 2-sources and (b) 3-sources vacuum deposition without sample rotation. The position of the thermal sources with respect to the sample holder and the corresponding materials are also reported.

(c) Optical absorption and (d) photoluminescence spectra of a series of CsDMAPbI$_3$ perovskite films with varying DMA deposition rates, obtained with sample rotation.

Figure 5.2. (a) Device layout for p-i-n and n-i-p cells used in this study. (b) Representative J−V curves for CsDMAPbI$_3$ solar cells, obtained with r_{DMA} = 0.2 Å/s. The J−V curves are collected in forward (from short to open circuit, solid line) and reverse scan directions (from open to short circuit, dashed line). (c) PV parameters extracted from the same J-V curves.

Figure 5.3. XRD pattern of a thin perovskite film deposited on ITO, obtained by co-sublimation of PbI$_2$ (1.2 Å/s), CsI (0.6 Å/s) and DMAI (0.2 Å/s). The main observable phases are assigned following literature reports.[177],[123]

Figure 5.4. (a) Absorption and (b) PL spectra for triple cation perovskites obtained by adding MAI (blue) or FAI (red) to the previously developed CsDMAPbI$_3$ perovskite, using a fourth source and *r* = 0.1 Å/s. (a) J−V curves under illumination for a representative MA_DMACsPbI$_3$ and FA_DMACsPbI$_3$ solar cells and corresponding (b) PV parameters extracted from J-V curves.

Figure 5.5. EQE spectrum (red) of a CsMADMAPbI$_3$ perovskite solar cell in the n-i-p configuration, with 250 nm thick perovskite, and corresponding integrated short-circuit current density with the AM1.5G solar irradiance spectrum.

Figure 5.6. (a) J−V curves for a triple cation CsMADMAPbI$_3$ perovskite solar cell, with a 400 nm thick absorber layer. (b) EQE spectrum with integrated current density and (c) PV parameters extracted from J-V curves.

Figure 5.7. (a) Cross-sectional SEM of a CsMADMAPbI$_3$ perovskite film deposited on a textured silicon substrate. (b) Zoom of the same sample highlighting the uniform thickness and low porosity of the perovskite coating.

Index of Tables

Table 3.1. Initial set of deposition rates of the perovskite precursors, calculated taking into account the target stoichiometry of the wide bandgap perovskite $FA_{0.6}Cs_{0.4}Pb(I_{0.8}Br_{0.2})_3$ (**r*(PbI$_2$) is fixed at 1.0 Å/s as a starting point).

Table 4.1. Average PV parameters extracted from the J-V characterization of quadruple-cation solar cells under simulated solar illumination.

Appendix D

List of Publications

1. **Isidora Susic**, Adi Kama, Lidón Gil-Escrig,* Chris Dreessen, Francisco Palazon, David Cahen, Michele Sessolo,* and Henk J. Bolink. Combinatorial Vacuum-Deposition of Wide Bandgap Perovskite Films and Solar Cells. *Adv. Mater. Interfaces* **2022**, 2202271. DOI: 10.1002/admi.202202271

2. **Isidora Susic**,§ Lidón Gil-Escrig,§ Francisco Palazon, Michele Sessolo,* and Henk J. Bolink. Quadruple-Cation Wide-Bandgap Perovskite Solar Cells with Enhanced Thermal Stability Enabled by Vacuum Deposition. *ACS Energy Lett*. **2022**, *7*, 1355−1363. DOI: 10.1021/acsenergylett.2c00304

3. **Isidora Susic**, Kassio P. S. Zanoni, Abhyuday Paliwal, Ismail C. Kaya, Zafer Hawash,* Michele Sessolo,* Ellen Moons, and Henk J. Bolink. Intrinsic Organic Semiconductors as Hole Transport Layers in p–i–n Perovskite Solar Cells. *Sol. RRL* **2022**, *6*, 2100882. DOI: 10.1002/solr.202100882

4. Lidón Gil-Escrig,* **Isidora Susic**, İlker Doğan, Valerio Zardetto, Mehrdad Najafi, Dong Zhang, Sjoerd Veenstra, Salar Sedani, Bulent Arikan, Selcuk Yerci, Henk J. Bolink, and Michele Sessolo*. Efficient and Thermally Stable Wide Bandgap Perovskite Solar Cells by Dual-Source Vacuum Deposition. *Adv. Funct. Mater.* **2023**, 2214357. DOI: 10.1002/adfm.202214357

5. Nina Arnosti, Fabian Brunner, **Isidora Susic**, Sarah Keller, José M. Junquera-Hernández, Alessandro Prescimone, Henk J. Bolink, Michele Sessolo,* Enrique Ortí,* Catherine E. Housecroft,* and Edwin C. Constable*. Remote Modification of Bidentate Phosphane Ligands Controlling the Photonic Properties in Their Complexes: Enhanced Performance of [Cu(RN-xantphos)(N^N)][PF$_6$] in Light-Emitting Electrochemical Cells. *Adv. Optical Mater.* **2020**, 1901689. DOI: 10.1002/adom.201901689

6. Lucía Martínez-Goyeneche, Lidón Gil-Escrig, **Isidora Susic**, Daniel Tordera, Henk J. Bolink, and Michele Sessolo*. Narrowband Monolithic Perovskite–Perovskite Tandem Photodetectors. *Adv. Optical Mater.* **2022**, *10*, 2201047. DOI: 10.1002/adom.202201047

7. Wiria Soltanpoor, Chris Dreessen, Mehmet Cem Sahiner, **Isidora Susic**, Amir Zarean Afshord, Vladimir S. Chirvony, Pablo P. Boix,* Gorkem Gunbas,* Selcuk Yerci,* and

Henk J. Bolink*. Hybrid Vapor-Solution Sequentially Deposited Mixed-Halide Perovskite Solar Cells. *ACS Appl. Energy Mater*. **2020**, *3*, 8257−8265. DOI: 10.1021/acsaem.0c00686

Acknowledgements

I still can’t believe that this PhD journey is getting to its end. First of all, I would like to thank my supervisors Henk and Michele, I am truly fortunate to have had their mentorship. This achievement would have been impossible without your guidance. Henk, thank you for giving me the opportunity to join the group and thank you for support, understanding, and encouragement throughout this journey. Michele, thank you for being so patient and always willing to discuss my work. I am very grateful for the constant support you gave me during my PhD and for believing in me. A ver si al final hacemos ese limoncello.

I would also like to thank my whole group for making this journey easier and more fun! Thank you for all great moments, laughter, trips and parties that we had together. Was a pleasure to be a part of such an international group. Lidón, Paz, Chris, Bas, Abhi, Lucía, Argha, Isabella, Kassio, Nathan, Fede, Cristina, Dani, María and Jorge thank you all for being a part of this journey!

Sobre todo, quería dar las gracias a Lidón, la persona que me ha ayudado más en el laboratorio y que me ha enseñado todos los trucos. Siempre dispuesta a escuchar y ayudar. Mi mejor compañera de la sala limpia y el Pilates, muchas gracias por todo tu apoyo! Eres un amor! Vamos team wide bandgap!

Paz! ¿Qué haría yo sin ti? (probablemente estaría ya deportada fuera de España haha) Desde el primer día juntas, mi compañera a todas las conferencias, has sido mi SOS, siempre ayudándome con los papeles y administración. Gracias por todos los momentos que hemos compartido juntas, las risas, los cotilleos y los viajes (sobre todo Holanda). Has sido mi gran apoyo durante el doctorado y estoy muy agradecida de tenerte en mi vida.

Bas (or better say responding on “Dios”/”God” haha), thank you for all your support during my PhD, for listening to all my complaints, for making me laugh, for the amazing moments and trips and above all thank you for being great friend!

Chris, my tandem, sharing the desk from the first day! Thank you for being patient with me, for answering my 1000 questions per day haha, for all the inspiring talks and discussions, trips, nights out, juegos de mesa and most of all thank you for being true friend!

Abhi, one of the best persons I have met, very enthusiastic and always ready to help. Thank you for your support, for unforgettable moments and for being a real friend!

Lucía, Argha, Isabella and Kassio thank you for the wonderful time we shared together and of course our gossip sessions. María y Jorge, muchas gracias por toda su ayuda durante estos años y por hacer un trabajo eficaz.

Also, I'd like to express my gratitude to both the former (Lorenzo, Benni, Maria Grazia, Azin, Dani, Jorge, Sang…) and newly joined group members (Javi, Manu, Joost, Serhii, Inma, Sofía, Michelino).

In the end, I want to dedicate my thesis to my family, this journey wouldn’t be possible without you! Hvala vam na nesebičnoj podršci, ljubalju i što ste uvek bili uz mene. Volim vas!